Macroscopic Models and Phase Resetting of Coupled Biological Oscillators

by

Kevin M. Hannay

A dissertation submitted in partial fulfillment
of the requirements for the degree of
Doctor of Philosophy
(Applied and Interdisciplinary Mathematics)
in the University of Michigan
2017

Doctoral Committee:

Associate Professor Victoria Booth Co-Chair
Professor Daniel B. Forger, Co-Chair
Professor Trachette Jackson
Assistant Professor Indika Rajapakse
Associate Professor Orie Shafer

Kevin M. Hannay
khannay@umich.edu
ORCID iD:0000-0003-0193-0245

For Melissa, my parents and my brother Ian

ACKNOWLEDGEMENTS

This work would not have been possible without the help, support and guidance of many people. My wife, Melissa, has been a major source of inspiration and without her I would not be where I am today. Her patience, tireless support and largely irrational belief in me, has made graduate school some of the best times of my life. I would also like to thank my two avian collaborators (pets), Bandit and Walt, whose utter lack of respect for me is a constant reminder of how little I know.

Of course, many thanks are owed to my co-advisors Danny Forger and Victoria Booth. First, I would like to thank you both for giving me an opportunity to work with you. When I first returned to graduate school following three years in the Marine Corps even I had doubts as to whether I could finish the graduate program. I'm glad you took a chance in investing your valuable time and energy into me. More than that you introduced me to a beautiful line of research, which no doubt will keep my mind occupied for the rest of my life. I could not have asked for better advisors over the last four years. Your scientific and life advice have been invaluable to me. I will miss our meetings together, but look forward to the transition from mentors to friends and colleagues.

I would also like to thank my other committee members Trachette Jackson, Orie Shafer and Indika Rajapakse for your continuous support during my graduate studies. Trachette Jackson's partial differential equations in biology class was a great help to me in writing this thesis. I want to thank Orie Shafer and all of his lab members for opening their laboratory to me and allowing a mathematician into their lab meetings.

I am indebted to Indika Rajapakse for his stimulating lectures on biological networks, helpful discussions and supreme enthusiasm for mathematical biology.

I also owe many thanks to Adam Stinchcombe, Amy Cochran, Dan DeWoskin, Olivia Walch and Scott Rich for stimulating discussions both about mathematics and perhaps especially for those not about mathematics. I would also like to thank Jihwan Myung for sharing both this data and insights into circadian rhythms with me.

I would also like to thank some of the many people who influenced my decision to pursue a graduate degree. First, my high school teachers Ron Sprott (Biology) and Ralph Real (Math) who challenged me to develop my mind. It is a testament to the influence they had on me that my graduate thesis is on mathematical biology. As an undergraduate I was lucky to have many scientific mentors and role models. Christine Vogel was my first scientific mentor and showed me the commitment it takes to produce new scientific work. Oscar Gonzalez was my first mathematics mentor and gave me the confidence to apply to mathematics graduate programs. Tim Keitt showed me how to apply mathematical reasoning to biological problems. Finally, Alan Cline who taught me and many others that academic success and happiness are not quite the same thing.

My family is also deserving of much of the credit for this work. They have been a constant source of support throughout my education. You also provided a much needed escape for Melissa and I from our graduate school lives and a reminder that life is about more than mathematics and circadian rhythms. I would also like to thank my brother Ian who would be very proud of his little brother finishing graduate school.

Finally, I would also like to thank all of my funding sources for their essential support during my graduate studies: the Human Frontiers of Science Program, the Air Force Office of Scientific Research, the Department of Mathematics at Michigan, National Science Foundation, and the Department of Veterans Affairs. The University of Michigan, Rackham Graduate School and the Mathematics Department are also

owed my thanks for their support of my military service during graduate school.

TABLE OF CONTENTS

LIST OF FIGURES

Figure

LIST OF TABLES

Table

LIST OF APPENDICES

Appendix

ABSTRACT

This thesis concerns the derivation and analysis of macroscopic mathematical models for coupled biological oscillators. Circadian rhythms, heart beats, and brain waves are all examples of biological rhythms formed through the aggregation of the rhythmic contributions of thousands of cellular oscillations. These systems evolve in an extremely high-dimensional phase space having at least as many degrees of freedom as the number of oscillators. This high-dimensionality often contrasts with the low-dimensional behavior observed on the collective or macroscopic scale. Moreover, the macroscopic dynamics are often of greater interest in biological applications.

Therefore, it is imperative that mathematical techniques are developed to extract low-dimensional models for the macroscopic behavior of these systems. One such mathematical technique is the Ott-Antonsen ansatz. The Ott-Antonsen ansatz may be applied to high-dimensional systems of heterogeneous coupled oscillators to derive an exact low-dimensional description of the system in terms of macroscopic variables. We apply the Ott-Antonsen technique to determine the sensitivity of collective oscillations to perturbations with applications to neuroscience.

The power of the Ott-Antonsen technique comes at the expense of several limitations which could limit its applicability to biological systems. To address this we compare the Ott-Antonsen ansatz with experimental measurements of circadian rhythms and numerical simulations of several other biological systems. This analysis reveals that a key assumption of the Ott-Antonsen approach is violated in these systems. However, we discover a low-dimensional structure in these data sets and

characterize its emergence through a simple argument depending only on general phase-locking behavior in coupled oscillator systems. We further demonstrate the structure's emergence in networks of noisy heterogeneous oscillators with complex network connectivity. We show how this structure may be applied as an ansatz to derive low-dimensional macroscopic models for oscillator population activity. This approach allows for the incorporation of cellular-level experimental data into the macroscopic model whose parameters and variables can then be directly associated with tissue- or organism-level properties, thereby elucidating the core properties driving the collective behavior of the system.

We first apply our ansatz to study the impact of light on the mammalian circadian system. To begin we derive a low-dimensional macroscopic model for the core circadian clock in mammals. Significantly, the variables and parameters in our model have physiological interpretations and may be compared with experimental results. We focus on the effect of four key factors which help shape the mammalian phase response to light: heterogeneity in the population of oscillators, the structure of the typical light phase response curve, the fraction of oscillators which receive direct light input and changes in the coupling strengths associated with seasonal day-lengths. We find these factors can explain several experimental results and provide insight into the processing of light information in the mammalian circadian system.

In a second application of our ansatz we derive a pair of low-dimensional models for human circadian rhythms. We fit the model parameters to measurements of light sensitivity in human subjects, and validate these parameter fits with three additional data sets. We compare our model predictions with those made by previous phenomenological models for human circadian rhythms. We find our models make new predictions concerning the amplitude dynamics of the human circadian clock and the light entrainment properties of the clock. These results could have applications to the development of light-based therapies for circadian disorders.

CHAPTER I

Introduction

Synchronization of coupled oscillators is a fundamental phenomenon for many biological processes including neural activity, circadian rhythms and cardiac dynamics. Accurate mathematical models for these systems are extremely high dimensional as they describe the complex dynamics of each individual oscillator embedded in a network of thousands of oscillators. This high dimensionality contrasts with the low-dimensional dynamics observed at the collective or macroscopic scale for many of these systems, for example epileptic seizure activity, circadian activity cycles and normal heart beats. Moreover, this high dimensionality can obscure insights provided by the biological accuracy of the models and makes simulations of such systems costly. On the other hand, phenomenological macroscopic-level models developed for coupled oscillator systems can address the dimensionality issues, but at the expense of the biological fidelity of the results.

Thus, it is imperative that mathematical techniques are developed which can extract a low-dimensional macroscopic model from a high-dimensional microscopic model in a systematic manner. In 2008, Edward Ott and Thomas Antonsen introduced such a macroscopic reduction for large systems of heterogeneous coupled oscillators [114, 113]. This discovery led to an explosion of results in the coupled oscillator literature over the last decade. The Ott Antonsen technique has been used to

study diverse issues such as chimera states, hierarchical synchrony, circadian rhythms and neuroscience [93, 115, 102]. However, despite the tremendous success and popularity of the Ott-Antonsen approach, its efficacy for describing real biological systems has not been evaluated in the literature.

In Chapter II, we compare the assumptions of the Ott-Antonsen approach with experimental measurements from cells in the mammalian circadian pacemaker and numerical simulations of several models of coupled biological oscillators. We find a core assumption of the Ott-Antonsen approach is not valid for these systems. Interestingly, we find a different, but related, ansatz which describes these diverse systems accurately. Our key results are to demonstrate the generality of our ansatz, which we call the m^2 ansatz, in networks of coupled oscillators and illustrate its use in extracting low-dimensional macroscopic models. We characterize the emergence of our ansatz based on the nature of the heterogeneity in the oscillator ensemble, and contrast this with conditions which yield the Ott-Antonsen relation. We find our ansatz can describe systems of noisy heterogeneous oscillators with complex network connectivity-extending the validity of our approach beyond the range of the Ott-Antonsen technique. In biological applications, our approach allows for the incorporation of cellular level experimental data into the macroscopic model whose parameters and variables can be directly associated with tissue-or organism-level properties, thereby elucidating the core properties driving the collective behavior of the system.

In many biological applications, we are interested in how perturbations imposed on individual oscillators will affect the collective rhythm produced by the coupled ensemble. In Chapter III, I apply the Ott-Antonsen procedure to study collective phase-resetting in large ensembles of coupled oscillators. This work has its origins in the study of phase response curves (PRC) which are a useful tool from both a theoretical and experimental prospective [156, 124]. Phase response curves describe the effect of an external perturbation on the phase of an oscillator. For example, in

a rhythmically firing neuron a voltage stimulus may be applied at some phase in the oscillation and the effect on the timing of the next action potential measured. If this shift is measured over a sampling of initial phases, a continuous phase response curve may be estimated. The amplitude, shape and zeros of the phase response curve can be used to determine the entrainment properties of the oscillator [156].

However, biological oscillators are usually found integrated into large assemblages of rhythmic components rather than as single isolated systems. Collective phase response curves extend phase response theory from considering a single oscillator to considering an entire population of coupled oscillators. Here phase shifts are measured in terms of the mean phase of a population of oscillators in response to a perturbation applied to the individual oscillators. In the neuronal example, we are interested in how phase shifts on the individual neuron scale are integrated into the collective oscillations of an entire brain region. This transformation is affected by several factors including the phase distribution of the individual cells and the coupling between the oscillators. In Chapter III, I develop an analytical framework, based on the Ott-Antonsen approach, for computing the collective phase response curve from knowledge of how the individual oscillators react to the stimulus. This work shows the impact of the Fourier composition of the individual phase response curve. The first harmonic of the individual phase response curve is seen to be amplified in the collective phase response as the individual oscillators lose synchrony. Higher harmonics in the phase response curve are damped out on the collective scale. This leads to a predictable change in the amplitude, shape and zeros in the collective phase response curve thereby affecting the entrainment properties of the ensemble.

In Chapter IV, we return to the m^2 ansatz formalism and examine the impact of light on the mammalian circadian rhythm. The mammalian circadian rhythm has been localized to a small region of the hypothalamus known as the suprachiasmatic nucleus (SCN) [103, 139]. The SCN is composed of thousands of individual

clock neurons each of which contain an intricate genetic feedback loop which cycles with a period of about twenty-four hours [92]. The mammalian circadian rhythm is produced as an emergent phenomenon through the aggregation of the rhythmic contributions of each of these molecular clocks. A defining property of circadian rhythms is their ability to be entrained to environmental cycles. In mammals, the most powerful entraining signal is the daily light cycle [123]. However, only a fraction of the clock neurons in the SCN are recipients of light information [98]. Therefore, we divide the circadian oscillator population into a ventral population which receives light information and a dorsal population which does not receive direct light input [98]. Making use of the m^2 ansatz we derive a low-dimensional model for the response of the mammalian circadian clock to a light pulse. Using our reduced model, we derive analytical results on how the coupling strengths between the ventral and dorsal populations shape the collective response to a light stimulus. Our analysis provides a parsimonious explanation for an experimentally observed reduction in the sensitivity of the mammalian circadian clock to light during summer months when organisms are exposed to long day-lengths [126, 147]. The simplicity of our derived model, along with the physiological interpretations of the variables and parameters also allows the change in coupling predicted by the model to be checked for consistency with other experimental data. Significantly, this analysis reveals that seasonal effects, light-resetting and after-effects of light entrainment are all intimately related phenomena.

In Chapter V, we employ the m^2 ansatz to derive a macroscopic model for the master circadian clock in humans. Experimental measurements of the circadian light response in humans are used to determine model parameters. In order to allow for noise in experimental measurements, as well as the population variability of the circadian light response, we make use of a Markov Chain Monte Carlo (MCMC) approach to produce a parameter ensemble which is consistent with the experimental

data. We validate the fitted model through the use of three additional data sets, and discuss the differences between the model's predictions and earlier models of human circadian rhythms.

Finally, the overall conclusions from my graduate work are discussed in Chapter VI. The remainder of this chapter is devoted to introducing key mathematical results (Sec. 1.1) and providing an introduction to circadian rhythms, (Sec. 1.2) the principal biological application considered here.

1.1 Mathematical Background

1.1.1 Kuramoto Model

While still an undergraduate, Art Winfree, began studying large systems of coupled oscillators motivated by his interest in biological rhythms [158, 141]. He intuitively grasped that oscillators on a stable limit cycle may be described using a single *phase* variable describing their progress along a circular orbit. This mode of analysis, now known as phase reduction, was put on mathematical footing by Yoshiki Kuramoto in his 1984 book "Chemical Oscillations, Waves, and Turbulence" [86]. Here he also presented a derivation of his now famous equation describing the dynamics of coupled oscillators,

$$\frac{d\phi_i}{dt} = \omega_i + \frac{K}{N}\sum_{j=1}^{N}\sin(\phi_j - \phi_i) \qquad\qquad i = 1, 2 \ldots N \tag{1.1}$$

where ϕ_i gives the phase of the oscillator, ω_i the natural frequency and K the coupling strength between the oscillators. The natural frequencies ω_i are typically assumed to be drawn from some distribution $g(\omega)$ and describe the frequency of the oscillators in the absence of coupling (this is often called heterogeneity). As the coupling strength (K) between the oscillators increases the oscillators begin to spend more time close to one another in phase. Finally, at some critical coupling strength K_c an ordered

synchronized state emerges out of the previous disorder. This synchronization transition can be beautifully observed throughout nature: Southeast Asian fireflies firing in unison, fish schools moving as a superorganism, cardiac cells firing together to form a heartbeat, brain waves and many other phenomena [141]. The broad applications and mathematical tractability of the Kuramoto model have made it the go-to model for studying synchronization for over forty years.

Equation 1.1 provides a mean-field model for studying synchrony, although it may be generalized in several ways to more closely match application areas. For a general network of coupled limit cycle oscillators we may apply the phase-reduction procedure to derive a model of the form:

$$\frac{d\phi_i}{dt} = \omega_i + \sum_{j=1}^{N} \Gamma_{ij}(\phi_j - \phi_i), \tag{1.2}$$

where Γ_{ij} is a 2π periodic coupling function describing the influence of the jth oscillator on oscillator i. I will outline the general phase reduction procedure in Sec. 1.1.4, and specify the added assumptions which allow for simplification to the Kuramoto model (Eq. 1.1).

1.1.2 Self-Consistency Arguments

Along with deriving the model which bears his name, Kuramoto's seminal work also introduced a powerful mode of analysis called *self-consistency analysis*. This technique enabled him to derive the first analytical results describing the onset of synchrony in a population of heterogeneous oscillators. These self-consistency arguments dominated early studies of large systems of coupled oscillators, and are still used frequently in the literature today [149, 65, 150]. In this section I will give a brief overview of the original self-consistency argument used by Kuramoto to derive a formula for the critical coupling strength in the Kuramoto model [142, 86]. For the

purposes of this section we consider the distribution of natural frequencies $g(\omega)$ in the Kuramoto model (Eq. 1.1) to be smooth, unimodal and symmetric.

A first step in studying synchrony is establishing an order parameter which indicates when synchrony is present in the oscillator population. The Kuramoto order parameter is given by,

$$Z(t) = Re^{i\psi} = \langle e^{i\phi} \rangle = \frac{1}{N} \sum_{j=1}^{N} e^{i\phi_j} \in \mathbb{C}, \tag{1.3}$$

where $R \in [0, 1]$ is called the phase coherence of the population and ψ is the mean-phase. Geometrically, $Z(t)$ is the centroid of the oscillator population placed on the complex unit circle. If $R = 0$ the oscillators are uniformly distributed on the unit circle (desynchrony) and $R = 1$ when they are all in the same phase (perfect synchrony). For intermediate values $0 < R < 1$ the order parameter retains its utility, as it measures the degree of synchrony in the population. For these intermediate values of R the Kuramoto model shows partial synchrony, a state in which some oscillators are phase-locked in a synchronized pack and others are drifting relative to this synchronized pack.

Critically, the Kuramoto equation may be re-written making use of the Kuramoto order parameter,

$$\frac{d\phi_i}{dt} = \omega_i + KR(t) \sin(\psi(t) - \phi_i). \tag{1.4}$$

Examining Eq. 1.4 we notice the interaction between the oscillators now depends only on the global order parameter. Moreover, we can begin to see how synchronized solutions may emerge from this system: as $R(t)$ grows from zero, the synchronized pack grows and this increases the pull on the oscillators to join the synchronized pack. This positive feedback mechanism leads synchronized solutions to grow quickly above the critical coupling K_c strength.

We now seek synchronized solutions for which $R(t)$ is constant and ψ rotates with a constant frequency Ω. Changing to a rotating frame of reference $\theta_i = \phi_i - \Omega t$, $\hat{\omega}_i = \omega_i - \Omega$ and choosing the coordinate frame such that the mean phase vanishes ($\psi = 0$) we may write our system as,

$$\dot{\theta}_i = \hat{\omega}_i - KR\sin(\theta_i). \tag{1.5}$$

If $R(t)$ is constant then the equations for each of the oscillators decouple, and we see that θ_i will go to a constant value if and only if $|\hat{\omega}| \leq KR$. These are the oscillators which are locked to the mean-field oscillation, meaning they move with the collective frequency Ω in the synchronized pack. Those oscillators at the extreme frequencies $|\hat{\omega}_i| > KR$ will drift relative to the mean-field and are not synchronized. They will drift in and out of phase with the mean-field oscillation over time. Thus, we may divide the population of oscillators into two classes based on their frequencies $|\hat{\omega}_i|$:

1. Locked oscillators with $|\hat{\omega}_i| \leq KR$ will evolve to a fixed θ_i such that $\sin(\theta_i) = \hat{\omega}_i/KR$,

2. Drifting oscillators with $|\hat{\omega}_i| > KR$, where $|\theta_i|$ grows without bound as time increases.

This analysis may now be compared with the original definition of the Kuramoto order parameter (Eq. 1.3) for consistency (hence the name self-consistency argument). To check for consistency we break the population into the locked and drifting populations,

$$R = \langle e^{i\theta} \rangle_{lock} + \langle e^{i\theta} \rangle_{drift}, \tag{1.6}$$

where I have used that we set the mean phase to zero ($\psi = 0$) in our coordinate frame. First, we evaluate the contribution of the locked oscillators using our assumption that

$g(\hat{\omega})$ is a unimodal and symmetric distribution of natural frequencies centered about zero. Thus, we find the locked oscillator contribution is given by,

$$\langle e^{i\theta} \rangle_{lock} = \int_{-KR}^{KR} e^{i\theta(\hat{\omega})} g(\hat{\omega}) d\hat{\omega} = \int_{-KR}^{KR} \cos(\theta(\hat{\omega})) g(\hat{\omega}) d\hat{\omega}, \tag{1.7}$$

using that $g(\hat{\omega})$ is symmetric and sin is an odd function. Changing variables from $\hat{\omega}$ to θ in the integral gives,

$$\langle e^{i\theta} \rangle_{lock} = KR \int_{-\pi/2}^{\pi/2} \cos^2(\theta) g(KR\sin(\theta)) d\theta. \tag{1.8}$$

It turns out the corresponding integral for the drifting oscillators vanishes, i.e. $\langle e^{i\theta} \rangle_{drift} = 0$. Intuitively, this is what our order parameter should tell us: the drifting oscillators are not synchronized and so we expect that R_{drift}=0. Thus, the self-consistency condition reduces to,

$$R = \langle e^{i\theta} \rangle_{lock} = KR \int_{-\pi/2}^{\pi/2} \cos^2(\theta) g(KR\sin(\theta)) d\theta. \tag{1.9}$$

The self-consistency condition (Eq. 1.9) shows that the desynchronized solution, $R = 0$, is always a solution regardless of the coupling strength K. However, we may also have solutions on a second branch with $R > 0$,

$$1 = K \int_{-\pi/2}^{\pi/2} \cos^2(\theta) g(KR\sin(\theta)) d\theta. \tag{1.10}$$

These solutions will emerge continuously from the $R = 0$ branch at a critical coupling strength K_c given by,

$$K_c = \frac{2}{\pi g(0)}, \tag{1.11}$$

found by taking $R \to 0^+$ in Eq. 1.10. Therefore, Kuramoto had demonstrated the

emergence of synchronized solutions above a specified critical coupling strength K_c.

While self-consistency analysis is a powerful tool for analyzing the Kuramoto model, this formalism proved to be the wrong choice for analyzing the stability of solutions. The challenge of analyzing stability ushered in an era of large center manifold reductions which proved up to the task of analyzing stability of the Kuramoto model [24, 142, 25]. In the next section we skip forward to the predominant current technique.

1.1.3 Ott-Antonsen Theory

In the last decade the dominant tool for analyzing systems of coupled phase oscillators has been Ott-Antonsen (OA) theory [114, 113]. This powerful ansatz is capable of reducing the Kuramoto model to a closed system of ordinary differential equations for the Kuramoto order parameter. Ott-Antonsen theory served as an inspiration and jumping off point for my dissertation research.

To begin we consider a slight generalization of the Kuramoto model, known as the Kuramoto-Sakaguchi model [129],

$$\frac{d\phi_i}{dt} = \omega_i + \frac{K}{N}\sum_{j=1}^{N}\sin(\phi_j - \phi_i + \beta), \tag{1.12}$$

where $\frac{-\pi}{2} < \beta < \frac{\pi}{2}$. The additional parameter β is known as the shear parameter and introduces a cosine component into the coupling function of the classic Kuramoto equation [101]. Significantly, when $\beta \neq 0$ the coupling function between the oscillators is no longer an odd function of the phase difference. In Chapter III, we will see this makes the collective frequency of the synchronized oscillators vary with the collective amplitude of the system and can have significant effects on the dynamics of the system following a perturbation.

Similar to the classical Kuramoto equation we may re-write the coupling terms in

the Kuramoto-Sakaguchu model using the Kuramoto order parameter (Eq. 1.3),

$$\frac{1}{N}\sum_{j=1}^{N}\sin(\phi_j-\phi_i+\beta)=Im[e^{i\beta}e^{-i\phi_i}Z] \tag{1.13a}$$

$$\frac{d\phi_i}{dt}=\omega_i+KIm[e^{i\beta}e^{-i\phi_i}Z], \tag{1.13b}$$

where again we see the interaction between the oscillators depends only on the order parameter Z. We now consider the continuum limit of this system, that is the limit as the number of oscillators approaches infinity ($N\to\infty$). This enables us to define the continuous phase density function for this system as $f(\omega,\phi,t)$ where $fd\phi d\omega$ gives the fraction of oscillators at phase ϕ with natural frequency ω at time t. Assuming the number of oscillators at each frequency is conserved gives a continuity equation for the dynamics of the system,

$$f_t+\frac{\partial}{\partial\phi}[f(\omega+KIm[e^{i\beta}e^{-i\phi}Z])]=0 \tag{1.14a}$$

$$f_t+\frac{\partial}{\partial\phi}[f\omega+\frac{fK}{2i}(Ze^{i\beta}e^{-i\phi}-Z^*e^{-i\beta}e^{i\phi})]=0 \tag{1.14b}$$

where I have used the property that $Im[z]=\frac{z-z^*}{2i}$ for $z\in\mathbb{C}$ and stars denote the complex conjugate. In the continuum limit the Kuramoto order parameter $Z(t)$ may be defined as,

$$Z(t)=Re^{i\psi}=\int_{-\infty}^{\infty}\int_{0}^{2\pi}f(\omega,\phi,t)e^{i\phi}d\phi d\omega, \tag{1.15}$$

making the continuity equation (Eq. 1.14b) a nonlinear partial integro-differential equation through its dependence on $Z(t)$. We may consider the Fourier series of $f(\omega,\phi,t)$ in ϕ,

$$f(\omega,\phi,t)=\frac{g(\omega)}{2\pi}\sum_{n=-\infty}^{\infty}A_n(\omega,t)e^{in\phi}, \qquad A_0=1. \tag{1.16}$$

Now we introduce the Ott-Antonsen ansatz and restrict our phase distribution functions $f(\omega, \phi, t)$ to those which have a special property,

$$A_1(\omega, t) = \alpha(\omega, t) \qquad\qquad A_n(\omega, t) = [\alpha(\omega, t)]^n, \tag{1.17}$$

in their Fourier series representations. We add the restriction that $|\alpha(\omega, t)| \leq 1$ so this series does not diverge. Remarkably, if we restrict to this space of distribution functions the continuity equation (Eq. 1.14b) simplifies to,

$$\frac{\partial \alpha(\omega, t)}{\partial t} + \frac{K}{2}\left(Ze^{i\beta}[\alpha(\omega, t)]^2 - Z^* e^{-i\beta}\right) + i\omega\alpha(\omega, t) = 0. \tag{1.18}$$

Furthermore, we may also find an expression for the order parameter $Z(t)$ in the space of Ott-Antonsen distribution functions,

$$Z^*(t) = \int_{-\infty}^{\infty}\int_0^{2\pi} \frac{g(\omega)}{2\pi}[e^{-i\phi} + \sum_{n=1}^{\infty} \alpha^n(\omega, t)e^{i(n-1)\phi} + \alpha^*(\omega, t)^n e^{i(-n-1)\phi}]d\phi d\omega \tag{1.19}$$

Exchanging the integral and sum, causes all terms but $n = 1$ to go to zero giving,

$$Z^*(t) = \int_{-\infty}^{\infty} g(\omega)\alpha(\omega, t)d\omega, \qquad\qquad Z(t) = \int_{-\infty}^{\infty} g(\omega)\alpha^*(\omega, t)d\omega. \tag{1.20}$$

It should be noted that the Ott-Antonsen ansatz (Eq. 1.17) has not achieved a dimension-reduction as of yet-as the system is still infinite dimensional through the ω variable. That is not to say the transformation constructed so far is without use. A restriction to these special phase distribution functions has eliminated the ϕ dependence in the continuity equation, which reduces the numerical burden of simulation and allows for more powerful analytical analysis [112].

1.1.3.1 Dimension Reduction in the Ott-Antonsen Theory

As noted thus far we have not achieved a dimension reduction through the use of the Ott-Antonsen ansatz. To achieve a dimension reduction we need to assume a special form for $g(\omega)$, the distribution of natural frequencies of the system. The most common assumption on the distribution of natural frequencies is to consider the Cauchy (Lorentzian) distribution of natural frequencies,

$$g(\omega) = \frac{\gamma}{\pi[(\omega - \omega_0)^2 + \gamma^2)]}, \tag{1.21}$$

where ω_0 is the median frequency and γ controls the range of heterogeneity in the oscillator population. The Cauchy distribution has very heavy tails-in fact, the heavy tails of the Cauchy distribution endow it with several pathological properties such as a divergent second moment. However, for the purposes of the Ott-Antonsen technique it has the important property that it has a pole in the lower-half complex plane at $\omega = \omega_0 - i\gamma$. Thus, if we add the restriction on our space of distribution functions that $\alpha(\omega, t)$ may be analytically continued into the lower half complex plane we may compute the integral for the order parameter $Z(t)$ (Eq. 1.20) using a semi-circle contour in the lower half-plane,

$$Z(t) = \int_{-\infty}^{\infty} g(\omega)\alpha^*(\omega, t)d\omega = \alpha^*(\omega_0 - i\gamma). \tag{1.22}$$

Therefore, for the case of a Cauchy distribution of natural frequencies the infinite frequency modes all collapse to an evaluation at a single complex frequency ($\omega = \omega_0 - i\gamma$). Evaluating our system for $\alpha(\omega, t)$ at this point gives,

$$\frac{\partial \alpha}{\partial t} + \frac{K}{2}(Ze^{i\beta}\alpha^2 - Z^*e^{-i\beta}) + i\omega\alpha = 0 \tag{1.23a}$$

$$\frac{dZ^*}{dt} + \frac{K}{2}(Ze^{i\beta}(Z^*)^2 - Z^*e^{-i\beta}) + i\omega_0 Z^* + \gamma Z^* = 0, \tag{1.23b}$$

which is a complex ordinary differential equation for the order parameter $Z^*(t)$. If we substitute $Z^*(t) = R(t)e^{-i\psi(t)}$ into the system we get,

$$\dot{R}e^{-i\psi} - iR\dot{\psi}e^{-i\psi} + \gamma Re^{-i\psi} + i\omega_0 Re^{-i\psi} + \frac{K}{2}(R^3e^{i\beta}e^{-i\psi} - Re^{-i\beta}e^{-i\psi}) = 0 \quad (1.24a)$$

$$\dot{R} - iR\dot{\psi} + \gamma R + i\omega_0 R + \frac{K}{2}(R^3e^{i\beta} - Re^{-i\beta}) = 0. \quad (1.24b)$$

Separating the real and imaginary parts of the expression, we find a two-dimensional system for the mean-phase ψ and phase coherence R of the oscillator population,

$$\dot{R} = \frac{K\cos(\beta)}{2}R(1-R^2) - \gamma R \quad (1.25a)$$

$$\dot{\psi} = \omega_0 + \frac{R\sin(\beta)}{2}(1+R^2). \quad (1.25b)$$

We may apply a similar procedure for any distribution of natural frequencies $g(\omega)$ which has a finite number of poles in the complex plane [114]. In general, for this dimension reduction technique we will see two dimensions in the macroscopic reduction for each pole of the natural frequency distribution $g(\omega)$.

1.1.3.2 Ott-Antonsen Manifold and Generalizations

The derivation we presented here can in fact be generalized to consider any infinite ensemble of oscillators whose dynamics can be put into the form,

$$\frac{d\phi_j}{dt} = \omega_j + \mathrm{Im}[H(t)e^{-i\phi_j}] \qquad j = 1, 2, ...N \quad (1.26)$$

as $N \to \infty$. For example, the Kuramoto model takes this form with $H(t) = KZ(t)$. Ott and Antonsen showed that the space of distribution functions defined by their ansatz, the Ott-Antonsen manifold, contains both the desynchronized ($\alpha = 0$) and perfect synchrony ($\alpha = 1$) distribution functions [114]. In addition, they demonstrated that when these systems are initialized on the Ott-Antonsen manifold it will

stay on this manifold for all time [114]. Finally, they demonstrated that all the long-time attractors of the system (Eq. 1.26) are captured within this manifold [113].

The proof of these theorems enabled the analytical study of systems of heterogeneous coupled oscillators which had previously only been accessible through numerical studies. However, it is worth noting that the power of Ott-Antonsen theory comes at the price of several limitations. First, the coupling function between the oscillators can only have a single harmonic component [95]. Secondly, OA theory is not valid for systems which are subjected to stochastic forces. The final issue of note is one of practicality rather than of a mathematical nature. As noted when the dimension reduction was demonstrated, the dimension reduction to a macroscopic model relies on the distribution of natural frequencies taking the form of a rational function. In particular, the simplest choice of a Cauchy distribution has several pathological properties stemming from its heavy polynomial tails which may limit its applicability for biological systems. A major focus of this thesis is to evaluate the validity of these assumptions for biological systems, and to introduce modifications to the Ott-Antonsen approach to more closely model biological systems.

1.1.4 Phase Resetting

A key property of oscillating systems is their stability to perturbations off the attracting limit cycle. For a stable limit cycle small perturbations along the limit cycle will be retained, while small perturbations off the attracting cycle will decay asymptotically. It is precisely this neutral stability along the limit cycle which allows weak interactions among oscillators to give rise to synchronization and entrainment [118].

Thus, studying the sensitivity of the phase of an oscillator to perturbations can reveal much about how the oscillator synchronizes when coupled with similar systems and its entrainment by periodic perturbations from outside forces. For example,

in the study of circadian rhythms it is common to introduce a perturbation, such as a light stimulus, at a sampling of points across the twenty-four hour cycle. The phase of the circadian rhythms may be assessed before and after the application of the stimulus through the monitoring of circadian markers such as wheel-running behavior in hamsters or core body temperature oscillations in humans. These experiments produce a map from the initial phase measured just prior to the stimulus to the final phase assessed after the stimulus. This map $\phi_i \to \phi_f$ is called a phase transition curve (PTC). Equivalently, we may define a phase response curve (PRC) mapping the initial phase to the phase shift induced by the stimulus $\phi_i \to \Delta\phi$. Phase response curves are also widely used in studying neuronal oscillators where the stimulus may be a current pulse and the phase shifts are determined by the effect on the timing of the next action potential.

Interestingly, the theory of phase response curves arises in a theoretical context in the derivation of Kuramoto's equation [86]. Since phase response theory figures prominently in this thesis I give an outline of the phase reduction process here. Let $\dot{X} = \vec{F}(X)$ define a dynamical system with a hyperbolic limit cycle solution and $\vec{p}(t)$ define a general time-dependent perturbation of the system scaled by the parameter ϵ.

$$\dot{X} = \vec{F}(X) + \epsilon\vec{p}(t), \qquad X \in \mathbb{R}^M. \tag{1.27}$$

For the unperturbed oscillator equation let the limit cycle be denoted as C, a curve in $\mathbb{R}^M$. Then while the solution trajectory is on the limit cycle we can parametrize its position in $\mathbb{R}^M$ using a single parameter $\phi \in [0, 2\pi]$ called the phase of the oscillator. Let the parametrization be defined such that $\frac{d\phi}{dt} = \omega$. The phase of the oscillator is easily defined on the unperturbed ($\epsilon \to 0$) limit cycle of the oscillator, but in order to consider the case of $\epsilon \neq 0$ we need to extend this definition to define the

phase of the oscillator for points in some neighborhood of the limit cycle. Call this tubular ring neighborhood about the limit cycle G. To extend our phase function $\phi : C \subset \mathbb{R}^M \to \mathbb{R}$ to $\phi : G \subset \mathbb{R}^M \to \mathbb{R}$, we will need the concept of asymptotic phase.

Definition I.1 (Asymptotic Phase)**.** We say two points $P \in G$ and $Q \in G$ have the same asymptotic phase if as $t \to \infty$, $\phi_P = \phi_Q$

Definition I.2 (Isochron)**.** $I(\phi)$=$\{x \in G|$ asymptotic phase of x = $\phi\}$ is a $M-1$ dimensional hypersurface embedded in $\mathbb{R}^M$ and is called an isochron of the oscillator [156].

Notice that nothing about our definition of isochrons needs to be restricted to a small neighborhood of the limit cycle. In fact, isochrons can be uniquely defined throughout the basin of attraction of the limit cycle. Points where isochrons cross one another (and thus a phase cannot be defined) are called phase singularities. The presence of phase singularities can give rise to interesting spatiotemporal behavior [86, 59, 156].

Applying our definitions of the phase $\phi(X)$ and the dynamical system reveals,

$$\frac{d\phi(X)}{dt} = \nabla\phi \cdot \frac{dX}{dt}, \tag{1.28a}$$

$$\frac{d\phi(X)}{dt} = \nabla\phi \cdot \vec{F}(X) + \epsilon\nabla\phi \cdot \vec{p}(t), \tag{1.28b}$$

$$\frac{d\phi(X)}{dt} = \omega + \epsilon\nabla\phi \cdot \vec{p}(t), \tag{1.28c}$$

using that $\nabla\phi \cdot \vec{F}(X) = \omega$ on the unperturbed limit cycle. We assumed the perturbation is small so we know X is close to $X_0(\phi)$, where $X_0(\phi)$ is the intersection of the isochron $I(\phi)$ with the limit cycle C. Thus to leading order in ϵ we can replace X with its value on the limit cycle $X_0(\phi)$.

$$\frac{d\phi}{dt} = \omega + \epsilon\nabla\phi|_{X_0(\phi)} \cdot \vec{p}(t) \tag{1.29}$$

Now we define $\vec{Q}(\phi) = \nabla\phi|_{X_0(\phi)}$ to be the *infinitesimal phase response curve*. Notice that it is just the gradient of the isochron $I(\phi)$ evaluated on the limit cycle. If the isochron hypersurface is a hyperplane then this approximation will be exact, whereas significant curvature in the isochron surface will degrade the accuracy of this linear approximation. If we assume that $\vec{p}(t)$ is a perturbation in just one variable of our system, (e.g. the voltage in a neuronal model), then the vector equation (Eq. 1.29) simplifies to the following:

$$\frac{d\phi}{dt} = \omega + \epsilon Q(\phi)p(t). \tag{1.30}$$

The finite phase response curve $\hat{Q}(\phi)$ in response to a perturbation defined by $p(t)$ will then be given by the difference in phase between this perturbed system and an unperturbed system as $t \to \infty$. If we make the change of variables $\psi = \phi - \omega t$ this measures the phase difference between the perturbed system and an unperturbed system.

$$\frac{d\psi}{dt} = \epsilon Q(\psi + \omega t)p(t) \tag{1.31a}$$

$$\int_0^\infty \frac{d\psi}{dt}dt = \int_0^\infty \epsilon Q(\psi + \omega t)p(t)dt \tag{1.31b}$$

$$\hat{Q}(\psi) = \epsilon \int_0^\infty Q(\psi + \omega t)p(t)dt \tag{1.31c}$$

Therefore, the finite phase response curve $\hat{Q}(\theta)$ can be approximated as

$$\hat{Q}(\theta) = \epsilon \int_0^\infty Q(\theta + \omega t)p(t)dt = \epsilon Q * p \tag{1.32}$$

where $*$ denotes convolution. Recall the approximation here comes as a result of approximating $\vec{Q}(\phi_i) = \nabla\phi|_{X_0(\phi)}$, which is valid only to leading order in ϵ (small perturbation off the limit cycle). If $p(t)$ is given by a Dirac delta function then the infinitesimal and finite phase response curves are seen to coincide $\hat{Q}(\theta) = Q(\theta)$,

hence the name infinitesimal for $Q(\theta)$. Therefore, the infinitesimal phase response curve is often approximated experimentally by giving very short and weak stimuli to the system and measuring the phase shifts induced. Moreover, Eq. 1.32 shows how the infinitesimal phase response curve may be used to approximate the finite phase response of the oscillator to a general stimulus $p(t)$.

Finally, we note that phase reduction may also be applied to systems of coupled oscillators. This situation may be described in its full form by the following system of differential equations:

$$\dot{X}_1 = \vec{F}_1(X_1) + K\vec{V}(X_1, X_2) \tag{1.33a}$$

$$\dot{X}_2 = \vec{F}_2(X_2) + K\vec{V}(X_2, X_1) \tag{1.33b}$$

where $X_{1,2} \in \mathbb{R}^M$, $\vec{F}_{1,2}$ define the uncoupled dynamics of the oscillators, $\vec{V}$ is the interaction function between the oscillators and is assumed to be symmetric between the oscillators. Here our time dependent perturbation $\vec{p}(t)$ is defined by the interaction function V. Once again we may parameterize the autonomous limit cycles such that $\frac{d\phi}{dt} = \omega_{1,2}$ on the limit cycle respectively for F_1 and F_2 and extend this definition into a neighborhood of the limit cycle using the concept of isochrons. The calculation follows the same form as the phase response calculation, except we now consider the coupling strength K a small parameter,

$$\dot{\phi_1} = \omega_1 + K\vec{Q}_1(\phi_1) \cdot \vec{V}(X_1(\phi_1), X_2(\phi_2)), \tag{1.34a}$$

$$\dot{\phi_2} = \omega_2 + K\vec{Q}_2(\phi_2) \cdot \vec{V}(X_2(\phi_2), X_1(\phi_1)), \tag{1.34b}$$

where $\nabla\phi(X_0(\phi) = \vec{Q}(\phi)$. Grouping the interaction terms together and evaluating

the functions on the limit cycle we have the following expression,

$$\dot{\phi_1} = \omega_1 + KM_1(\phi_1, \phi_2) \tag{1.35a}$$

$$\dot{\phi_2} = \omega_2 + KM_2(\phi_2, \phi_1) \tag{1.35b}$$

We simplify Eq. 1.35 further by considering the double Fourier series for the interaction functions M and plugging-in the zero order solutions for $\phi_1 \approx \omega_1 t$ and $\phi_2 \approx \omega_2 t$. Considering only the first oscillator gives,

$$M_1(\phi_1, \phi_2) = \sum_{k,l} a_{k,l} e^{i(k\omega_1 + l\omega_2)t}. \tag{1.36}$$

M_1 has fast oscillating as well as slow oscillating terms. The slow terms satisfy the resonance condition $k\omega_1 + l\omega_2 \approx 0$. The fast terms lead to phase deviations of order K but the slow terms act on the timescale $\frac{1}{K}$ and can induce large changes in the phase [118].

If we assume that $\omega_1 \approx \omega_2$ then only terms of the form $l = -k$ will satisfy the resonance condition. In general we could have the terms of the form $n\omega_1 - m\omega_2$ which would give higher order phase locking [118]. The assumption of $\omega_1 \approx \omega_2$ allows us to define,

$$\Gamma_1(\phi_1 - \phi_2) = \sum_k a_{-k,k} e^{ik(\omega_1 - \omega_2)t} = \sum_k a_{-k,k} e^{ik(\phi_1 - \phi_2)} \tag{1.37}$$

where the periodic function $\Gamma(\theta)$ is known as the coupling function. We note the coupling function is derived from both the interaction function $\vec{V}(X_1, X_2)$ in the full limit cycle model and the infinitesimal phase response curve $Q(\phi)$. Written in terms

of these coupling functions the system (Eq. 1.35) becomes,

$$\frac{d\phi_1}{dt} = \omega_1 + K\Gamma_1(\phi_2 - \phi_1) \tag{1.38a}$$

$$\frac{d\phi_2}{dt} = \omega_2 + K\Gamma_2(\phi_1 - \phi_2). \tag{1.38b}$$

Now, we see the simple Kuramoto coupling function arises if we take only the $\sin(\theta)$ term in a Fourier series of the full coupling functions $\Gamma_{1,2}(\theta)$.

1.2 Biological Background

The mathematical theory of coupled oscillators and the study of biological rhythms have a rich shared history, with breakthroughs in either field fueling innovations in the other. This exchange of ideas may be traced back to early studies of biological oscillations, where the study of daily cycles in behavior and physiologically inspired the development of a suite of mathematical tools for studying oscillatory phenomena [156, 123, 28]. Following in this tradition, daily or circadian rhythms are the principal biological application considered in my graduate work.

1.2.1 Whole Organism Studies

Circadian rhythms in behavior and physiology have been observed in every taxa of life ranging from single cellular organisms to plants, fungi, insects and mammals. Pioneering studies of circadian rhythms focused on characterizing circadian rhythms at the level of whole organisms, as localized circadian pacemakers were unknown prior to 1968 [28, 78, 139]. These studies characterized the sensitivity and precision of these rhythms using behavioral markers such as wheel-running activity in hamsters, perch hopping in finches or eclosion rhythms in *Drosophila* [122, 123]. Typically, researchers manipulated the environmental stimuli provided to the circadian cycle (e.g. light cycles, temperature cycles) and measured the effect on the marker rhythms to infer

the effect on the circadian clock [28].

Studies of circadian rhythms at the whole organism scale were vital in the development of the theory of entrainment [28]. Experimentally, it was discovered that circadian rhythms may be entrained to periods of slightly less than or greater than 24 hours, and that this entrainment range varies with the stimulus type, species, age, and light history of the organism [123, 28, 9]. Two competing hypothesis emerged to explain circadian entrainment known as parametric and non-parametric entrainment [29]. Non-parametric entrainment theory focuses on the phasic aspects of light input and posits that entrainment may be explained by the determination of the phase response curves to short stimuli [28]. While non-parametric entrainment focuses on tonic effects of light on the circadian cycle. Each of these theories have their merits, although the role of non-parametric entrainment is better understood [53]. Some of the strongest evidence for parametric entrainment is the changes in the circadian period of organisms kept in constant light conditions (τ_{LL}). By comparing the effects of constant light exposure among species, Jurgen Aschoff, discovered a trend that nocturnal animals generally show longer periods $\tau_{LL} > \tau_{DD}$, while diurnal animals show a period shortening under constant light $\tau_{LL} < \tau_{DD}$ [8].

In addition to being instrumental in developing a theory for circadian entrainment, whole organism studies also uncovered a large number of peculiar properties of circadian oscillators [122]. Especially important for this work are the so-called light entrainment after-effects [122]. After-effects describe stable changes observed in the free-running period τ (the circadian period as measured in an enviroment free from time cues) and may be distinguished from transient effects on the circadian period by their longer lasting effects and apparent quasi-stability [122]. For example, after-effects to large phase shifts in the light schedule may be observed in several species where large phase advances lead to an increase in the period and phase delays a decrease in the period [122]. Another prominent after-effect may be observed

when organisms are entrained to light schedules either longer or shorter than the free-running period of the organism. Entrainment to long periods leads to an increase in the free-running period, while entrainment to short periods show the opposite trend with a decrease in the free-running period [11, 122] . These entrainment after-effects were found to persist for 50-100 days following a release into free-running conditions [122].

Light entrainment after-effects may also be observed for light entrainment to varying photoperiods. The photoperiod of a light signal describes the fraction of the periodic cycle in which the organism is exposed to light. In a natural setting the photoperiod is short during winter days and lengthens in long summer days. Generally, when nocturnal mammals are entrained to long photoperiods they will show a shortened period when moved into darkness [122, 105]. Entrainment to light cycles with a short photoperiod leads to the opposite effect and organisms show a longer free-running period [122, 105].

Exposure to photoperiods of different lengths was also found to alter the response of the circadian circuit to brief light pulses. In particular, when organisms are exposed to long day-lengths the phase shifting response to light is seen to be attenuated [126, 147]. This attenuation effect and its relationship with the photoperiodic after-effect will be considered in Chapter IV.

1.2.2 The Master Circadian Clock

Crucially, whole organism studies of circadian rhythms led to a consensus three component definition of circadian rhythms. First, the rhythm must be endogenous, meaning it must persist in the absence of time cues and cycle with a period close to 24 hours. Secondly, the rhythm must be entrainable by external time cues called zeitgebers (german for "time givers"). Finally, the rhythm must be temperature compensated such that the period does not vary strongly with the ambient temperature.

This definition of circadian rhythms, together with technological advances, allowed for the genetic screens to be applied looking for mutations affecting the circadian phenotype. Genetic screens identified a host of "clock" genes involved in circadian timekeeping [78, 148]. The tools of molecular biology then revealed that circadian dynamics observed in whole organisms originate from a molecular clock at the single cell level [154]. This intricate genetic feedback loop produces molecular oscillations with a period of about 24 hours [92]. Simultaneously, neurobiologists searched for brain regions associated with circadian rhythms. In mammals, a small region of the anterior hypothalamus known as the Suprachiasmatic Nucleus (SCN) was found to house the master circadian clock [139]. From this neural command center the master clock sends out daily signals to a system of peripheral clocks located throughout the body [33].

Localization of the master circadian clock enabled the neural tissue to be excised and studied in culture [145]. The tools of electrophysiology could now be applied to study the neuronal properties of the clock cells. It was found that the firing rates of the clock neurons also vary in a circadian manner, with a peak firing rate near the middle of the circadian day [58, 56]. The organism level circadian rhythm is produced in an emergent manner through the aggregation of the molecular rhythms of the roughly twenty thousand clock neurons in the SCN.

In order to produce a coherent rhythm these clock neurons are coupled to one another through a large suite of neurotransmitters [87]. These coupling neurotransmitters act to oppose the tendency of intrinsic noise and heterogeneity in the individual clock neurons to cause the molecular clocks to desynchronize [86, 92]. Additionally, the coupling forces in the SCN establish a characteristic circadian waveform within the SCN tissue, allowing information to be encoded at a network level [39]. Changes in the environment conditions, such as the seasonal day-length, induce changes in this waveform allowing the SCN to act as a seasonal calendar as well as a daily clock [38,

105, 32]. Measurements of the changes in the circadian waveform may be integrated with the whole organism data describing how the changes in these same factors (environmental conditions, age, light history, zeitgeber character) affect the entrainment properties of the core circadian clock.

Studies of the structure of the SCN have revealed it may be functionally and physiologically clustered into two principal regions: the ventral (core) and dorsal (shell) phase clusters [45, 106]. These regions have been found to have distinct roles in determining the circadian waveform produced by the SCN holistically [39]. In addition to differences in the primary coupling forces between the ventral and dorsal SCN, a fundamental difference between these regions lies in the reception of light information. Photic information in mammals is channeled to the clock along a dedicated neural track from the retina. Interestingly, only a fraction of the clock neurons in the SCN are recipients of this light information largely located in the ventral SCN [98]. The consequences of this imbalance between the ventral and dorsal SCN in the reception of light information is examined in Chapters IV-V of this thesis.

CHAPTER II

Macroscopic Models of Coupled Biological Oscillators

2.1 Introduction

The study of coupled oscillators is important for many biological and physical systems, including neural networks, circadian rhythms and power grids [156, 43, 141]. Mathematical models of these coupled oscillator systems can be extremely high-dimensional, having at least as many degrees of freedom as the number of oscillators as well as additional dimensions for the coupling mechanisms between oscillators. However, this microscale complexity is belied by the elegant simplicity which emerges at the macroscopic scale in many coupled oscillator populations. Quite generally, these systems demonstrate a phase transition as the coupling between the oscillators is strengthened leading to the emergence of a self-organized synchronized state [157].

This emergence of a synchronized state from the dynamics of a very high-dimensional dynamical system, suggests that a low dimensional representation of this system should be possible. A major step in this direction was proposed by Art Winfree in 1967 when he intuitively grasped that for systems of weakly coupled, limit cycle oscillators the time evolution of each oscillator and the effects of coupling with its neighbors may be described by a single phase variable [158]. This method, known

as phase reduction, reduces the dimension of the coupled system to the number of constituent oscillators and has been used to analyze diverse coupled oscillator systems [86, 156, 130].

In the following years Kuramoto formalized the mathematical procedure for phase reduction and used it to derive his now famous model for N coupled heterogeneous oscillators,

$$\dot{\phi}_j = \omega_j + \frac{K}{N}\sum_{n=1}^{N}\sin(\phi_n - \phi_j), \qquad j = 1, N \tag{2.1}$$

where ϕ_j gives the phase of the jth oscillator, K is the coupling strength and ω_j gives the natural frequency of the oscillator [86]. The natural frequencies of the oscillators are typically assumed to be drawn from a distribution $g(\omega)$ which reflects the heterogeneity in the oscillator population. The Kuramoto model captures the essential features of many coupled oscillator systems and has been used to study the phase transition to synchrony in detail [142].

However, many biological systems contain thousands of oscillators, making even the phase model a very high-dimensional representation of the dynamical system. A recent breakthrough occurred when Ott and Antonsen discovered an ansatz that can be applied to a family of Kuramoto-like systems to derive a low-dimensional model for the macroscopic behavior of the coupled population [114]. When the ansatz is applied, the long-time behavior of a system of $N \to \infty$ heterogeneous oscillators can accurately be described by two differential equations, one for the mean phase of the coupled oscillators, and the other for their collective amplitude [113]. Despite the hundreds of recent papers that use the Ott-Antonsen dimension reduction procedure, the authors are not aware of any carefully done experiments to test whether this powerful ansatz holds for biological systems.

In this chapter we test the applicability of the Ott-Antonsen ansatz using a recent

experimental data set collected from neurons in the suprachiasmatic nucleus (SCN), the mammalian circadian pacemaker, and through simulations of several models of coupled biological oscillators [2]. We find that a core assumption of the Ott-Antonsen ansatz is not valid in our test systems. However, we find that a different, but related, ansatz more accurately describes the data. Using a simple argument, we demonstrate the validity of our ansatz for a wide-class of models. We then apply this ansatz to derive a two-dimensional macroscopic model for the population activity of a system of coupled, heterogeneous noisy oscillators. The generality of our procedure should allow for the derivation of low-dimensional macroscopic models of many coupled oscillator systems, allowing for fundamental insights into the core principles driving many biological phenomena.

2.2 Results

The development of the Ott-Antonsen ansatz initiated a revolution in the coupled oscillator literature [119]. The impact of their ansatz stems from the fact that the macroscopic equations exactly capture all the long-time attractors of the Kuramoto (Eq. 2.1) and closely related systems [113]. The ability to derive strong analytic results has led to its application to a vast array of application areas [94, 61, 102]. Recently, the Ott-Antonsen procedure was applied directly to the study of circadian rhythms for the first time [93].

The power of the Ott-Antonsen procedure comes at the price of several limitations. First, it may only be applied to systems where the interaction between the oscillators is described by a coupling function with a single harmonic [95]. Secondly, the ansatz is not valid for systems whose oscillators evolve with a stochastic component [136]. Each of these limitations could severely restrict its applicability to biological systems: complex coupling forces between biological oscillators often induce higher harmonic components in the model's coupling function [63, 15], and biological oscillators are

invariably subjected to noise [15].

A further limitation of the Ott-Antonsen procedure is one of practicality rather than a formal mathematical restriction. In its most powerful form, the Ott-Antonsen procedure requires the assumption that the distribution of natural frequencies of the oscillators be a rational function $g(\omega) = a(\omega)/b(\omega)$, which is typically taken to be a Cauchy (Lorentzian) distribution,

$$g(\omega) = \frac{\gamma}{\pi[(\omega - \omega_0)^2 + \gamma^2)]}, \tag{2.2}$$

where ω_0 is the median frequency and γ controls the strength of the heterogeneity in the oscillator population. Making this assumption on the frequency distribution is a crucial step in achieving the dimension reduction to the macroscopic model. For more general frequency distributions, the Ott-Antonsen procedure is still mathematically valid, although it produces an infinite set of integro-ordinary differential equations rather than the two-dimensional ordinary differential equation macroscopic model. Let us refer to the Ott-Antonsen reduction procedure with the additional assumption of a Cauchy distribution of frequencies as Cauchy Ott-Antonsen (COA).

The ansatz of the COA procedure takes a particularly simple form when written in terms of the Daido order parameters for the distribution of phases of the coupled oscillators. As seen in the introductory chapter, the Daido order parameters [31, 30] are given by,

$$Z_m(t) = R_m(t)e^{i\psi_m(t)} = \frac{1}{N}\sum_{j=1}^{N} e^{im\phi_j(t)}, \tag{2.3}$$

where ϕ_j are the phases of the oscillators, R_m are the phase coherences and ψ_m are the mean phases. Typically, only the first term is considered $Z_1 = R_1 e^{i\psi_1}$ and is known as the Kuramoto order parameter. Here R_1 measures the amplitude of the collective behavior of the oscillator population with $R_1 \approx 0$ indicating desynchrony

among the oscillators and $R_1 = 1$ perfect synchrony. The COA ansatz is a simple geometric relation between the Daido order parameters,

$$Z_m = (Z_1)^m \tag{2.4a}$$

$$R_m = R_1^m \qquad \psi_m = m\psi_1 \qquad \text{COA} \tag{2.4b}$$

When the phase distribution of the oscillators is unimodal and symmetric about its mean phase, we expect the mean phase relation $\psi_m = m\psi_1$ to hold generally, and we will focus on that case. However, the prediction that $R_m = R_1^m$ is more subtle and its accuracy has not been evaluated for biological systems.

To test the COA ansatz, we computed the Daido order parameters for a recently published data set measuring the approximate 24 hour oscillations of protein expression in neurons from whole SCN explants [2]. Phases were computed from hourly measurements of protein expression in individual neurons over a week long period as the neurons resynchronized following the application of a desynchronizing perturbation (see Methods). We examined this data set for evidence of the COA relation $R_m = R_1^m$ at each time point. We found that the phase coherences did not follow this relation (Fig. 2.1(A)). Additionally, numerical simulations of several different coupled populations of biological oscillator models also reveal the COA ansatz does not provide a good representation of the equilibrium phase coherences for these systems (Fig. 2.1(b-d)).

Instead, in each of these systems, we found that the relation,

$$R_m = R_1^{m^2} \qquad \psi_m = m\psi_1 \qquad m^2 \text{ ansatz} \tag{2.5}$$

better captures the properties of the phase distribution. We refer to this alternate scaling of the Daido order parameters as the m^2 ansatz.

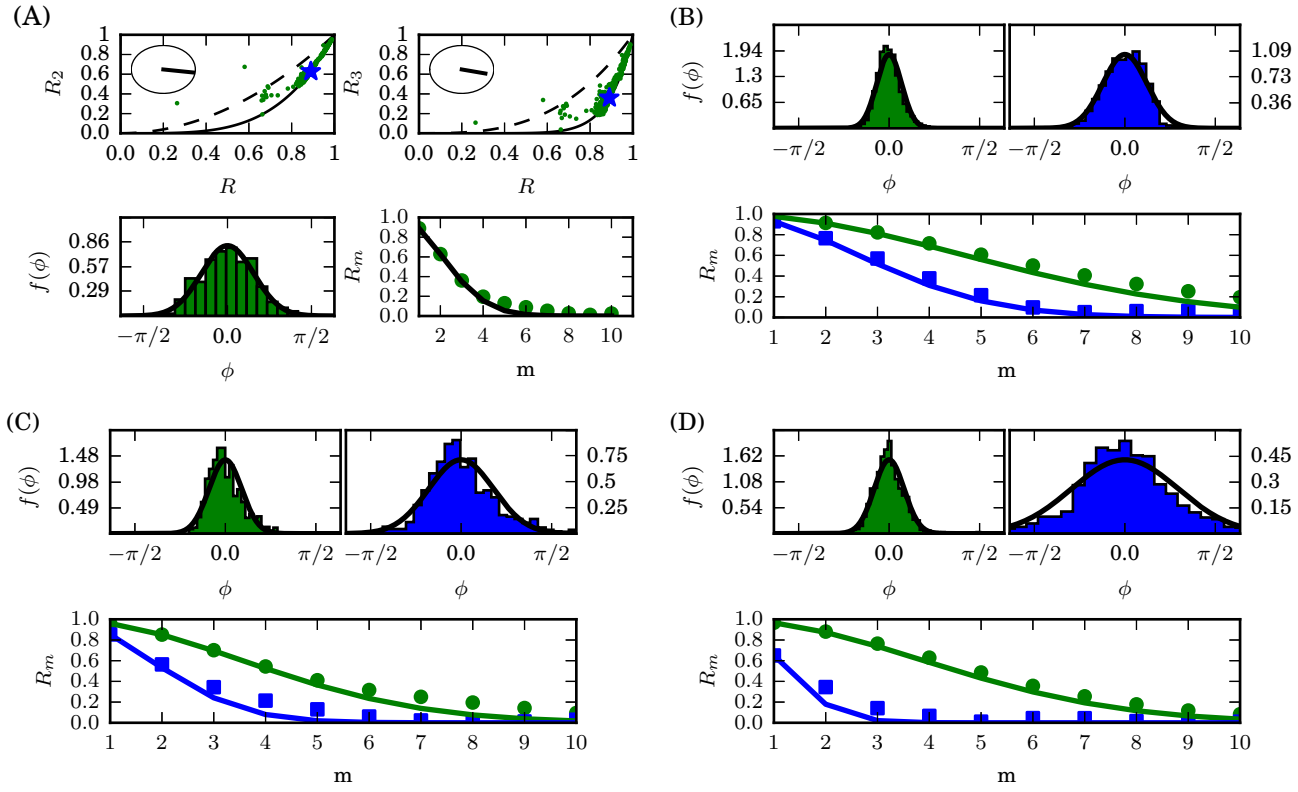

Figure 2.1: A low-dimensional structure in the phase distribution of coupled oscillator systems: (A) experimental SCN neuron data [2], (B) simulation of coupled heterogeneous Repressilator oscillators [50], (C) simulation of coupled heterogeneous Morris-Lecar neural oscillators, (D) simulation of coupled noisy modified Goodwin oscillators [76] (see Appendix A). (A) Top row: Green dots show the phase coherences computed from hourly measurements of cell protein expression in the SCN neurons. The solid black line shows the relation $R_m = R_1^{m^2}$ and the dashed line shows the COA ansatz $R_m = R_1^m$. Inset plots show the circular mean vector of $\psi_m - m\psi_1$ across all observations. Bottom row: Histogram (left) and first ten phase coherences (right) of the phase distribution computed from the data point indicated by the blue star in the top row panels, compared to the phase distribution satisfying the m^2 ansatz (black curves). Bottom right: The first ten phase coherences for the phase distribution computed from the data (green dots in top panels) compared to the m^2 ansatz relation (black curve). (B-D) Top row: Histogram of the simulated equilibrium phase distribution computed from model simulations for two different coupling strengths (left panel: strong coupling, right panel: weak coupling), compared to the m^2 ansatz phase distribution. Bottom row: The first ten phase coherences for the simulated equilibrium phase distributions for two coupling strengths (green dots = strong coupling, blue squares = weak coupling) compared to the m^2 ansatz relation (solid curves).

2.2.1 Emergence of the Scaling

The m^2 ansatz may be derived under more general assumptions than those required by the Ott and Antonsen procedure. Let us consider a population of N coupled oscillators with an equilibrium phase distribution ϕ_j^* such that $\phi_j^* \approx 0$ for $j = 1, 2 \ldots, N$. A Taylor series expansion of the Daido order parameters may be written as

$$Z_m \approx 1 + \frac{im}{N} \sum_{j=1}^{N} \phi_j^* - \frac{m^2}{2N} \sum_{j=1}^{N} (\phi_j^*)^2 + ... \tag{2.6a}$$

Making use of our assumption that the equilibrium phase distribution is unimodal and symmetric, we have that $\psi_m = m\psi_1$ and without loss of generality we may set $\psi_1 = 0$. Thus, introducing the notation $||\phi^*||_k^k = \sum_{j=1}^{N} (\phi_j^*)^k$ gives

$$R_m \approx 1 - \frac{m^2 ||\phi^*||_2^2}{2N} \approx \left(1 - \frac{||\phi^*||_2^2}{2N}\right)^{m^2}, \tag{2.7a}$$

$$R_m \approx R_1^{m^2}, \tag{2.7b}$$

which holds whenever the quantity $||\phi^*||_2^2$ can be considered small and justifies the emergence of the m^2 ansatz we found in both the experimental and simulated data (Fig. 2.1).

This analysis begs the question of how the COA ansatz $R_m = R_1^m$ and the m^2 ansatz can both be true. The root of the discrepancy is in the *fat-tails* of the Cauchy distribution for the natural frequencies of the oscillator population. The slow decay of the tails of the Cauchy distribution profile results in a significant fraction of oscillators whose phases are not locked to the mean phase but instead drift relative to the population rhythm. This effect keeps the quantity $||\phi^*||_2^2$ large for any finite coupling strength. However, for natural frequency distributions with exponential tails (e.g. Gaussian) the fraction of locked oscillators grows quickly as coupling strength

increases and the m^2 ansatz emerges for moderate coupling strengths. Fig. 2.2(a,b) shows the phase coherences for simulations of the Kuramoto system (Eq. 2.1) with Gaussian and Cauchy distributions of natural frequencies. Thus, we conclude the m^2 ansatz provides a close approximation for systems with natural frequency distributions with exponential tails, while the COA procedure provides an exact relation for systems with a Cauchy distribution of natural frequencies.

In fact, we may introduce a correction to our ansatz which takes into account the presence of phase-locked and phase-drifting oscillators in the population. Let p be the fraction of the population whose phases are locked to the mean phase. Then the Daido order parameters can be expressed as $Z_m = pZ_m^{locked} + (1-p)Z_m^{drift}$ and $|Z_m^{drift}| \approx 0$ for the drifting population. Then the same Taylor-series based argument in Eqs. 2.6 and 2.7 considering only the contribution of the locked population gives,

$$R_m \approx \frac{R_1^{m^2}}{p^{m^2-1}}, \tag{2.8}$$

which collapses to Eq. 2.7b as $p \to 1$. Additionally, this analysis shows that assuming $p = 1$ gives a lower-bound on the Daido order parameter. In particular, $R_m \geq R_1^{m^2}$ and $R_m \to R_1^{m^2}$ as $p \to 1$. For the Kuramoto model (Eq. 2.1) we may calculate the fraction of phase-locked oscillators as the coupling strength increases $p(K)$ as [86, 142]

$$p(K) = \int_{-KR_1}^{KR_1} g(\omega) d\omega. \tag{2.9}$$

For the Kuramoto model with Gaussian or Cauchy distributions of oscillator natural frequencies $g(\omega)$, we may solve for $p(K)$ using Eq. 2.9. The comparatively slow growth of the fraction of locked oscillators as K increases for the Cauchy distribution relative to a Gaussian distribution of natural frequencies is shown in Fig. 2.2(c).

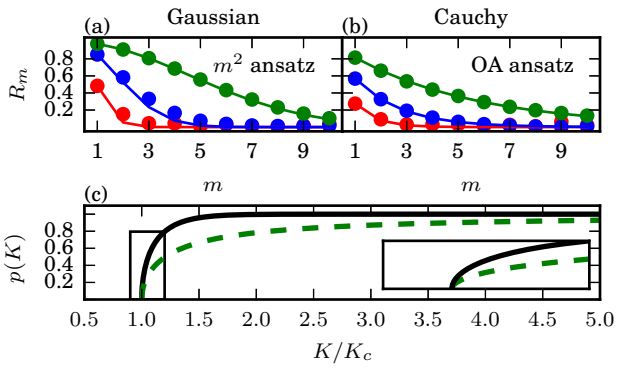

Figure 2.2: The Kuramoto model (Eq. 2.1) with Gaussian and Cauchy distributions for the natural frequencies of the oscillators, $g(\omega)$. (a,b) Relation among the Daido order parameters computed from numerical simulations (circles) and predicted (curves) by (a) the m^2 ansatz for Gaussian $g(\omega)$ and (b) the COA ansatz for Cauchy $g(\omega)$ for increasing coupling strength. Colors indicate different coupling strengths K normalized to the critical coupling strength K_c where partially synchronized solutions emerge [86, 142]: $K/K_c = 1.1$ (red), $K/K_c = 1.5$ (blue) and $K/K_c = 3.0$ (green). (c) The fraction of oscillators phase-locked to the mean phase p as a function of normalized coupling strength K/K_c for a Cauchy (dashed green) and Gaussian (solid black) $g(\omega)$.

2.2.2 Complex Networks and Noise

The simplicity of our derivation makes it clear the m^2 ansatz should hold quite generally. In this section we characterize its emergence for the case of systems with complex network coupling and intrinsically noisy oscillators. To explore this, we consider a model network of N noisy heterogeneous phase oscillators,

$$\dot{\phi}_i = \omega_i + \frac{K}{d_i}\sum_{j=1}^{N} A_{ij} H(\phi_j - \phi_i) + \sqrt{D}\eta_i(t), \tag{2.10}$$

where η_i is a white noise process with $\langle \eta_i \rangle = 0$ and $\langle \eta_i(t)\eta_j(t') \rangle = 2\delta(t-t')\delta_{ij}$, where δ_{ij} is the Kronecker delta. Network connectivity is defined by the adjacency matrix A and we assume an undirected network such that A is symmetric and $A_{ij} = A_{ji} = 1(0)$ if oscillators i and j are coupled (uncoupled). The degree of the oscillator is then given by $d_i = \sum_{j=1}^{N} A_{ij}$. Let the coupling function H be a 2π periodic function and

we assume that $H'(0) > 0$. We note that Eq. 2.10 is quite general and may be derived in many applications from higher dimensional, limit cycle oscillator network models under the assumption of weak coupling [7].

We consider the case of strong coupling between the oscillators such that, $\phi_j - \phi_i \approx 0$ for all oscillator pairs. In this case, we can linearize about the phase-locked state to give

$$\dot{\phi}_i = \tilde{\omega}_i - KH'(0)\sum_{j=1}^{N} L_{ij}\phi_j + \sqrt{D}\eta_i(t), \tag{2.11}$$

where L is a normalized Laplacian matrix given by $L_{ij} = \delta_{ij} - A_{ij}/d_i$ and $\tilde{\omega_i} = \omega_i + KH(0)$. Our assumptions on the network connectivity dictate that L has real eigenvalues that may be ordered $\lambda_1 = 0 \leq \lambda_2 \leq ...\lambda_N$ with associated eigenvectors $\{\mathbf{v}_1, ..., \mathbf{v}_N\}$. For the linear system (Eq. 2.11) in the absence of noise ($D \to 0$) we may solve for the deterministic steady state ϕ^* using the Moore-Penrose pseudoinverse of the normalized Laplacian $L^\dagger$,

$$\phi^* = \frac{L^\dagger \tilde{\omega}}{KH'(0)}, \quad \text{with} \quad L^\dagger = \sum_{j=2}^{N} \frac{\mathbf{v}_j \mathbf{v}_j^T}{\lambda_j}. \tag{2.12}$$

Allowing for stochastic fluctuations about the deterministic steady state ϕ^*, we may compute the quantity $\mathbb{E}\left[||\phi^*||_2^2\right]_t$ as,

$$\mathbb{E}\left[||\phi^*||_2^2\right]_t = \sum_{j=2}^{N}\left[\left(\frac{|\mathbf{v}_j \cdot \tilde{\omega}|}{\lambda_j KH'(0)}\right)^2 + \frac{D}{\lambda_j KH'(0)}\right], \tag{2.13}$$

where details of this derivation are given in Appendix A. If the quantity $\mathbb{E}\left[||\phi^*||_2^2\right]_t$ is small, then our expansion of the Daido order parameters (Eq. 2.7a) tells us that the m^2 ansatz will provide a good approximation for the phase distribution. Thus, considering Eq. 2.13 we see that the m^2 ansatz will hold for sufficiently strong coupling strengths for any connected network where $||\tilde{\omega}||$ is finite. Additionally, Eq. 2.13 can be

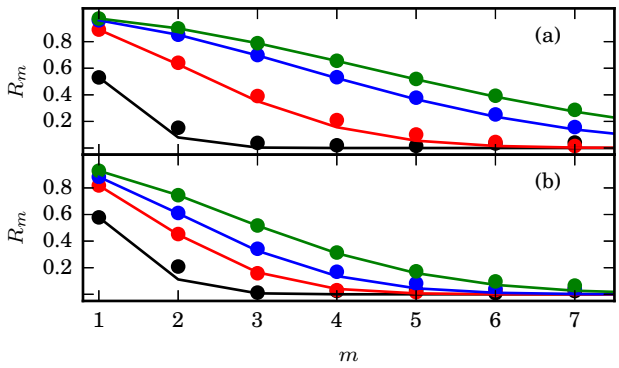

Figure 2.3: The equilibrium phase distribution of complex network phase oscillators converges to the m^2 ansatz as the coupling strength between the oscillators increases: (a) Barabasi-Albert Scale-Free network (b) Watts-Strogatz Small World network. Circles show the results from simulations of networks of $N = 1000$ coupled oscillators with noise amplitude $D = 1$ and oscillator frequencies drawn from a Gaussian distribution with $\sigma = 1$. Solid lines show $R_m = R_1^{m^2}$. Colors indicate different coupling strengths as in Fig. 2.2. Details of these simulations are given in Appendix A

used to study how the emergence of the ansatz depends on the network connectivity, noise strength and the arrangement of the heterogeneous frequencies in the network [133].

These results are confirmed by numerical simulations of Eq. 2.10 for the noisy, heterogeneous Kuramoto model (where $H(\theta) = \sin(\theta)$) with different network connectivity topologies (Fig.2.3). In particular, we find the m^2 ansatz provides a quality approximation to the Daido order parameters for both Watts-Strogatz small world [153] and Barabasi-Albert scale-free [12] network topologies. For each network topology, the accuracy of the approximation increases with the strength of the coupling as predicted by Eq. 2.13.

2.2.3 Macroscopic Model

A principal strength of the Ott-Antonsen approach is that the dynamics of the Kuramoto model (Eq. 2.1) for a large system of coupled oscillators can be reduced

to the following two dimensional macroscopic model [114]:

$$\dot{R}_1 = \left(\frac{K}{2} - \gamma\right) R_1 - \frac{K}{2} R_1^3 \tag{2.14a}$$

$$\dot{\psi}_1 = \omega_0, \tag{2.14b}$$

where w_0 is the median frequency of the oscillators and γ is the dispersion parameter of the Cauchy distribution of natural frequencies (Eq. 2.2). In this section, we apply the m^2 ansatz to extract a similar macroscopic model for a large network of noisy, heterogenous oscillators. In particular, we employ the m^2 ansatz as a motivated moment closure to extract a macroscopic model for the order parameter Z_1 for the noisy heterogeneous Kuramoto equation (Eq. 2.10). We consider a fully-connected network with coupling function $H(\theta) = \sin(\theta)$. Under these conditions we may write the system using the Kuramoto order parameter $Z_1 = R_1 e^{i\psi_1}$ [86],

$$\dot{\phi}_i = \omega_i + K R_1 \sin(\psi_1 - \phi_i) + \sqrt{D}\eta_i(t). \tag{2.15}$$

Following the Ott-Antonsen procedure [114] we consider the continuum limit $N \to \infty$ of Eq. 2.15 and find the continuity equation for the phase density function $f(\omega, \phi, t)$

$$\frac{\partial f}{\partial t} + \frac{\partial}{\partial \phi}(fv) + D\frac{\partial^2 f}{\partial \phi^2} = 0, \tag{2.16a}$$

$$v = \omega + K\,\mathrm{Im}[e^{-i\phi} Z_1], \tag{2.16b}$$

where Im denotes the imaginary part of the expression. The Fourier series decomposition of f is given by

$$f = \frac{g(\omega)}{2\pi}\left(1 + \left[\sum_{n=1}^{\infty} A_n(\omega, t) e^{in\phi} + \text{c.c.}\right]\right), \tag{2.17}$$

where c.c. stands for the complex conjugate of the expression and $g(\omega)$ is the distribution of natural frequencies of the oscillators. Substitution of the Fourier series for f into the continuity equation yields

$$\frac{\dot{A}_n}{n} + (i\omega + Dn)A_n + \frac{K}{2}\left(Z_1 A_{n+1} - \bar{Z}_1 A_{n-1}\right) = 0. \tag{2.18}$$

where barred quantities are the complex conjugate. In the continuum limit the Daido order parameters Z_m are given by

$$Z_m(t) = \int_0^{2\pi}\int_{-\infty}^{\infty} f(\omega,\phi,t)e^{im\phi}d\omega d\phi \in \mathbb{C} \tag{2.19a}$$

$$= \int_{-\infty}^{\infty} \bar{A}_m(\omega,t)g(\omega)d\omega, \tag{2.19b}$$

using that all oscillating terms in the Fourier series for f integrate to zero except for $n = m$. It is at this point in the Ott-Antonsen procedure where the assumption of a Cauchy distribution of natural oscillator frequencies becomes important. If $g(\omega)$ is given by a Cauchy distribution with median ω_0 and dispersion parameter γ (Eq. 2.2), the integral (Eq. 2.19b) can be evaluated as a residue by arguing that $A_m(\omega,t)$ may be analytically continued into the lower half of the ω plane [114]. To continue the derivation of the macroscopic model, we assume a Cauchy distribution of natural frequencies and obtain $Z_m(t) = \bar{A}_m(\omega_0 - i\gamma, t)$. Using this substitution for the Daido order parameters allows us to re-write Eq. 5.9 as follows

$$\frac{\dot{Z}_n}{n} = (i\omega_0 - \gamma - Dn)Z_n + \frac{K}{2}(Z_1 Z_{n-1} - \bar{Z}_1 Z_{n+1}). \tag{2.20}$$

Finally, we set $n = 1$ and apply the moment closure $Z_m = |Z_1|^{(m^2-m)}Z_1^m$ or $R_m = R_1^{m^2}, \psi_m = m\psi_1$, which yields an equation of motion for the Kuramoto order param-

eter $Z = Z_1$,

$$\dot{Z}_1 = (i\omega_0 - \gamma - D)Z_1 + \frac{K}{2}\left(Z_1 - |Z_1|^2(Z_1)^2\bar{Z}_1\right) \tag{2.21}$$

Separating the real and imaginary parts $Z_1 = R_1 e^{i\psi_1}$ gives the macroscopic equations

$$\dot{R}_1 = \left(\frac{K}{2} - D - \gamma\right) R_1 - \frac{K}{2}R_1^5 \tag{2.22a}$$

$$\dot{\psi}_1 = \omega_0. \tag{2.22b}$$

In previous work, Sonnenschein and Schimansky-Geier [136] derived Eq. 2.22 for the special case of the noisy Kuramoto model assuming homogeneous oscillator frequencies ($\gamma \to 0$) by employing an ad-hoc Gaussian moment closure on the phase distribution. Interestingly, the Gaussian moment closure follows the m^2 ansatz found here. In agreement with our findings, they found the macroscopic system (Eq. 2.22) captured the dynamics of the microscopic noisy homogeneous Kuramoto model accurately, particularly at strong coupling strengths [136] .

Here, we find the m^2 ansatz provides an accurate approximation for the macroscopic dynamics of the noisy heterogeneous Kuramoto model. In Fig. 2.4 we show the predictions of the macroscopic model (Eq. 2.22) compared to numerical simulations of the microscopic model in the continuum limit found by using the first fifty moments of Eq. 5.11[136].

In the limit of zero noise amplitude ($D \to 0$), the accuracy of the m^2 ansatz breaks down under the assumption of a Cauchy distribution of oscillator natural frequencies. This is to be expected given that the zero noise limit of Eq. 4.5 has been proven to follow the COA ansatz $R_m = R_1^m$ [113]. However, in the case of weak to moderate heterogeneity relative to the noise strength $s = \gamma/D \leq 1$ we find the m^2 ansatz also

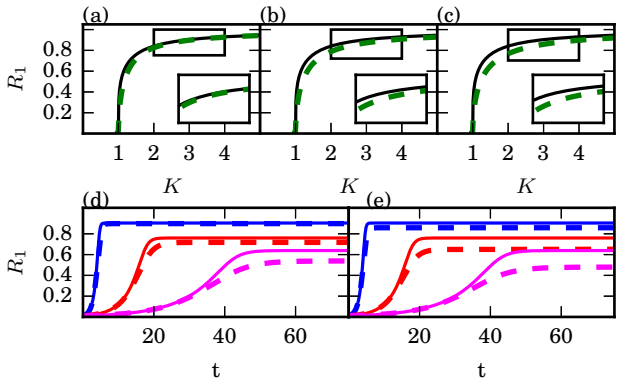

Figure 2.4: The equilibrium phase coherence R_1 as a function of the coupling strength K for the noisy, heterogeneous Kuramoto model (Eq. 2.15) for different relative levels of heterogeneity (γ) and noise amplitude (D) (a) $s = \gamma/D = 0.05$ (b) $s = 0.5$ (c) $s = 1$. (d-e) The transient dynamics of R_1 for (d) s=0.05 and (e) s=1.0 for different coupling strengths: $K = 1.2$ (magenta), $K = 1.5$ (red) and $K = 3.0$ (blue). In all panels, solid curves show the macroscopic model predictions (Eq. 2.22) and dashed curves show numerical simulations of the microscopic model in the continuum limit (Eq. 5.11). Parameters chosen such that critical coupling strength $K_c = 1$ for the microscopic model. Insets show curves in the rectangular regions.

provides an accurate description of the macroscopic dynamics (Fig. 2.4). Moreover, we find the m^2 ansatz provides a useful upper-bound for the collective amplitude R_1 and the accuracy improves with increased coupling strength. This may be explained by our result that $R_m \geq R_1^{m^2}$ and that $R_m \to R_1^{m^2}$ as the entire oscillator population is locked to the mean-field.

As discussed above, the breakdown of the m^2 ansatz is related to the fat-tails of the Cauchy distribution, which cause the fraction of oscillators locked to the mean-field to grow slowly as coupling strength increases. If the natural frequency heterogeneity has less density in the tails of the distribution, our analysis predicts the m^2 ansatz should become more accurate. In the next section we investigate how the m^2 ansatz may be used to derive macroscopic models for systems with strong heterogeneity and exponential tails.

Oscillator Heterogeneity

In the derivation of the macroscopic model for the noisy Kuramoto system (Eq. 2.22), we achieved the dimension reduction by assuming that the oscillator frequency distribution $g(\omega)$ took the form of a rational function, specifically the Cauchy distribution (Eq. 2.2). However, our analysis has shown that the m^2 ansatz is best applied to frequency distributions with exponential tails. For a general frequency distribution $g(\omega)$, the m^2 ansatz may be applied using

$$Z_1(t) = \int_{-\infty}^{\infty} \bar{A}_1(\omega, t) g(\omega) d\omega \tag{2.23a}$$

$$Z_m = |Z_1|^{m^2-m} Z_1^m. \tag{2.23b}$$

However, without further simplification the advantage of our approach is largely negated as this is an infinite set of integro-differential equations which yield an approximate solution. In this section, we derive an approximate two-dimensional macroscopic model for systems where oscillator frequencies follow a general symmetric, unimodal distribution.

For a general symmetric and unimodal distribution of oscillator frequencies $g(\omega)$ with a maximum at ω_0, we can approximate it with a Cauchy distribution $g_c(\omega, \gamma)$. Let $h(\omega, \gamma) = g(\omega) - g_c(\omega, \gamma)$, then the solution to Eq. 2.23a is

$$Z_1(t) = \bar{A}_1(\omega_0 - i\gamma, t) + E_1(\gamma, t) \approx \bar{A}_1(\omega_0 - i\gamma, t) \tag{2.24a}$$

$$E_1(\gamma, t) = \int_{-\infty}^{\infty} \bar{A}_1(\omega, t) h(\omega, \gamma) d\omega. \tag{2.24b}$$

Thus, the approximation for Z_1 in Eq. 2.24a allows for the dimension reduction and the accuracy of the macroscopic model will depend on choosing the dispersion parameter $\gamma = \hat{\gamma}$ such that the magnitude of the error term $|E_1(\gamma, t)|$ is minimized. The m^2 ansatz yields the higher order Daido order parameters with error $\mathcal{O}(E_1)$ using

Eq. 2.23b.

To compute the error term $|E_1(\gamma, t)|$, consider the function $A_1(\omega, t) \in \mathbb{C}$ as a frequency-dependent version of the Kuramoto order parameter Z_1. For oscillators which are entrained to the mean-field we may write

$$A_1(\omega, t) = \rho(\omega) e^{i(\theta(\omega)+\Omega t)}, \tag{2.25}$$

where Ω gives the frequency of the mean-field, $\rho(\omega)$ describes the collective amplitude and $\theta(\omega)$ the entrainment angle for oscillators with natural frequency ω. When oscillators with frequency ω are locked to the mean-field we have $\rho(\omega) = 1$ [112].

For the Kuramoto model, oscillators with $\omega \leq KR_1$ are locked to the mean-field with entrainment angle $\theta(\omega) = \arcsin(\frac{\omega}{KR_1}) \approx \frac{\omega}{KR_1}$. Therefore we may approximate the magnitude of the error integral by considering only the locked oscillators

$$|E_1(\gamma)| \approx |L_1(\gamma)| = \left| \int_{-KR_1}^{KR_1} e^{i\frac{\omega}{KR_1}} h(\omega, \gamma) d\omega \right|. \tag{2.26}$$

Thus, $\hat{\gamma}$ should be chosen such that $|L_1(\gamma)|$ is minimized. For example, for a Gaussian distribution of frequencies it is possible to find $\hat{\gamma}$ such that $|L_1(\hat{\gamma})| = 0$. In general, $\hat{\gamma}$ will depend on the coupling strength K both directly and implicitly through $R_1(K)$.

Therefore, the approximate macroscopic model for the heterogeneous Kuramoto model is

$$\dot{R}_1 = \left(\frac{K}{2} - \hat{\gamma}(K) \right) R_1 - \frac{K}{2} R_1^5 \tag{2.27a}$$

$$\dot{\psi} = \omega_0. \tag{2.27b}$$

For $KR_1 \approx 0$ we may solve for $\hat{\gamma}$ by setting $|h(\omega_0, \hat{\gamma})| = 0$ which yields $\hat{\gamma} = 1/[\pi g(\omega_0)]$. Therefore, the approximate macroscopic model captures the critical coupling strength $K_c = 2\hat{\gamma}$ as determined by the classical self-consistency approach reviewed in the

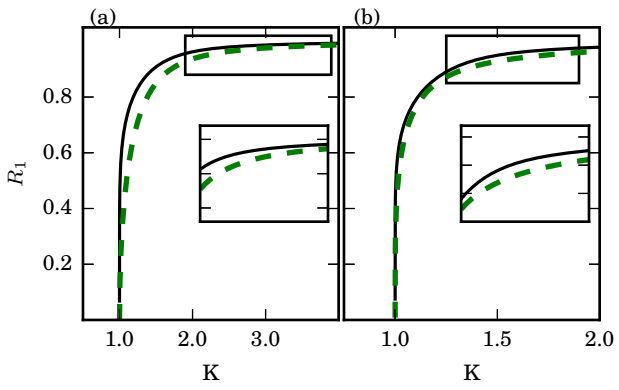

Figure 2.5: The equilibrium phase coherence R_1 against the coupling strength K for the Kuramoto model for (a) $g(\omega)$ Gaussian (b) $g(\omega) \propto e^{-\omega^4/a}$ distributions of natural frequencies. Exact solutions obtained from classical self-consistency theory [86, 142] are shown as dashed green, and the solution according to the m^2 ansatz solid black

introductory chapter [142, 86]. Moreover, we find the macroscopic model (Eq. 2.27) provides a close approximation to $R_1(K)$ as the coupling strength increases as shown in Fig. 2.5 for $g(\omega)$ Gaussian and $g(\omega) \propto e^{-\omega^4/a}$.

Finally, we note that the error in the approximation in Eq. 2.26 for the error term $|E_1(\gamma)|$ scales with the fraction of locked oscillators p. Thus, the approximation of a Cauchy frequency distribution and the m^2 ansatz each introduce errors which scale with the fraction of locked oscillators. Therefore, employing the Cauchy approximation alongside the m^2 ansatz does not add any additional assumptions to the approximation and does little to affect the accuracy of the approach.

2.3 Discussion

In the past decade, the powerful ansatz discovered by Ott and Antonsen [114] has been used to resolve many open problems in the coupled oscillator literature and has been applied to an increasing number of application areas [94, 102, 93]. In this chapter, we provide the first evaluation of the suitability of the Ott-Antonsen reduction procedure for extracting macroscopic models of real biological networks.

Our examination of a recent experimental data set of circadian oscillator activity

[2], as well as simulations of several biological oscillator networks, revealed that these systems did not follow the Ott-Antonsen ansatz. Instead, we identified a new relation, the m^2 *ansatz*, which captures the phase distribution of these systems more accurately.

A simple argument showed the emergence of the m^2 ansatz for systems of coupled oscillators which have a high percentage of the oscillators phase-locked to the mean-field oscillation. We found the m^2 ansatz emerged at moderate coupling strengths for oscillator populations whose frequency heterogeneity has exponential tails. In contrast, the Ott-Antonsen ansatz holds at any coupling strength when the frequency heterogeneity has a Cauchy distribution (polynomial tails). For noisy heterogeneous coupled oscillator systems, the m^2 ansatz robustly emerged for sufficiently strong coupling strengths. Further, the m^2 ansatz may be used as a moment closure to extract a low-dimensional macroscopic model for noisy heterogeneous oscillator networks.

The low-dimensional system we derive differs slightly from the Ott-Antonsen approach as it produces a term of order R^5 in the collective amplitude equation as compared with the cubic scaling R^3 in the Ott-Antonsen equations [114, 93]. We note that a cubic scaling is expected for coupling strengths near the critical coupling strength K_c as predicted by the normal form for a Hopf bifurcation [60]. Therefore, we expect our ansatz would overestimate the growth of the phase coherence about the critical coupling strength and may not be an appropriate tool for studying the scaling of the order parameter about the critical coupling. However, as we demonstrated, our approach provides a close approximation to the equilibrium phase coherence as the coupling between oscillators is strengthened.

In the case of human circadian rhythms, several results suggest that models for collective amplitude dynamics should include higher order terms. For example, higher-order terms in the amplitude growth have previously been required to accurately model the collective amplitude dynamics of the human circadian rhythm in response to a desynchronizing light-pulse [68]. Additionally, the R^5 term which appears in

our model predicts it should be difficult to increase the amplitude of the circadian rhythm by applying light pulses to an equilibrium circadian amplitude. This is in accordance with experimental results that light pulses administered during the day do not significantly affect the circadian amplitude [69, 71]. Finally, we note that a previous comparison of two phenomenological van der Pol models for human circadian rhythms showed that the model with higher order terms better explained human circadian amplitude data [67].

A principal strength of both the Ott-Antonsen procedure and our results is that the parameters and variables of the derived macroscopic models have direct physical interpretations. Therefore, the predictions of the models may be compared with experimental data from the cellular, tissue and whole organism levels. For example, Lu et al [93] made use of the COA ansatz to study jet-lag resynchronization asymmetry using readily available data on the mean-period of circadian oscillator cells [16, 27]. Future work could use this formalism to synthesize cellular-level data on the coupling mechanisms[105], network connections [2] and cellular periods [106] of SCN neurons with behavioral circadian abnormalities observed at the whole organism level. We will apply the m^2 ansatz to study the impact of light on the mammalian circadian rhythm in Chapter IV and to derive a low-dimensional model for human circadian rhythms in Chapter V.

To conclude, the m^2 ansatz allows derivations of macroscopic models for populations of oscillators with more general frequency distributions and phase-locked behavior than required by the COA ansatz. Our analysis of the phase-locked dynamics of neurons in the mammalian circadian pacemaker suggest that other biological oscillator systems may also be better represented by the m^2 ansatz.

2.4 Methods

The circadian time-series shown in Fig. 2.1(a) was collected as described by Abel et al [2], who generously made their data set publicly available. Briefly, the time-series was collected from whole SCN mouse explants cultured for 14 days. The expression of the circadian marker PERIOD2::Luciferase was monitored under a microscope, with bioluminescence measurements collected every hour. On day six in culture tetrotoxin (TTX) was added to the culture in order to block neuronal signaling and desynchronize the neurons. The TTX solution was washed away and the culture was allowed to resynchronize. For our purposes we removed the time-points when the TTX solution was added in order to study the phase distribution of the coupled neurons during resynchronization. Plots of additional SCN explants adherance to the m^2 ansatz are shown in Appendix A.

The raw bioluminscience data were processed following established methods [106]. First, the raw bioluminscience data was de-trended by removing the Hodrick-Prescott baseline trend with a large penalty parameter $\lambda = 10^6$ to minimize loss of the oscillatory signal component. The time-dependent protophase of each oscillator was extracted by dimensional embedding with an six hour embedding lag [134]. Finally, the time-dependent phase was estimated using the protophase to phase transformation as specified in the DAMOCO Matlab toolbox [83, 82].

Details for the mathematical models used in Fig. 2.1(b-d) are given in Appendix A. The estimation of the phase distribution for the *in silco* data was carried out in much the same manner as described for the experimental data. However, due to the large number of data points available in the simulated data we used the Hilbert transform to estimate the protophase of the oscillators.

CHAPTER III

Collective Phase Response Curves for Heterogeneous Coupled Oscillators

3.1 Introduction

Many biological rhythms are produced in a collective manner by a large ensemble of coupled heterogeneous oscillators. For example, the mammalian circadian clock consists of approximately twenty thousand coupled heterogeneous neuronal oscillators [92]. The collective oscillation produced by the ensemble of individual neurons drives the behavioral circadian rhythm [92]. Similar phenomena have been observed in the generation of brain rhythms, cardiac pacemaker cells, and many other biological systems [55, 116, 51].

For weakly coupled limit-cycle oscillators the dynamics of each oscillator may be reduced to a single phase variable and the collective properties of the system may be revealed through the study of the coupled phase equations [86, 135, 158]. One of the best characterized systems of coupled phase oscillators is the mean-field Sakaguchi-Kuramoto model [142, 86]. In this model the oscillators are assumed to be all-to-all coupled through a sinusoidal coupling function. The existence, stability and phase distribution of the synchronized state in the Sakaguchi-Kuramoto equations has been the subject of extensive mathematical investigation [142, 4]. In particular, several

dimension-reduction techniques have been developed for this system which allow for analytical investigation [114, 54, 120, 152, 22].

The properties of oscillating systems are often studied both experimentally and theoretically by characterizing their response to perturbations applied at different phases in the oscillation [72, 135]. Commonly, the effect of the perturbation is measured in terms of a phase shift and the resulting curve is termed a phase response curve (PRC).

For a single oscillator, the (microscopic) PRC is well defined both mathematically and experimentally and can provide insights into the stability, synchronization and entrainment behaviors of the oscillator [130, 156, 118]. Of particular importance are the amplitude and zeros of the PRC. For entrainment by a weak resetting signal, the amplitude of the PRC determines the range of frequencies the oscillator can entrain to and the stable zeros give the phase difference between the entraining force and the oscillator [118].

Comparatively little is known about the (macroscopic) collective phase response curve. Here, an external stimulus perturbs each individual oscillator which induces a phase shift according to the microscopic PRC. These microscopic shifts interact to produce a macroscopic shift in the collective rhythmicity of the population. The phase shift in the macroscopic phase gives the collective PRC for the ensemble of oscillators.

For a population of oscillators with identical phases the collective and microscopic phase PRCs will coincide. However, when the oscillator population has some variance in the phase distribution, the collective PRC will generally differ from the microscopic PRC [156]. A central question is how the collective and the microscopic PRCs may be related for a population of heterogeneous oscillators.

Mathematically, several factors have been identified which can lead to significant differences between the microscopic and collective PRCs. The nature of the coupling

function as well as the connectivity between the individual oscillators is known to have important effects on how the collective PRC differs from the microscopic PRC [81]. The effect of a general network structure on the collective PRC is discussed in [81] for the case of small deviations from a global limit cycle attractor. Furthermore, the effect of a non-odd coupling function on collective phase shifts is examined in Levnajic and Pikovsky [89] using the Ott-Antonsen dimension reduction technique [114, 113]. The effect of non-odd coupling functions is also examined in Ko and Ermentrout [77] using symmetry properties of the coupling function. Moreover, the phase distribution of the ensemble of oscillators is known to effect the shape of the collective PRC [156].

In this work, we consider an all-to-all coupled network and focus on the effect of the phase distribution and the coupling function in determining the collective PRC. We study a globally coupled system of Sakaguchi-Kuramoto oscillators with a non-odd sinusoidal coupling function. Each individual oscillator experiences an instantaneous phase shift according to a microscopic PRC-where we make no assumptions on the form of the microscopic PRC. We analytically determine an asymptotic expansion for the collective phase response curve making use of the formalism developed in [89] based on the Ott-Antonsen reduction [114, 113].

The resulting analytical formula reveals the effect of heterogeneity. The formula predicts the collective PRC differs from the microscopic PRC by an amplification of the first harmonic and dissipation of the higher harmonics. In addition, an important effect of coupling is shown to be a shift in the zeros of the collective PRC. Significantly, these results give a characteristic scaling for the amplitude and change in the zeros of the collective PRC as a function of the mean phase coherence of the system. We also derive the instantaneous amplitude response function for the coupled system which characterizes the transient effect of perturbations on the phase coherence of the system.

Our work builds upon that of Levnajić and Pikovsky [89] in that we consider general microscopic phase response curves and derive a characteristic scaling for the collective phase response curve. We also focus on the deterministic case, whereas in Refs. [73, 74] they consider a stochastic system.

This chapter is organized as follows: in Sec. 3.2 we define the model to be studied, components of the collective phase response curve and the Ott-Antonsen reduction approach. In Sec. 3.3 we derive an asymptotic formula for the collective phase response curve. In Sec. 3.4 we test the analytical theory against numerical simulations for phase oscillators. In Sec. 3.5 we demonstrate the applicability of the theory to biological systems by studying a population of coupled neuronal oscillators. The results and conclusions are discussed in Sec. 3.6.

3.2 Formulation of the Model

3.2.1 Model Definition

We consider an ensemble of N heterogeneous oscillators characterized by their natural frequencies ω_k and whose dynamical states may be described as phase variables ϕ_k, $k = 1, 2...N$. Further we assume a Sakaguchi-Kuramoto type sinusoidally coupled system where each individual oscillator responds to a instantaneous perturbation according to a microscopic phase response curve $Q(\phi)$:

$$\dot{\phi_k} = \omega_k + \frac{K_0}{N}\sum_{j=1}^{N}\sin(\phi_j - \phi_k + \beta) + \epsilon Q(\phi_k)\delta(t - t') \tag{3.1}$$

for $\beta \in (\frac{-\pi}{2}, \frac{\pi}{2})$. The ϵ parameter will be used to control the magnitude of the phase shifts. The collective dynamical state of the ensemble is described through the set of

Daido order parameters Z_n defined according to [31, 30],

$$Z_n = \frac{1}{N}\sum_{k=1}^{N} e^{in\phi_k} \in \mathbb{C}. \tag{3.2}$$

When $n = 1$ we refer to $|Z_1| = R$ as the phase coherence of the system and $Arg(Z_1) = \psi$ as the mean or collective phase. The collective PRC will be expressed as a function of the mean phase ψ. In the limit as $N \to \infty$ we may convert Eq. (3.1) to a partial differential equation for the continuous density function $f(\omega, \phi, t)$ such that $f(\omega, \phi, t)d\phi d\omega$ gives the fraction of oscillators at phase ϕ with natural frequency ω at time t. The continuity equation as $N \to \infty$ is given by,

$$\frac{\partial f}{\partial t} + \frac{\partial}{\partial \phi}\left[f(\omega, \phi, t)v\right] = 0, \tag{3.3a}$$

$$v = \omega + K_0 Im[e^{i\beta}e^{-i\phi}Z] + \epsilon Q(\phi)\delta(t - t'). \tag{3.3b}$$

The generalized Daido order parameter Z_n for a continuous density function is given by,

$$Z_n(t) = \int_{-\pi}^{\pi}\int_{-\infty}^{\infty} f(\omega, \phi, t)e^{in\phi}d\omega d\phi \in \mathbb{C}. \tag{3.4}$$

Finally, we assume the distribution of natural frequencies follows a Cauchy distribution with mean ω_0 and dispersion parameter γ,

$$g(\omega) = \frac{1}{\pi}\frac{\gamma}{(\omega - \omega_0)^2 + \gamma^2}. \tag{3.5}$$

3.2.2 Components of the Phase Response Curve

The shift induced on the collective phase in this system may be separated into two components: (1) The prompt phase shift induced on the system at $t = t'$ governed by the microscopic phase response curve, and (2) the slower acting phase shift mediated

by the coupling function as the ensemble returns to its asymptotic state [89] (see Fig. 3.1). Assume that just before the perturbation occurs the order parameter is given by Z_0 and the mean phase ψ_0. Barred quantities will refer to the system just after the perturbation.

Definition III.1 (pPRC Δ_0)**.** Let us define the *prompt phase response curve* as the phase shift of the mean phase just after the perturbation $t = t'$.

$$\Delta_0(\psi_0) = \bar{\psi} - \psi_0 = Arg\frac{\bar{Z}}{Z_0}$$

Definition III.2 (fPRC Δ_∞)**.** Let us define the final ($t \to \infty$) phase resetting value as the *final phase response curve* where

$$\Delta_\infty(\psi_0) = \lim_{t\to\infty}[\bar{\psi}(t) - \psi(t)] = \lim_{t\to\infty} Arg\frac{\bar{Z}(t)}{Z(t)}$$

In the long-time limit the dynamics of Eq. (3.3) for heterogeneous oscillators collapses to the so-called Ott-Antonsen manifold [113]. Within the Ott-Antonsen manifold the dynamics of Z are described by a two dimensional system for the phase coherence R and the mean phase ψ:

$$\dot{R} = -\gamma R + \frac{K_0\cos(\beta)}{2}R(1-R^2) \tag{3.6a}$$

$$\dot{\psi} = w_0 + \frac{K_0\sin(\beta)}{2}(1+R^2) \tag{3.6b}$$

These equations are solved analytically in [89] to give a prediction for the final phase shift as,

$$\Delta_\infty = Arg\left[\frac{\bar{Z}}{Z_0}\right] + \tan(\beta)\ln\left|\frac{\bar{Z}}{Z_0}\right| = \Delta_0 + \Delta_R. \tag{3.7}$$

Here we define Δ_R as the *relaxation phase shift* or the phase shift incurred during

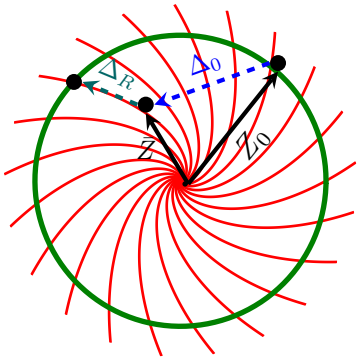

Figure 3.1: The order parameter just before the perturbation is at Z_0. Just after the perturbation it is shifted to $\bar{Z}$. Δ_0 tracks the shift in the mean phase that occurs in the movement from Z_0 to $\bar{Z}$ and Δ_R gives the relaxation phase shift of the collective oscillator. The isochrons here show the case where $\beta = -\frac{1}{2}$.

the relaxation of the system to equilibrium. The dynamics of the order parameter only collapse to two-dimensions (Eqs. 3.6) for continuous density functions which lie strictly within the Ott-Antonsen Manifold [113] [95]. However, as demonstrated in Levnajić and Pikovsky [89] numerically and further validated in this work, we expect Eqs. (3.7) to provide a good approximation for sufficiently small deviations off the manifold.

Using the Ott-Antonsen reduced system (Eqs. 3.6) we can analyze the isochrons of the collective oscillator for states lying within the OA manifold. When $\beta = 0$ the coupling function is odd and the isochrons of the collective oscillator are radial. For radial isochrons a change in the phase coherence will not affect the phase and $\Delta_R = 0$ meaning $\Delta_\infty = \Delta_0$. However, when $\beta \neq 0$ the collective oscillator (Eqs. 3.6) has spiral isochrons and a change in the phase coherence will induce an additional rotation (Fig .3.1).

From Eqs. (3.7) we can see the collective PRC (Δ_∞) is determined by the mapping $Z_0 \to \bar{Z}$ at the instant the perturbation is applied (Fig. 3.1). We will now show that the nature of this mapping depends on the Fourier decomposition of the microscopic PRC $Q(\phi)$.

3.3 Analytical Approximation of $\bar{Z}$

As $N \to \infty$ we may replace Eq. (3.1) by the continuity equation (Eq. 3.3) describing the time evolution of $f(\omega, \phi, t)$ the continuous density function. To ease the notation in this section we set the time of the perturbation $t' = 0$.

As $t \to \infty$ the continuous density function $f(\omega, \phi, t)$ will collapse to the Ott-Antonsen manifold [113]. Within the Ott-Antonsen manifold the higher moments of Z may be expressed as powers of Z such that $Z_n = (Z)^n$ and $Z_{-n} = (Z^*)^n$ where $*$ denotes the complex conjugate. This property will be exploited to obtain the map from $Z_0 \to \bar{Z}$ for a general Q in closed form.

For times sufficiently close to the moment of the perturbation ($t = t' = 0$) the $\epsilon Q(\phi)$ term will dominate the velocity of f and the continuity equation can be approximated as,

$$f_t + \frac{\partial}{\partial \phi}[\epsilon Q(\phi) f(\omega, \phi, t)\delta(t)] \approx 0. \tag{3.8}$$

Applying the method of characteristics (see Appendix B for more details) to Eq. 3.8 yields the characteristic equations,

$$\frac{d\phi}{dt} = \epsilon \delta(t) Q(\phi) \tag{3.9a}$$

$$\frac{dh}{dt} = -\epsilon \delta(t) Q'(\phi) h \tag{3.9b}$$

where $h(t) = f(\omega, \phi, t)$. In order to obtain an analytical solution for Eqs. (3.9) we assume ϵ is a small parameter and conduct a perturbation expansion. The expansion will be valid for small changes in the mean phase ψ. To leading order in ϵ we find,

$$\phi(t) = \phi_0 + \epsilon Q(\phi_0) \tag{3.10a}$$

$$h(t) = h_0 e^{-\epsilon Q'(\phi_0)}, \tag{3.10b}$$

for $t > 0$ where ϕ_0, h_0 indicate the quantities just prior to the perturbation.

Since $Q(\phi) = Q(\phi_0) + O(\epsilon)$ we approximate $\phi_0 \approx \phi - \epsilon Q(\phi)$. Thus, we approximate $\bar{f}(\omega, \phi)$ the distribution after the perturbation as,

$$\bar{f}(\omega, \phi) = f(\omega, \phi - \epsilon Q(\phi)) e^{-\epsilon Q'(\phi - \epsilon Q(\phi))} \tag{3.11}$$

to leading order in ϵ. We integrate out the ω dependence and define $\rho(\phi)$ which gives the fraction of oscillators at phase ϕ,

$$\rho(\phi) = \int_{-\infty}^{\infty} f(\omega, \phi) d\omega. \tag{3.12}$$

Therefore, we can write

$$\bar{\rho}(\phi) = \rho(\phi - \epsilon Q(\phi)) e^{-\epsilon Q'(\phi - \epsilon Q(\phi))} \tag{3.13}$$

Eq. 3.13 gives an expression, valid for small ϵ, for the continuous phase distribution just after the perturbation $\bar{\rho}(\phi)$ in terms of the phase distribution prior to the perturbation $\rho(\phi)$. We now convert Eq. 3.13 into an expression for the order parameter and derive a form for the desired mapping $Z_0 \to \bar{Z}$. We expand Eq. (3.13) to leading order in ϵ, multiply by $e^{i\phi}$ and integrate to get an expression in terms of the order parameter Z.

$$\bar{Z} = Z_0 - \epsilon \int_{-\pi}^{\pi} \rho(\phi) Q'(\phi) e^{i\phi} d\phi - \epsilon \int_{-\pi}^{\pi} \rho_\phi Q(\phi) e^{i\phi} d\phi \tag{3.14}$$

Integrating the second term by parts and simplifying gives

$$\bar{Z} = Z_0 + i\epsilon \int_{-\pi}^{\pi} \rho(\phi) Q(\phi) e^{i\phi} d\phi. \tag{3.15}$$

In order to express the integral in Eq. 3.15 in terms of powers of Z_0 we replace $Q(\phi)$

with its Fourier Series representation,

$$Q(\phi) = \frac{A_0}{2} + \sum_{n=1}^{\infty} A_n e^{in\phi} + A_n^* e^{-in\phi}. \tag{3.16}$$

This gives the following expression,

$$\bar{Z} = Z_0 + i\epsilon \left(\frac{A_0}{2} Z_0 + \sum_{n=1}^{\infty} \int_{-\pi}^{\pi} A_n \rho e^{i(n+1)\phi} + A_n^* \rho e^{i(1-n)\phi} \right). \tag{3.17}$$

Since $\rho(\phi)$ describes a system on the Ott-Antonsen manifold we have the special property,

$$\int_{-\pi}^{\pi} \rho(\phi) e^{in\phi} d\phi = (Z_0)^n \qquad\qquad \int_{-\pi}^{\pi} \rho(\phi) e^{-in\phi} d\phi = (Z_0^*)^n. \tag{3.18}$$

Applying this moment closure allows us to close Eq. 3.17,

$$\bar{Z} = Z_0 + i\epsilon \left(\frac{A_0}{2} Z_0 + \sum_{n=1}^{\infty} A_n Z_0^{n+1} + A_n^* (Z_0^*)^{n-1} \right)$$

This can be rearranged to give,

$$\bar{Z} = Z_0 \left(1 + i\epsilon \hat{Q}(\psi) \right) \tag{3.19a}$$

$$\hat{Q}(\psi) = \frac{A_0}{2} + \sum_{n=1}^{\infty} R^{n-1} (R A_n e^{in\psi} + \frac{A_n^*}{R} e^{-in\psi}). \tag{3.19b}$$

Eqs. (3.19) gives an expression for $\bar{Z}$ in terms of Z_0 valid for small values of ϵ in terms of the Fourier series for the microscopic PRC.

Notice that $\hat{Q}(\psi)$ is closely related to the microscopic phase response curve $Q(\phi)$. For values of the phase coherence ≈ 1 the spread of the phase distribution is small and $\hat{Q}(\psi) \approx Q(\psi)$. However, as the phase coherence decreases, $\hat{Q}(\psi)$ diverges from the microscopic phase response curve.

In addition, we note the Ott-Antonsen reduction has only been applied as a moment closure in this derivation. In particular, the integral equation Eq. 3.15 may be used for cases for which the Ott-Antonsen reduction cannot be applied and be adapted to moment-closure schemes which close the moments at a higher order. In Chapter IV we will adapt this procedure for the study of mammalian circadian rhythms using the m^2 ansatz in place of the Ott-Antosen ansatz.

3.3.1 Prompt Phase Response Curve Δ_0

With an analytical expression for the order parameter after the perturbation is applied (Eqs. 3.19) we may derive an expression for the prompt phase resetting curve Δ_0.

$$\begin{aligned}\Delta_0 = Arg\left[\frac{\bar{Z}}{Z_0}\right] &= Arg\left[\frac{Z_0\left(1+i\epsilon\hat{Q}(\psi)\right)}{Z_0}\right] \\ &= \arctan\left(\frac{\epsilon Re[\hat{Q}(\psi)]}{1-\epsilon Im[\hat{Q}(\psi)]}\right) \\ &\approx \epsilon Re[\hat{Q}(\psi)] + O(\epsilon^2)\end{aligned}$$

Taking the real part of $\hat{Q}(\psi)$ yields,

$$\Delta_0(\epsilon, R, \psi) = \frac{\epsilon}{2}\left\{A_0 + \sum_{n=1}^{\infty} R^{n-1}\left(R+\frac{1}{R}\right)\left[a_n \sin(n\psi) + b_n \cos(n\psi)\right]\right\} \tag{3.20}$$

which is an asymptotic expansion valid as $\epsilon \to 0$ for the prompt phase resetting curve as a function of the Fourier Series for the microscopic phase response curve and the phase coherence (R) of the system. Lower phase coherence values affect the Fourier modes of the microscopic phase response curves differently.

Specifically, Eq. 3.20 predicts a scaling for the amplitude of the collective PRC. In particular, for microscopic PRCs which are dominated by their first harmonic the

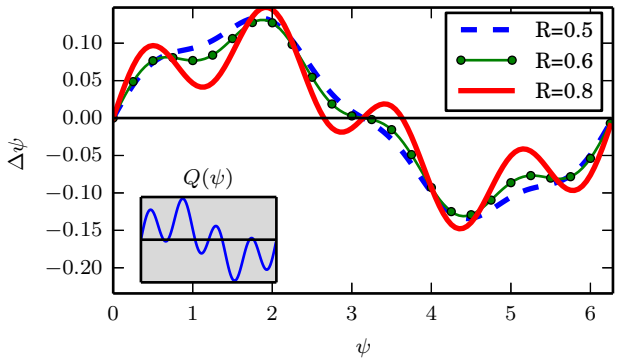

Figure 3.2: A representative plot of the prompt phase response curve Δ_0 for various values of R and $Q(\psi) = \sin(\psi) + \sin(4\psi)$ with $\epsilon = 0.1$. The first harmonic is amplified and higher harmonics are dissipated in the collective PRC.

amplitude of the collective PRC should scale like $R + \frac{1}{R}$ and for a microscopic PRC whose principal Fourier coefficient is of order N the amplitude of the collective PRC should scale like $R^N + R^{N-2}$. For microscopic PRCs composed of several modes we expect the first harmonic to be amplified and higher harmonics to be damped in the collective PRC resulting in a change in shape of the PRC (Fig. 3.2).

3.3.2 Amplitude Response Curve

The formalism developed here allows us to predict not only the phase shift of the collective phase but also how perturbations of individual oscillators affect the phase coherence of the population. Since we are operating within the Ott-Antonsen framework we expect that after a perturbation the system will return to its equilibrium R value for long times. However, it is interesting to consider how the phase coherence is transiently altered by perturbations. To study this we introduce the amplitude response curve $\Lambda(\psi, R, \epsilon)$ where Λ is defined as the ratio of the phase coherence after the perturbation to the phase coherence prior to the perturbation.

$$\begin{aligned}\Lambda_0(\psi, R, \epsilon) &= \left|\frac{\bar{Z}}{Z_0}\right| \approx \left|\frac{Z_0 + \epsilon i Z_0 \hat{Q}(\psi)}{Z_0}\right| \\ &= \sqrt{1 - 2\epsilon Im[\hat{Q}] + \epsilon^2(Re[\hat{Q}]^2 + Im[\hat{Q}]^2)} \\ &= 1 - \epsilon Im[\hat{Q}] + O(\epsilon^2)\end{aligned}$$

Therefore using that $Im[z] = (z - z^*)/2i$ we have that

$$\begin{aligned}Im[\hat{Q}] &= \sum_{n=1}^{\infty} R^{n-1}(\frac{1}{R} - R)\,\mathrm{Im}[A_n^* e^{-in\psi}] \\ Im[\hat{Q}] &= \frac{1}{2}\sum_{n=1}^{\infty} R^{n-1}(\frac{1}{R} - R)(a_n \cos(n\psi) - b_n \sin(n\psi))\end{aligned}$$

Where a_n is the nth sine coefficient and b_n is the nth cosine coefficient in the Fourier Series of $Q(\psi)$. This gives the following expression for Λ_0:

$$\Lambda_0(\psi, R, \epsilon) \approx 1 + \frac{\epsilon}{2}\sum_{n=1}^{\infty} R^{n-1}\left(\frac{1}{R} - R\right)[b_n \sin(n\psi) - a_n \cos(n\psi)] \tag{3.21}$$

Notice that

$$b_n \sin(n\psi) - a_n \cos(n\psi) \propto -\frac{dQ}{d\psi},$$

so we expect the amplitude shifts to be greatest around the zeros of the microscopic phase response curve, with increases in R around stable points and decreases around unstable points (Fig. 3.3).

In addition, we note this derivation contains two expected limits: as $\epsilon \to 0$ or $R \to 1$ we expect the amplitude changes to be unchanged by the perturbation.

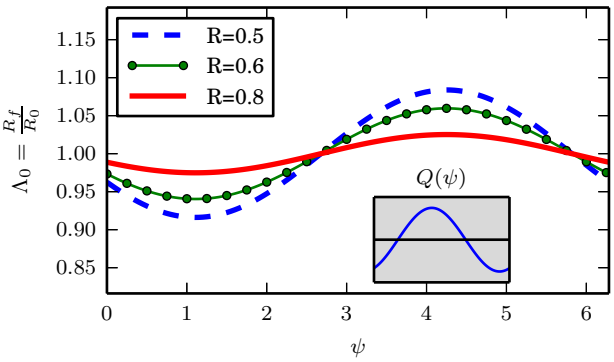

Figure 3.3: A representative plot of the amplitude response curve Λ for various values of the phase coherence with $Q(\psi) = \frac{1}{2}sin(\psi) - cos(\psi)$ and $\epsilon = 0.1$. Perturbations around stable fixed points of $Q(\psi)$ give transient increases in the phase coherence and perturbations about unstable fixed points of $Q(\psi)$ give decreases in the phase coherence.

3.3.3 Relaxation Phase Response Curve Δ_R

We now consider the case where the system (Eq. 3.1) evolves with a non-odd coupling function $\beta \neq 0$. In this case we expect the relaxation phase shift (Δ_R) to be non-zero. If the deviation off the Ott-Antonsen manifold is small enough we expect that Eq. 3.7 will provide a good estimate for Δ_R.

$$\Delta_R = \tan(\beta) \ln\left(\left|\frac{\bar{Z}}{Z}\right|\right) = \tan(\beta) \ln[\Lambda_0(R, \psi, \epsilon)]$$

Therefore, the relaxation phase shift depends on the logarithm of the amplitude response curve. Expanding this system to leading order in ϵ we get:

$$\Delta_R = \frac{\epsilon}{2} \tan(\beta) \sum_{n=1}^{\infty} R^{n-1} \left(\frac{1}{R} - R\right) [b_n \sin(n\psi) - a_n \cos(n\psi)] \tag{3.22}$$

where a_n is the n^{th} sine coefficient and b_n is the n^{th} cosine coefficient in the Fourier Series for $Q(\psi)$. Once again as the phase coherence goes to one the relaxation phase shift goes to zero. Also, we expect the effect of the relaxation phase shift to be

strongest around the zeros of the microscopic phase response curve $Q(\psi)$ because the amplitude response curve is maximal at those points (Fig. 3.3).

Therefore, for systems with $\beta \neq 0$ we expect the collective PRC to have shifted zeros compared to the microscopic phase response curve. Moreover, this shift will become more exaggerated when the microscopic phase response curve is dominated by low harmonics and the ensemble has a small phase coherence.

3.3.4 Collective Phase Response Curve Δ_∞

Having computed the prompt phase response curve Δ_0 and the relaxation curve Δ_R we can now write down an expression for the collective phase response curve Δ_∞ valid for small ϵ,

$$\Delta_\infty = \Delta_0 + \Delta_R \tag{3.23a}$$

$$\Delta_0 = \frac{\epsilon}{2}\left\{ A_0 + \sum_{n=1}^{\infty} R^{n-1}\left(R + \frac{1}{R}\right)\left[a_n \sin(n\psi) + b_n \cos(n\psi)\right]\right\} \tag{3.23b}$$

$$\Delta_R = \frac{\epsilon}{2}\tan(\beta)\sum_{n=1}^{\infty} R^{n-1}\left(\frac{1}{R} - R\right)\left[b_n \sin(n\psi) - a_n \cos(n\psi)\right]. \tag{3.23c}$$

Therefore we have expressed the collective phase response function in terms of the Fourier coefficients of the microscopic phase response function and the phase coherence of the equilibrium state.

We may now find an approximation for the shift in zeros for the collective phase response curve. If $\Delta_\infty(\psi_0) = 0$ then we have $\Delta_0(\psi_0) = -\Delta_R(\psi_0)$. Let $Q(\psi)$ be a microscopic PRC which is dominated by its nth harmonic, then applying Eqs. 3.23 we get that,

$$\tan(n\psi_0) = \tan(\beta)\left(\frac{2}{1+R^2} - 1\right) \tag{3.24}$$

Let ψ^* be the zero of the microscopic PRC $Q(\psi^*) = \Delta_0(\psi^*) = 0$ and let $\Delta\psi_z = \psi_0 - \psi^*$ be the shift in the zero for the collective PRC. We expand Eq. 3.24 about ψ^* to get an expression for the shift in the zero $\Delta\psi_z$,

$$\Delta\psi_z = \frac{1}{n}\left(\frac{2}{R^2+1} - 1\right)\tan(\beta). \tag{3.25}$$

Thus, the shift in the zeros of the collective phase response curve relative to the microscopic PRC will increase like $\frac{1}{R^2+1}$ for smaller values of the phase coherence and will be attenuated like $1/n$ when the microscopic phase response curve is dominated by higher harmonics.

In summary, Eqs. 3.23 make the following predictions concerning the difference between the microscopic phase response curve Q and the collective PRC for sinusoidally coupled heterogeneous phase oscillators:

1. The amplitude of the nth harmonic in the collective PRC should scale like $R^{n-1}(R + \frac{1}{R})$ relative to the microscopic PRC.

2. For non-odd coupling functions ($\beta \neq 0$) the zeros of the collective PRC should be shifted in a manner that scales with $\frac{2}{R^2+1} - 1$ relative to the microscopic PRC.

We now test these predictions numerically for coupled phase oscillators and for a model of electrically coupled neurons.

3.4 Numerical Results

In this section we present numerical results in order to test the theoretical findings from the previous section. For each simulation we set $N = 10^4$ oscillators and numerically integrate (Eq.3.1) to find the stationary phase distribution. The natural frequencies of the oscillators were drawn from a Cauchy distribution (Eq. 3.5) with

dispersion parameter $\gamma = 0.5$ and mean $w_0 = 0.0$. In order to generate phase distributions with differing phase coherence (R) values the strength of the coupling constant K_0 in Eq. 3.1 was varied. Ott-Antonsen theory predicts and numerics validate that the equilibrium phase coherence and coupling constant are related by, $K_0 = \frac{2\gamma}{(1-R^2)\cos(\beta)}$. A stationary phase distribution was generated by numerically integrating Eq. 3.1 for long-times.

A stimulus was applied to the stationary phase distribution at a sampling of mean phase values $\psi \in [0, 2\pi)$ and the order parameter was recorded just after the application of the stimulus. The system was numerically integrated for a long-time until a steady state phase shift in the mean phase was recovered relative to the unperturbed system. These numerical collective PRCs were compared against the theoretical predictions from Sec. 3.3.

As a first case, we consider a simple microscopic PRC $Q(\psi) = \sin(\psi)$ (Fig. 3.4). This provides validation that the first harmonic is amplified like $R+\frac{1}{R}$ in the collective PRC and the zeros of the microscopic PRC are shifted proportional to $\tan(\beta)(\frac{1}{R} - R)$ in the collective PRC (Fig. 3.4).

In Fig. 3.5 we consider more general microscopic PRCs and once again see good agreement between the theoretical prediction (Eq. 3.23) and numerical simulations. As can be seen in Fig. 3.5 the collective PRC can deviate significantly from the microscopic PRC and these differences can largely be understood as an amplification of the first harmonic and dissipation of higher harmonics.

When the microscopic PRC is composed of several harmonics this amplification/dissipation can be manifest in a significant change in shape from the microscopic to the collective PRC (Fig. 3.5(d)). For example, in Fig. 3.5(d) the collective PRC has a phase delay region which is not present in the microscopic PRC. Moreover, the collective PRC in Fig. 3.5(d) has a stable entrainment point where the microscopic PRC has only a neutrally stable region ($\psi > \pi$).

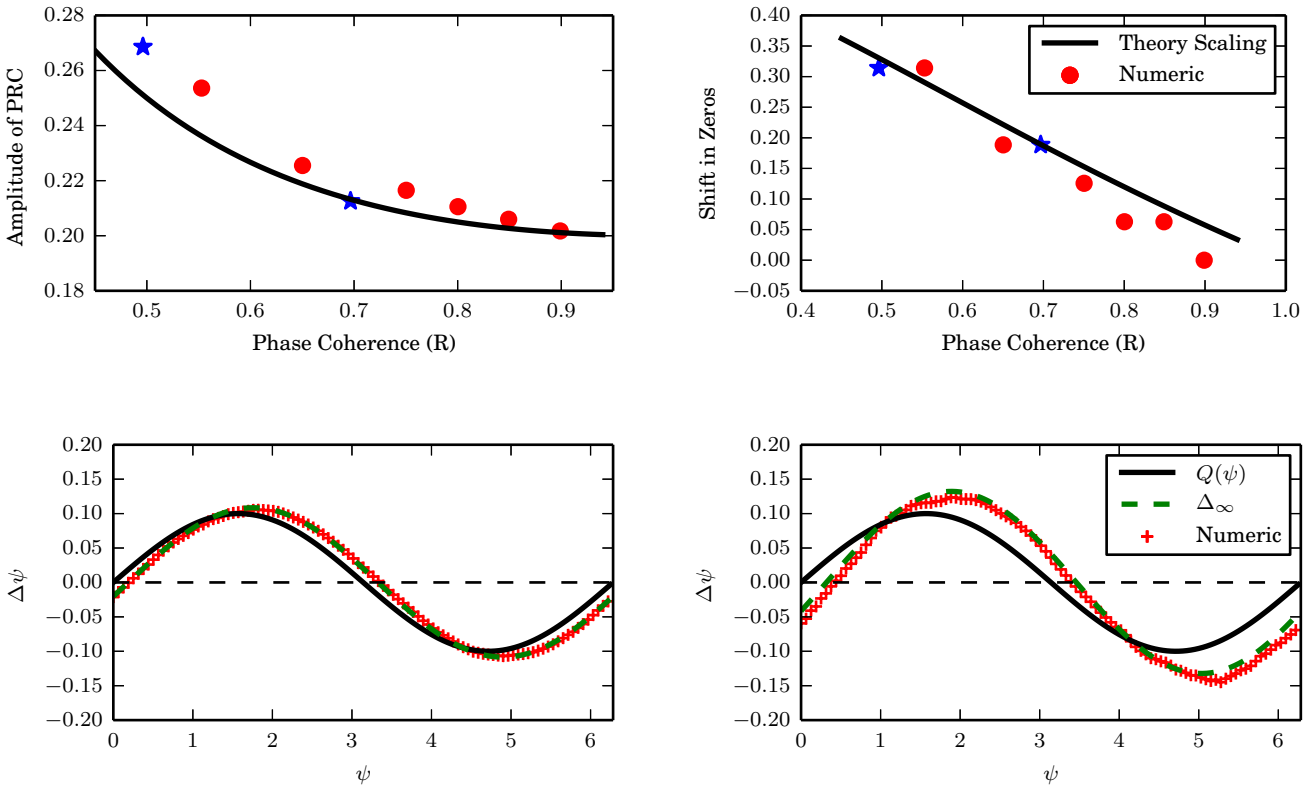

Figure 3.4: Change in the amplitude and entrainment points for a sinusoidal microscopic PRC. Here we set $Q(\psi) = \sin(\psi)$, $\epsilon = 0.1$ and $\beta = 0.5$. The coupling strength K_0 was varied to produce phase distributions with differing phase coherence (R) values in the synchronized state. Blue stars in Fig. (a,b) indicate the values of R which are plotted in (c,d). (a) The amplitude of the collective phase response curve scales like $R + \frac{1}{R}$ with the phase coherence. (b) The shift in the zero at $\psi = \pi$ scales like $\tan(\beta)\left(\frac{2}{R^2+1} - 1\right)$. (c) Microscopic, predicted collective PRC and numerical collective PRC for $R = 0.7$ (d) Microscopic, predicted collective PRC and numerical collective PRC when R=0.5.

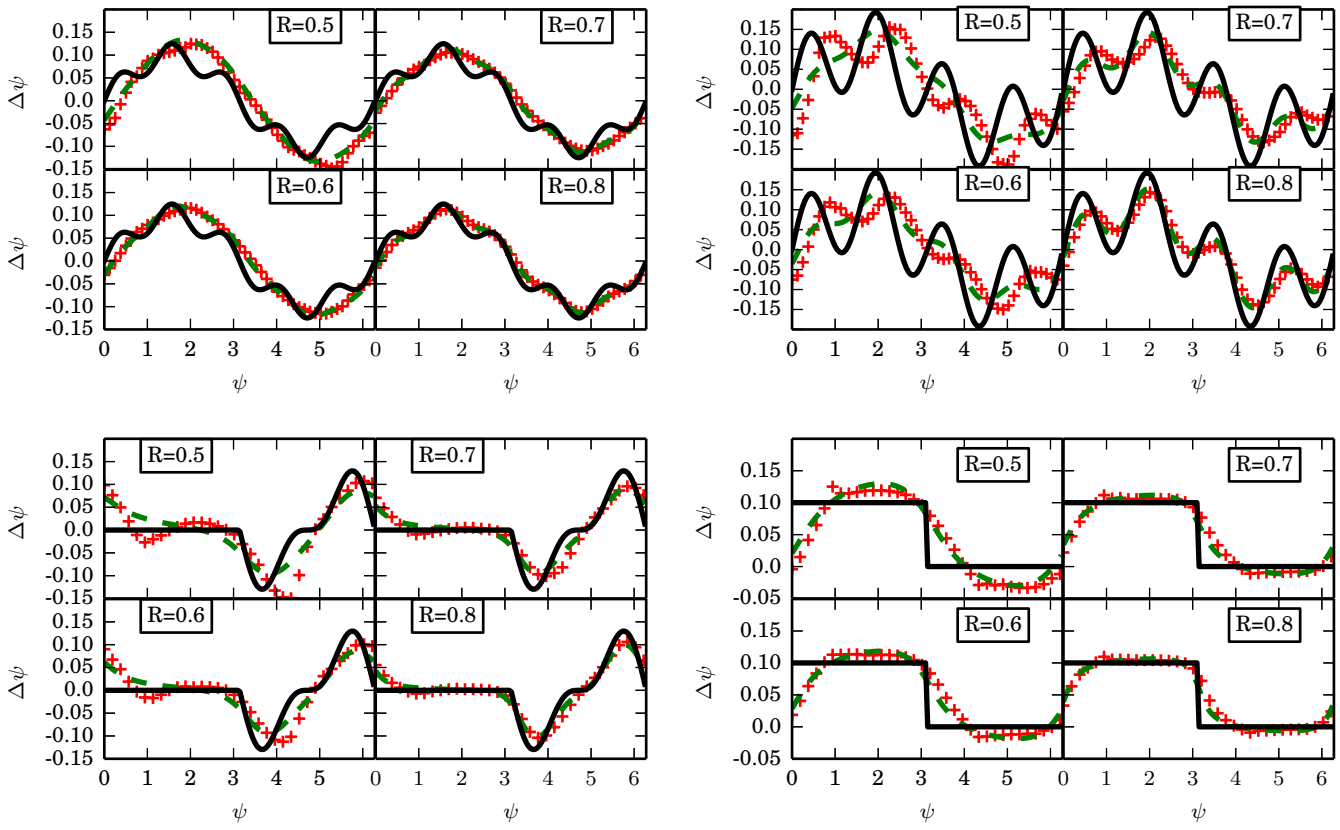

Figure 3.5: Comparing theoretical predictions against numerical results for the collective PRC for various microscopic PRC with $\epsilon = 0.1$ and $\beta = 0.5$. The coupling strength K_0 was varied to produce phase distributions with differing phase coherence (R) values in the synchronized state. Microscopic PRC (solid black), Δ_∞ (dashed green), numerical simulation (red '+'). Let $H(\psi)$ be the heaviside step function. (a) $Q(\psi) = \sin(\psi) + \frac{1}{4}\sin(5\psi)$ (b) $Q(\phi) = \sin(\psi) + \sin(4\psi)$, (c) $Q(\psi) = H(\psi - \pi)(-\sin(2\psi) - \sin(2\psi)\cos(2\psi))$ (d) $Q(\psi) = H(-\psi - \pi)$.

3.5 Applications

3.5.1 Application to a Neuronal Model

In order to investigate the broader application of this theory, we considered a system of coupled neurons modeled by the Morris-Lecar Model. The Morris-Lecar model is a two-dimensional conductance-based neuronal firing model which is commonly used as a general neural model [104]. For model details and parameter values see Appendix E.

We consider an all-to-all connected system of Morris-Lecar neurons with electrical coupling between the neurons. Specifically, the coupling term in the current balance equation for neuron i is $\sum_j g_{syn}(V_j - V_i)$ where j sums over all other neurons in the network. The population of neurons is set to fire with heterogeneous frequencies distributed in a Cauchy manner. The Morris-Lecar model is capable of producing both Type I and Type II microscopic phase response curves for different parameter values [37]. This classification of neuronal PRCs distinguishes between two physiologically observed neuronal firing properties and is linked to the neural membrane properties and the bifurcation which births the oscillations. In a Type I neuronal system the PRC is characterized by having a large region of phase advances and a comparatively small region of phase delays in response to an applied current [37]. A Type II PRC is characterized by having regions of both phase advances and delays. In this context the distinction allows us to test the collective PRC theory for two qualitatively different and physiologically relevant microscopic phase response curves.

In order to evaluate the utility of the theoretical predictions of this work we computed the individual neuron phase response curves, the Ott-Antonsen predicted collective phase response function and the numerical collective phase response function in both the Type I and Type II parameter regimes. The numerical curves were produced using a short weak applied current pulse ($I_{applied} = 1.0\frac{uA}{cm^2}$, $\Delta t = 1$ms) to

each individual neuron and then measuring the phase shift in the mean phase for an ensemble of $N = 10^3$ neurons. Ensembles of neurons with differing phase coherence (R) values in the equilibrium state were generated by varying the strength of the coupling through the g_{syn} parameter.

We first consider the Type I parameter regime for the Morris-Lecar model. We numerically determined the collective phase response curve for various values of the phase coherence. For $R \approx 1$ all oscillators are phase locked together and the microscopic, asymptotic Ott-Antonsen collective and numerical collective PRC agree. However, as R was decreased we observed several changes in the shape of the collective phase response curve. First, higher harmonic Fourier terms in the microscopic PRC damped out quickly. Secondly, the amplitude of the first harmonic grows as R decreases and finally we saw a slight phase shift in the zeros of the curve. The asymptotic Ott-Antonsen procedure correctly predicted each of these qualitative changes (Fig. 3.6).

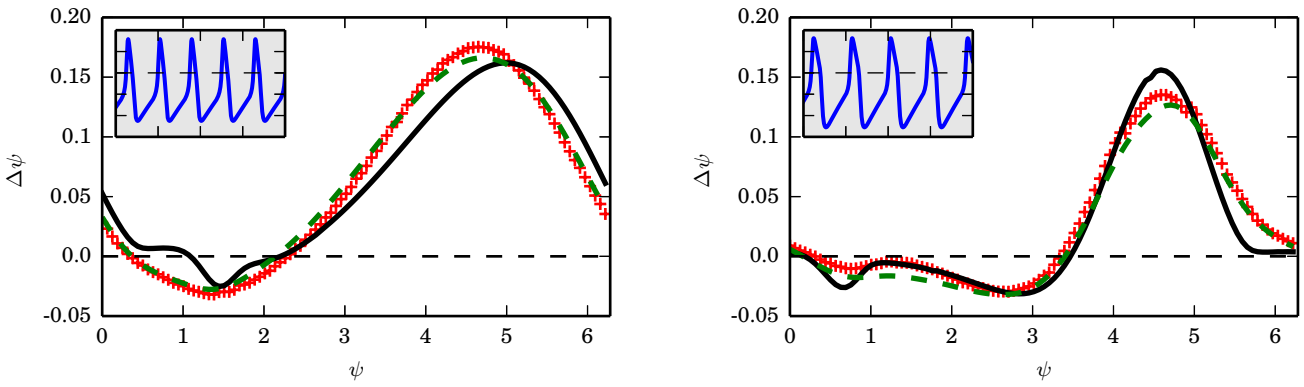

Figure 3.6: Comparing theoretical predictions against numerical results for the collective PRC of Morris-Lecar neurons. Inset plots show individual neurons action potentials (mV) for 400 ms in the synchronized state for the two parameter regimes. Microscopic PRC (solid black), Δ_∞ (dashed green), numerical simulation (red '+') (a) Collective PRC for Type I Morris-Lecar Neurons with $R = 0.67$ and mean applied current of $50.0\frac{\mu A}{cm^2}$. (b) Type II Morris-Lecar system with $R = 0.70$ and mean applied current of $95\frac{\mu A}{cm^2}$.

These conclusions carried through to the case of Type II neurons as well. However,

for the Type II regime we did not see as prominent a phase shift between the collective and microscopic phase response curves. This can be explained by the β term in the Ott-Antonsen asymptotic method. The β term for both the Type I and II parameter regimes was computed numerically by truncating the Fourier series for the coupling function determined in the course of the phase reduction of the coupled Morris-Lecar system (see Appendix E for more details). For electrically coupled neurons with Type II microscopic PRCs $\beta = 0.25$ while for electrically coupled neurons with Type I microscopic PRCs $\beta = -0.65$. This implies that the Type II system isochrons are closer to radial so we see a smaller resetting shift (Δ_R) due to the perturbation.

In both of these cases we see that the Ott-Antonsen derived collective phase response curve gives a good approximation to the numerical case and provides an accurate approximation for the shape, zeros and amplitude of the collective phase response curve. We note the asymptotic procedure matches numerical simulations well despite a violation of the assumptions of the Ott-Antonsen reduction. In particular, the coupling functions for both the Type I and Type II parameter regimes have higher harmonic terms which violates a principal assumption of the Ott-Antonsen approach [95]. Finally, this theory makes the experimentally testable prediction that a coupled system of Type II neurons will be able to entrain to a smaller frequency range than the individual neurons with the opposite being true for coupled Type I neurons.

3.6 Conclusions

We have constructed an asymptotically valid analytic formula for the collective phase response function in terms of the microscopic phase response curve for globally coupled Sakaguchi-Kuramoto phase oscillators interacting via an non-odd coupling function. Our analytic results extend the framework developed in Levnajić and Pikovsky [89] to consider a general microscopic PRC and determines a characteristic scaling for changes in the amplitude and zeros of the collective PRC relative to the

microscopic PRC. These results were validated through comparison with numerical simulations for a variety of microscopic PRCs. By studying a system of coupled neurons we demonstrated the broader applicability of the theory to biological systems.

In particular, the theory predicts the amplitude and zeros of the collective PRC. For weakly forced systems a larger amplitude PRC indicates a broader range of frequencies which can entrain the system and the zeros predict the phase offset between the entraining force and the mean phase of the population of oscillators. Therefore, a better understanding of how these properties may be altered by coupling between large ensembles of oscillators has direct application to many biological systems. For instance, in experimental studies of the mammalian circadian rhythm, it was found that weaker coupling between the neurons or a greater variance in the phase distribution of the oscillators decreased the entrainment time to light input and increased the entrainment range [5, 3]. This suggests the collective PRC has a larger amplitude than the microscopic PRC in the circadian system as predicted by our analysis.

Moreover, the collective PRC is shown to have a change in shape when the microscopic PRC is composed of several harmonics. The first harmonic is amplified and higher harmonics are dissipated as the phase coherence of the population is decreased. This can result in the introduction of advance/delay regions in the collective PRC which are not observed in the microscopic PRC and an overall smoothing of the curve.

The Ott-Antonsen dimension reduction is a key component allowing for an analytical investigation of the collective PRC presented in this chapter. The Ott-Antonsen reduction is strictly valid for sinusoidally coupled heterogenous Sakaguchi-Kuramoto phase oscillators. However, as demonstrated numerically, for a Morris-Lecar neuronal system here and for Stuart-Landau oscillators in [89], it provides a useful approximation even for systems which have not been shown to rigorously collapse to the Ott-Antonsen manifold. Moreover, additional dimension-reduction techniques have been developed which may be useful in studying the collective phase response curve in

the future [22, 120, 152, 54, 136]. In Chapter IV I develop a theory of collective phase resetting for mammalian circadian rhythms using the m^2 ansatz as the dimension reduction tool.

The prompt phase shift, Δ_0, can be estimated when the Ott-Antonsen moment closure cannot be applied using the integral equation Eq. 3.15 either numerically or analytically by using an appropriate higher order moment closure. However, in the absence of the Ott-Antonsen reduction the computation of the relaxation phase shift Δ_R presents a challenge. In this case we cannot assume the collective oscillator has simple spiral isochrons as exploited in [89] to derive Eq. 3.7. Therefore, the computation becomes much more difficult. In Chapter IV, I develop a perturbation approach for the calculation of the relaxation phase shift which may be used to approximate these phase shifts in a general context.

CHAPTER IV

Seasonality and Light Phase-Resetting in Mammalian Circadian Rhythms

4.1 Introduction

Daily or circadian cycles in behavior and metabolism can be observed for virtually all forms of life. The utility of circadian rhythms relies on the proper timing of these cycles relative to external environmental oscillations. Thus, a defining property of circadian rhythms is their ability to be entrained to external time cues or zeitgebers. The principal zeitgeber for the mammalian circadian clock is light [123]. Therefore, a crucial component to understanding mammalian circadian rhythms is an improved understanding of the impact of light on the circadian cycle. A first step in this endeavor is understanding the response of the circadian circuit to a brief light pulse.

The theory of phase response curves (PRC) provides a natural language for studying the effects of external stimuli on endogenous rhythms with a rich history of application to circadian biology [72, 156]. Phase response curves characterize the phase shift induced by the application of the stimulus at different phases of the oscillation. For instance, the amplitude of the PRC gives the entrainment range of the system to a weak resetting signal and the zeros of the PRC specify the entrainment angle [118].

Phase response curve theory figured prominently in early investigations of circa-

dian rhythms, where organisms were exposed to a sensory stimulus at a sampling of points across the daily cycle and phase shifts were measured relative to to some behavioral or physiological marker [28, 156]. However, the discovery of the location of the master circadian clock in a small region of the hypothalamus known as the suprachaismatic nucleus (SCN) provided a neurological basis for circadian rhythms in mammals [103, 139]. The SCN was found to contain thousands of coupled clock neurons which each contain a biochemical oscillator with a period of approximately twenty-four hours [92]. Daily activity cycles are driven by this large ensemble of coupled oscillators acting collectively to produce a reliable circadian oscillation.

Thus, a light stimulus applied to the mammalian circadian rhythm does not act by shifting a single limit cycle oscillator, but rather acts by shifting the oscillations of individual clock neurons which in turn induce a shift in the collective rhythms produced by the ensemble. The recognition of this distinction helped motivate the development of the theory of collective phase response curves which describe the collective phase shift of an entire population of coupled oscillators subjected to a stimulus [73, 77, 81, 89]. Collective phase resetting is especially important for the mammalian circadian response to light, because only a fraction of the clock cells are phase shifted in response to the stimulus [98]. This may induce non-trivial transient dynamics on the system following a light perturbation and forms a major focus of this work [107].

In general, the phase-shifting behavior of a coupled ensemble of oscillators differs from the behavior of a single autonomous oscillator. In this work we study the transformation between the response of a single circadian cell to a light-pulse (microscopic PRC) and the collective phase response described by the shift in the mean-phase of the population of oscillators. A growing literature on collective phase resetting has revealed coupling, oscillator heterogeneity and network structure can all lead to significant differences between the microscopic and collective PRCs in networks of

coupled oscillators [89, 81, 77, 73]. Within the circadian literature, examinations of collective phase resetting have led to the formation of a rule of thumb that increasing phase dispersion in the oscillator population leads to a monotonic increase in the amplitude of the collective phase response [125, 3] and thus the entrainment range of the collective oscillator [156].

In addition to the role of light input in ensuring the circadian clock is synchronized to the outside environment, the SCN is also responsible for storing seasonal day-length information [23, 97, 143]. The ability of seasonal day-lengths to alter the core circadian clock was established in early circadian studies, where it was noticed that entrainment of mammals to long/short day-lengths caused lasting changes in the endogenous circadian period when organisms were transfered to a dark environment [122]. These effects are known as seasonal after-effects and have been described for many mammal species [28, 122].

Recently, significant progress has been made in characterizing the physiological changes in the SCN underlying seasonal day-lengths changes [147, 106, 105, 40, 18]. The physiological changes in the SCN which encode the seasons have been shown to affect the phase response to brief light pulses. When organisms are entrained to long (summer) days the phase shift caused by brief light pulse is seen to decrease [126, 147]. This seemingly contradicts the rule of thumb for collective phase resetting, because experimental evidence has also shown the phase dispersion in the SCN increases in longer day-lengths [147]. A primary goal of this work is to provide a unified theory of collective phase resetting to light in mammals, consistent with seasonal changes in SCN physiology.

In order to study phase resetting to light we make use of the m^2 ansatz (Chapter. II) to derive a three-dimensional model for the core circadian clock. Significantly, the m^2 ansatz is supported by experimental evidence and the resulting model gives variables and parameters which may be interpreted physiologically in the SCN [93].

Our work utilizes the framework for studying collective phase resetting developed in Levnajic and Pikovsky [89], and we apply this theory specifically to light induced phase resetting in mammals. We extend the results of Chapter III to consider oscillator networks where only a fraction of the population receives the phase-shifting stimulus. Additionally, we develop a perturbation technique which can be applied generally to characterize the effects of coupling on collective phase resetting.

The principal biological impacts of our work are three-fold. First, we provide a general theory for the effect of the collective amplitude on the phase-shifting capacity of the circadian clock. Our analysis reveals that the rule of thumb that lower amplitude rhythms give larger phase shifts in response to a stimulus is incomplete and more detailed analysis is required for many real-world phase response curves. Secondly, our analysis reveals that the reduction in light-shifting capacity observed for organisms entrained to long day-lengths may be explained by an adjustment of the coupling strengths with the seasonal day-length. Finally, we find this adjustment of coupling strengths is consistent with current theories for seasonal day-length encoding and is required to explain seasonal after-effects to light entrainment in mammals.

This chapter is organized as follows: In Sec. 4.2 we specify the circadian model, define the components of the collective PRC and derive the collective phase response for a single population model. In Sec. 4.3 we derive the collective phase response curve for the two population circadian model, In Sec. 4.4 we study the effect of seasonal day-length on light phase resetting in mammals. The results and conclusions are discussed in Sec. 4.5.

4.2 Formulation of the Model

4.2.1 Circadian Model

The suprachaismatic nucleus (SCN) is a collection of about $20,000$ neurons which form the core circadian pacemaker in mammals. Individual neurons in the SCN contain a biochemical feedback loop which cycles with a period of approximately 24 hours. While the SCN produces a variety of spatiotemporal patterns it can be functionally and physiologically broken into the ventral (core) and dorsal (shell) populations [45].

In mammals light input comes in through the eyes and is channeled to the SCN along the retinohypothamic tract (RHT) [98]. It is remarkable that the core circadian clock receives light information through a direct pathway from the eyes, which underscores the importance of light in entraining mammalian circadian rhythms. However, only a fraction of the clock cells in the SCN receive light input directly with the majority of cells receiving input in the ventral region [98]. Therefore, for the purposes of our model we split the SCN into ventral and dorsal phase clusters and allow light input into only the ventral population (Fig. 4.1).

Coupling between clock neurons in the SCN is mediated by a large suite of neurotransmitters [87]. In this chapter we focus on the functional coupling between the regions, although it may assist the reader to give an interpretation of the coupling in reference to two predominant neurotransmitters in mammalian circadian rhythms: vasoactive intestinal polypeptide (VIP) and γ-aminobutyric acid (GABA) whose properties have been characterized experimentally. Perhaps, the best understood coupling agent in the SCN is VIP which is released by the ventral population and is received by all or nearly all the oscillators [6]. VIP is known to be a synchronizing force in the SCN (phase attractive) [96]. Recent experimental results [105, 42] and detailed mathematical modeling [32] suggest that GABA mediated coupling is more subtle. GABA is released and received by all or nearly all clock neurons in

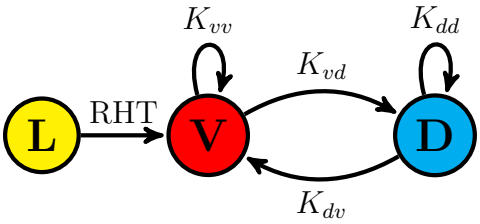

Figure 4.1: Subpopulations and coupling in the SCN. Light input comes into the sensor cells in the ventral SCN through the retino-hypothalamic tract (RHT). The majority of the dorsal cells do not receive direct input from the RHT but are bidirectionally coupled to the ventral sensor cells. Coupling terms are labeled as in Eqs. 4.1.

the SCN and has been identified as both a synchronizing [91] and desynchronizing [48, 10] agent among clock cells, although recent evidence suggests these properties vary spatially in the SCN [105, 32]. Evidence suggests that both VIP and GABA are involved in the communication of phase shifts between the ventral and dorsal SCN as well as the storage of seasonal day-length information in the SCN [99, 105, 32, 19]

Here we assume the combined action of VIP and GABA act to modulate the strength of the coupling between the ventral and dorsal phase clusters in the SCN as a function of the entrained day-length. This conceptional model, summarized in Fig. 4.1, may be translated into a coupled phase oscillator system,

$$\frac{d\phi_k^v}{dt} = \omega_k^v + \frac{K_{vv}}{M_v}\sum_{j=1}^{M_v}\sin(\phi_j^v - \phi_k^v) + \frac{K_{dv}}{M_d}\sum_{j=1}^{M_d}\sin(\phi_j^d - \phi_k^v) + \epsilon Q(\phi_k^v)\delta(t-t') + \sqrt{D}\eta_k^v(t) \tag{4.1a}$$

$$\frac{d\phi_k^d}{dt} = \omega_k^d + \frac{K_{dd}}{M_d}\sum_{j=1}^{M_d}\sin(\phi_j^d - \phi_k^v) + \frac{K_{vd}}{M_v}\sum_{j=1}^{M_v}\sin(\phi_j^v - \phi_k^d) + \sqrt{D}\eta_k^d(t), \tag{4.1b}$$

where $Q(\phi)$ gives the microscopic phase response curve of the ventral oscillators to light and $\eta_k^{v,d}$ defines a white noise process i.e. $\langle\eta_k(t)\rangle = 0$ and $\langle\eta_k(t)\eta_l(t')\rangle = 2\delta_{kl}\delta(t-t')$. The ϵ factor scales the microscopic phase response curve and is taken to be a small parameter. The coupling strengths are given as $K_{from,to}$ and we let $M_{v,d}$ indicate the total number of oscillators which fall into the ventral and dorsal phase clusters. We

define $q = M_v/(M_v + M_d)$ to be the fraction of ventral (sensing) oscillators in the population and $p = 1 - q$.

Finally, we allow the oscillators within the ventral and dorsal regions to be heterogeneous in their intrinsic frequencies and assume each cluster has a Cauchy (Lorentzian) distribution of frequencies,

$$g_{v,d}(\omega) = \frac{1}{\pi} \frac{\gamma}{(\omega - \omega_0^{v,d})^2 + \hat{\gamma}^2}, \tag{4.2}$$

with the mean frequency $\omega_0^{v,d}$ and dispersion parameter $\hat{\gamma}$.

In addition to daily timekeeping, the SCN is also responsible for storing seasonal day-length information [23, 97, 144]. It has been shown by several experimental groups that the phase difference between the dorsal and ventral clusters grows with the seasonal day-length, making this a leading hypothesis for how seasonal information is encoded in the SCN[105, 40]. Additionally, it has been suggested the physiological root of this seasonal variation in the phase difference is alterations in the coupling forces in the SCN [105, 32, 18]. Thus, we incorporate seasonal effects (day-lengths) into our model by allowing the coupling strengths K_{vd} and K_{dv} to vary with the seasonal day-length, as these coupling terms will be seen to control the phase difference between the ventral and dorsal populations.

4.2.2 Macroscopic Model

The model for the mammalian SCN as given in Eq. 4.1 gives a high-dimensional representation of the dynamical state of the circadian rhythm as $M_v + M_d = \mathcal{O}(10^4)$. This high dimensional representation of the system makes analytical analysis of the light-response difficult. Therefore, we make use of the m^2 ansatz to derive a low-dimensional macroscopic model for the ventral and dorsal phase clusters (see Chapter. II). Crucially, the use of this ansatz may be justified through comparison of the

core assumption with experimental data on the phase distribution of cellular oscillators in the mammalian SCN.

First, we define the Daido order parameters [31, 30] for the ventral and dorsal phase clusters as:

$$Z_n^v = \frac{1}{M_v}\sum_{j=1}^{M_v} e^{in\phi_j^v}, \qquad Z_n^d = \frac{1}{M_d}\sum_{j=1}^{M_d} e^{in\phi_j^d}, \tag{4.3a}$$

where $n \in \mathbb{Z}$. The special case of $n = 1$ gives the classical Kuramoto order parameter $Z_1^{v,d} = R_1^{v,d} e^{i\psi_1^{v,d}}$, where R is known as the phase coherence and gives a measure of the overall synchrony in the population: when $R_1 = 1$ the population is phase locked in perfect synchrony and $R_1 = 0$ when the population is completely desynchronized. Additionally, ψ_1 gives the mean phase of the population. For simplicity of notation we will drop the subscript for the Kuramoto order parameters, i.e. $Z_1^{v,d} = Z^{v,d} = R^{v,d} e^{i\psi^{v,d}}$. Using these order parameter definitions we may rewrite Eqs. 4.1 as,

$$\frac{d\phi_k^v}{dt} = \omega_k^v + K_{vv}\,\mathrm{Im}[e^{-i\phi_k^v} Z^v] + K_{dv}\,\mathrm{Im}[e^{-i\phi_k^v} Z^d] + \sqrt{D}\eta_k^v(t) \tag{4.4a}$$

$$\frac{d\phi_k^d}{dt} = \omega_k^d + K_{dd}\,\mathrm{Im}[e^{-i\phi_k^d} Z^d] + K_{vd}\,\mathrm{Im}[e^{-i\phi_k^d} Z^v] + \sqrt{D}\eta_k^d(t), \tag{4.4b}$$

with Im denoting the imaginary part of the expression. In the continuum limit $M_{s,n} \to \infty$ Eqs. 4.4 give rise to continuity equations for the phase density functions $f^{v,d}(\omega, \phi, t)$,

$$\frac{\partial f^{v,d}}{\partial t} + \frac{\partial}{\partial \phi}(f^{v,d} W_{v,d}) + D\frac{\partial^2 f^{v,d}}{\partial \phi^2} = 0 \tag{4.5a}$$

$$W_v = \omega + K_{vv}\,\mathrm{Im}[e^{-i\phi} Z^v] + K_{dv}\,\mathrm{Im}[e^{-i\phi} Z^d] \tag{4.5b}$$

$$W_d = \omega + K_{dd}\,\mathrm{Im}[e^{-i\phi} Z^d] + K_{vd}\,\mathrm{Im}[e^{-i\phi} Z^v]. \tag{4.5c}$$

Let us consider the Fourier series representation of the phase density functions $f^{v,d}(\omega,\phi,t)$,

$$f^{v,d} = \frac{g_{v,d}(\omega)}{2\pi}\left(1 + \left[\sum_{k=1}^{\infty} A_k^{v,d}(\omega,t)e^{ik\phi} + \text{c.c}\right]\right), \tag{4.6}$$

where c.c stands for the complex conjugate. Inserting the Fourier series representation into the continuity equation gives a system for the Fourier coefficients $A_k^{v,d}(\omega,t)$,

$$\frac{(A_k^v)'}{k} + (i\omega + Dk)A_k^v + \frac{K_{vv}}{2}\left[\tilde{Z}^v A_{k+1}^v - Z^v A_{k-1}^v\right] + \frac{K_{dv}}{2}\left[\tilde{Z}^d A_{k+1}^v - Z^d A_{k-1}^v\right] = 0, \tag{4.7a}$$

$$\frac{(A_k^d)'}{k} + (i\omega + Dk)A_k^d + \frac{K_{dd}}{2}\left[\tilde{Z}^d A_{k+1}^d - Z^d A_{k-1}^d\right] + \frac{K_{vd}}{2}\left[\tilde{Z}^v A_{k+1}^d - Z^v A_{k-1}^d\right] = 0, \tag{4.7b}$$

with the tilde representing the complex conjugate. In the continuum limit the Daido order parameters $Z_n^{v,d}$ are given by,

$$Z_n^{v,d}(t) = \int_0^{2\pi}\int_{-\infty}^{\infty} f^{v,d}(\omega,\phi,t)e^{in\phi}d\omega d\phi, \tag{4.8a}$$

$$= \int_{-\infty}^{\infty} \tilde{A}_n^{v,d}(\omega,t)g_{v,d}(\omega)d\omega, \tag{4.8b}$$

using that all the terms in the Fourier series integrate to zero except the $n = k$ term. Further, since we approximate the natural frequency distribution as a Cauchy/Lorentzian distribution (Eq. 4.2) we may evaluate the integral (Eq. 4.8b) under the assumption that $A_k(\omega,t)$ may be analytically continued into the complex ω plane [114]. Thus we have that,

$$Z_n^{v,d}(t) = \tilde{A}_n^{v,d}(\omega_0^{v,d} - i\hat{\gamma},t). \tag{4.9}$$

This substitution into Eqs. 4.7 gives,

$$\frac{(Z_k^v)'}{k} = i\omega Z_k^v - \hat{\gamma} Z_k^v + \frac{K_{vv}}{2}\left[Z^v Z_{k-1}^v - \tilde{Z}^v Z_{k+1}^v\right] + \frac{K_{dv}}{2}\left[Z^d Z_{k-1}^v - \tilde{Z}^d Z_{k+1}^v\right] - DkZ_k^v \tag{4.10a}$$

$$\frac{(Z_k^d)'}{k} = i\omega Z_k^d - \hat{\gamma} Z_k^d + \frac{K_{dd}}{2}\left[Z^d Z_{k-1}^d - \tilde{Z}^d Z_{k+1}^d\right] + \frac{K_{vd}}{2}\left[Z^v Z_{k-1}^d - \tilde{Z}^v Z_{k+1}^d\right] - DkZ_k^d \tag{4.10b}$$

Finally, we consider the system with $k = 1$ and apply the m^2 ansatz ($Z_m = |Z_1|^{m^2-m} Z_1^m$ or $R_m = R_1^{m^2}$, $\psi_m = m\psi_1$). Applying the m^2 ansatz and separation into the real and imaginary parts of the expressions gives a four dimension system describing the phase coherence $R_{v,d}$ and mean phase $\psi_{v,d}$ of each cluster. However, with a change of variables $\theta = \psi_d - \psi_v$ ("phase gap") and letting $\Delta\omega = \bar{\omega}_d - \bar{\omega}_v$ and $\gamma = \hat{\gamma}_{v,d} + D$ we arrive at a three dimensional system of equations:

$$\dot{R}_v = -\gamma R_v + \frac{K_{vv}}{2} R_v(1 - R_v^4) + \frac{K_{dv}}{2} R_d(1 - R_v^4)\cos(\theta) \tag{4.11a}$$

$$\dot{R}_d = -\gamma R_d + \frac{K_{dd}}{2} R_d(1 - R_d^4) + \frac{K_{vd}}{2} R_v(1 - R_d^4)\cos(\theta) \tag{4.11b}$$

$$\dot{\theta} = \Delta\omega - G\sin(\theta) \tag{4.11c}$$

$$G = \frac{R_v R_d}{2}\left[K_{vd}\left(R_d^2 + \frac{1}{R_d^2}\right) + K_{dv}\left(R_v^2 + \frac{1}{R_v^2}\right)\right]. \tag{4.11d}$$

By setting $\bar{\omega} = q\omega_0^v + p\omega_0^d$, we can define $\Omega = q\dot{\psi}_v + p\dot{\psi}_d$ as the collective frequency of the system in a synchronous state,

$$\Omega = \bar{\omega} + H\sin(\theta) \tag{4.12a}$$

$$H = \frac{R_v R_d}{2}\left[qK_{dv}\left(R_v^2 + \frac{1}{R_v^2}\right) - pK_{vd}\left(R_d^2 + \frac{1}{R_d^2}\right)\right] \tag{4.12b}$$

We note that both the collective amplitudes R_v, R_v and the frequency Ω depend on the phase gap variable θ within our model. In order to facilitate our analysis we define

Parameter	Value
$\bar{\omega}_v$	$2\pi/24.5$
$\bar{\omega}_d$	$2\pi/23.5$
γ	0.024
K_{vv}	0.095
K_{dd}	0.07
K_{vd}	αK_{dv}
K_{dv}	0.05
α	2.0
q	0.5

Table 4.1: Parameter sets used for numerical simulations in this chapter (default parameter set). These parameters give steady state values of $R_v^* = 0.81$, $R_d^* = 0.84$, $\theta^* = 0.06$. To ease the numerical simulations we assume γ is determined by the heterogeneity and set the noise strength to zero ($D = 0$).

a default parameter set for this model given in Table 4.1. Under this parameter set Eqs. 4.11 evolve to a fixed point (R_v^*, R_d^*, θ^*) with a collective frequency Ω^*-we will use starred quantities to refer to fixed points solutions.

Finally, we note that experimental evidence has shown that the phase gap between the dorsal and ventral populations is typically a small variable $\theta^* \in [0, 0.5]$ radians for photoperiods in the range of 6-18 hours of light [105], although it may grow considerably when mice are kept in twenty hours or more of light each day [40].

4.2.3 Components of the Collective Phase Response Curve

The collective phase response to a stimulus may be defined by the shift in the mean-phase $\psi = Arg(Z)$ induced by the light perturbation. For a brief (Dirac $\delta(t-t')$ function) stimulus we may break the collective phase shift into two components [89]:

1. The prompt phase shift (Δ_0) induced at $t = t'$ the instant the stimulus is applied.

2. The relaxation phase shift (Δ_R) which results from phase shifts induced as the system relaxes back to its asymptotic state.

The collective phase shift (Δ_∞) is then given by,

$$\Delta_\infty = \Delta_0 + \Delta_R = Arg\left(\frac{\bar{Z}}{Z_0}\right) + \Delta_R \tag{4.13}$$

where we define Z_0 as the order parameter just prior to the perturbation and $\bar{Z}$ as the order parameter just after the perturbation. Notationally, barred quantities will refer to the quantity just after the perturbation is applied.

It is also useful to define the amplitude response curve Λ as a measure of the perturbations transient effect on the amplitude of the collective rhythm,

$$\Lambda = \left|\frac{\bar{R}}{R_0}\right|. \tag{4.14}$$

Given the assumed stability of the limit cycle, perturbations of the amplitude R are expected to decay, thus the amplitude response curve is defined in terms of the initial amplitude reduction imposed on the system.

4.2.4 Single Population Case

We first consider the collective phase response for a single population of oscillators, that is, we consider the case where all oscillators in the population receive the light stimulus. These results will aid our consideration of the two population case, as they can be used to describe the initial phase shift in the ventral oscillator population. In Chapter III, we derived an asymptotic formula for the collective phase response of a single population of Kuramoto-Sakaguchi oscillators making use of the Ott-Antonsen formalism. In this section we adapt those results to study phase shifts in a population which follows the m^2 ansatz as has been found in experimental measurements of the SCN phase distribution (Chapter II). For times close to the perturbation $t \approx t'$ we

may approximate the single population continuity equation as,

$$f_t + \frac{\partial}{\partial \phi}\left[\epsilon f(\omega, \phi, t) Q(\phi(t))\delta(t)\right]. \tag{4.15}$$

We have previously shown that for small ϵ we may approximate the solution of Eq. 4.15 as,

$$\bar{f}(\omega, \phi, t) = f(\omega, \phi - \epsilon Q(\phi)) e^{-\epsilon Q(\phi - \epsilon Q(\phi))}, \tag{4.16}$$

by employing the method of characteristics. Expanding Eq. 4.16 to leading order in ϵ, multiplying by $e^{i\phi}$ and integrating with respect to ϕ and ω gives an expression relating the order parameter after the perturbation $\bar{Z}$ to the order parameter just prior to the perturbation Z_0.

$$\bar{Z} \approx Z_0 + i\epsilon \int_{-\pi}^{\pi} \int_{-\infty}^{\infty} f(\omega, \phi, t) Q(\phi) e^{i\phi} d\omega d\phi. \tag{4.17}$$

Now, we replace the microscopic PRC $Q(\phi)$ with its Fourier Series representation,

$$Q(\phi) = \frac{A_0}{2} + \sum_{n=1}^{\infty} A_n e^{in\phi} + \tilde{A}_n e^{-in\phi}, \tag{4.18a}$$

$$= \frac{A_0}{2} + \sum_{n=1}^{\infty} a_n \sin(n\phi) + b_n \cos(n\phi). \tag{4.18b}$$

Substitution of the Fourier series representation into Eq. 4.17 and applying the definition of the Daido order parameters gives,

$$\bar{Z} = Z_0 + i\epsilon \left[\frac{A_0}{2} Z_0 + \sum_{n=1}^{\infty} A_n Z_{n+1} + A_n^* Z_{n-1} \right]. \tag{4.19}$$

Now we apply the m^2 ansatz [$R_m = R^{m^2}$, $\psi_m = m\psi$] to arrive at an expression for $\bar{Z}$ in terms of Z_0,

$$\bar{Z} = Z_0(1 + i\epsilon\hat{Q}(\psi, R)) \tag{4.20a}$$

$$\hat{Q} = \frac{A_0}{2} + \frac{1}{R}\sum_{n=1}^{\infty} A_n R^{(n+1)^2} e^{in\psi} + A_n^* R^{(n-1)^2} e^{-in\psi}. \tag{4.20b}$$

By applying Eq. 4.13 and Eq. 4.14 we may derive expressions for the prompt resetting Δ_0 and the amplitude response curve Λ respectively,

$$\Delta_0 = Arg\left(\frac{\bar{Z}}{Z_0}\right) = \epsilon Re[\hat{Q}(\psi)] \tag{4.21a}$$

$$\Lambda = \left|\frac{\bar{R}}{R_0}\right| = 1 - \epsilon Im[\hat{Q}(\psi)]. \tag{4.21b}$$

The real part of $\hat{Q}(\psi)$ can be compactly expressed in terms of the Fourier series for the microscopic PRC Eqs. 4.18,

$$Re[\hat{Q}] = \frac{A_0}{2} + \sum_{k=1}^{\infty} f_k(R)[a_k \sin(k\psi) + b_k \cos(k\psi)] \tag{4.22a}$$

$$f_k(R) = \frac{1}{2}R^{k^2}(R^{2k} + \frac{1}{R^{2k}}). \tag{4.22b}$$

From these expressions we can see the principal effect of the phase distribution on the shape of PRC is to re-weight the Fourier harmonics according to $f_k(R)$. As $R \to 1$ we have that $f_k \to 1$ and the collective and microscopic prompt phase response curves coincide. However, when $R < 1$ the first harmonic of the microscopic phase response curve is amplified like $R^3 + \frac{1}{R}$ while the higher harmonics are damped out by higher powers of R.

The imaginary part of $\hat{Q}(\psi)$ can be expressed as,

$$Im[\hat{Q}] = \sum_{k=1}^{\infty} g_k(R)[a_k \cos(k\psi) - b_k \sin(k\psi)] \tag{4.23a}$$

$$g_k(R) = \frac{1}{2} R^{k^2} (\frac{1}{R^{2k}} - R^{2k}). \tag{4.23b}$$

In this case we see that the modulation term $g_k(R)$ goes to zero as $R \to 1$ meaning the amplitude is unaffected by the stimulus in this limit. Additionally we observe that,

$$a_k \cos(k\psi) - b_k \sin(k\psi) \propto \frac{dQ}{d\psi},$$

so we expect the amplitude shifts Λ to be greatest around the zeros of the microscopic phase response curve, with transient increases in R around stable points and decreases around unstable zeros.

4.2.5 Application to Light PRCs

The mammalian phase response curve to light has been characterized over a large variety of species and conditions [137, 72]. Generally, the mammalian circadian rhythm shows small sensitivity to light during the subjective day, phase delays during the early subjective night and phase advances in the late subjective night [121]. Although we expect our results to hold more generally we will focus our attention on phase response curves with this general shape.

The single population results derived in the last section indicate that for microscopic PRC's dominated by their first harmonic, as are commonly assumed in the circadian literature [125, 3], a general amplification in the phase response is expected as the oscillators are more dispersed in phase (either through weaker coupling or greater frequency heterogeneity in the population). This expectation has surfaced in the circadian literature under a variety of guises in the context of both phenomenological and biochemically motivated models [3].

These observations have led to the formation of a rule of thumb in the circadian literature that the magnitude of the phase response should increase when the collective amplitude (phase coherence) decreases [3]. However, our analysis shows this prediction will only hold when the underlying individual/microscopic phase response curve is dominated by its first harmonic-otherwise an overall reduction in the amplitude may be observed [61] (Eq. 4.22). An example of this effect is shown in Fig. 4.2 for a first harmonic phase response curve and a light-like PRC shape. The first harmonic curve shows a uniform increase in amplitude as the phase coherence of the sensing population decreases, whereas the light-like PRC shows a initial decrease in amplitude as the higher harmonics are dissipated.

The general shape of the mammalian phase response curve to light has significant power at higher harmonics [137]. Therefore, the rule of thumb does not necessarily apply in this case. For example, the phase coherence of the ventral (sensor) population is known to decrease with increasing day-length [17] which leads to the expectation of increasing amplitude in the response to light. However, as previously noted the opposite trend has been observed experimentally where organisms entrained to longer day-lengths show *decreased* sensitivity to light-pulses [147].

This reduction in amplitude of the collective phase response, in spite of a reduction in the phase coherence of the sensing population, may be at least partially explained when the higher harmonics in the microscopic phase response to light are taken into consideration. This effect has been noted in the course of simulations [147] and is readily explained by the theory given here using the m^2 ansatz and detailed previously for cases adhering to the Ott-Antonsen ansatz (Chapter III) [61].

In the following section we investigate the effects of only having a fraction of the total population shift in response to a light pulse. This analysis reveals an additional effect which allows the amplitude of the collective phase response to be modulated depending on the degree of asymmetry in the coupling between the ventral and dorsal

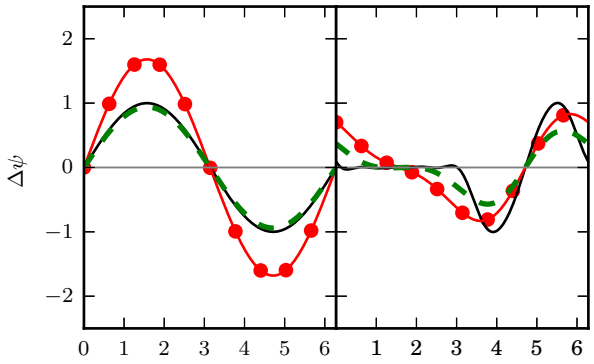

Figure 4.2: Collective phase response curves for two assumed microscopic phase response curves: (left) Simple phase response curve $Q(\psi) = \sin(\psi)$, (right) Light-like PRC shape $Q(\psi) = H(-\sin(\psi))\sin(-2\psi)$. Shown for three phase coherence R values: R=1 (solid black) R=0.6 (dashed green) and R=0.3 (red circles)

populations.

4.3 Two Population Phase Response Curves

We now consider the collective phase response of the circadian model Eqs. 4.11 to brief light pulses using that $\Delta_\infty = \Delta_0 + \Delta_R$. In the first section we compute the prompt phase shifting behavior Δ_0 for the circadian model with a subset of sensor cells and observe the effects on the initial phase shifting behavior (Δ_0). In the next subsection, we present a perturbation technique to determine the relaxation phase shift (Δ_R).

In the figures for this section we consider a microscopic phase response curve $Q(\psi)$ which is fit to experimental measurements of the human phase response curve to brief light pulses [137].

4.3.1 Prompt Resetting Δ_0

We begin by studying the prompt phase shifting curve Δ_0 for the circadian model. By applying Eq. 4.20 and using that the dorsal population is unaffected by the perturbation, we find the order parameter just after the perturbation $\bar{Z} = q\bar{Z}_v + p\bar{Z}_n =$

$qZ_v(1+i\epsilon\hat{Q}(\psi_v))+pZ_d$. Therefore the prompt phase shift Δ_0 for the SCN model can be derived as:

$$\Delta_0 = Arg\left(\frac{\bar{Z}}{Z}\right) = Arg\left(\frac{qZ_v(1+i\epsilon\hat{Q}(\psi_v))+pZ_d}{qZ_v+pZ_d}\right) \tag{4.24a}$$

$$= Arg\left(1+i\epsilon\mu\hat{Q}(\psi_v)\right),\ \mu = \frac{R_v}{R_v+\eta R_d e^{i\theta}} \tag{4.24b}$$

$$= \arctan\left(\frac{\epsilon Re[\mu\hat{Q}(\psi_v)]}{1-\epsilon Im[\hat{Q}(\psi_v)]}\right) \tag{4.24c}$$

$$= \epsilon Re[\mu\hat{Q}(\psi_v)] + \mathcal{O}(\epsilon^2) \tag{4.24d}$$

where $\eta = p/q$ is the ratio of dorsal to ventral (sensors) in the population. We may now expand Eq. 4.24d,

$$C = \frac{R_v[R_v + R_d\eta\cos(\theta)]}{R_v^2 + 2R_vR_d\eta\cos(\theta) + R_d^2\eta^2} \tag{4.25a}$$

$$D = \frac{R_vR_d\eta\sin(\theta)}{R_v^2 + 2R_vR_d\eta\cos(\theta) + R_d^2\eta^2} \tag{4.25b}$$

$$\Delta_0 = C\Delta_0^v + D(\Lambda_v - 1). \tag{4.25c}$$

Which gives an analytical expression for the prompt resetting in our system using our expressions for Δ_0^v and Λ_v for a single population of oscillators (Eqs. 4.21). We note that Eq. 4.25 has the expected limits: As $\eta \to 0$, $\Delta_0 \to \Delta_0^v$ and the system converges to the behavior of a single population of oscillators, in addition as the dorsal population grows ($\eta \to \infty$) we see that $\Delta_0 \to 0$ causing the system to become unresponsive to perturbations. This analytical approximation gives an accurate approximation for the prompt resetting curve when compared with numerical simulations (Fig. 4.3).

It is interesting to note the differences between our system and a single population of oscillators which all shift in response to the stimulus. In the two population system the damping of higher harmonics in the microscopic PRC is also observed, however we additionally see a decrease in the initial shift as a function of the fraction of oscillators

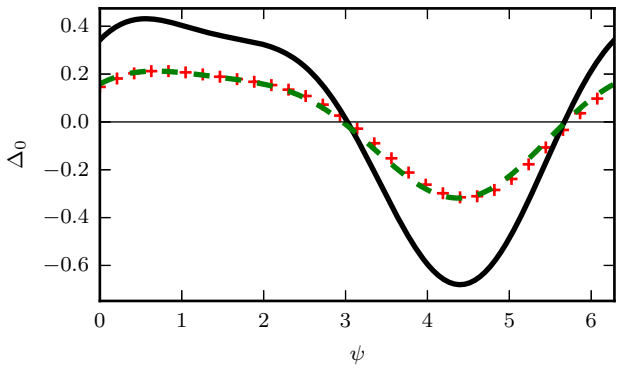

Figure 4.3: Prompt resetting curve with the fraction of sensors in the population $q = 0.50$ and the default parameter values. The microscopic phase response curve (solid black) is fit to the human PRC to a brief light pulse, direct numerical simulations of Eq. 4.1 with $N = 10^4$ (red crosses) and the theoretical prediction Eq. 4.25 (dashed green).

which receive the light pulse. We note that under the assumption that $\theta \approx 0$ we may approximate Eq. 4.25a as,

$$C \approx \frac{qR_v}{qR_v + pR_d}, \tag{4.26}$$

and $C \approx q$ when $R_v \approx R_d$, providing the intuitive result that the overall amplitude of the initial response scales with the fraction q of ventral sensor cells in the population.

In addition, unlike the single population case we see the prompt phase response curve depends on the amplitude response function Λ_v. This dependence leads to a slight change in the zeros (entrainment points) of the prompt PRC when compared to the microscopic PRC since Λ_v will be largest about the zeros of Q. Moreover, this effect is dependent on having a non-zero phase gap between the two populations ($\theta \neq 0$).

4.3.2 Relaxation Phase Shift Δ_R

We now consider the relaxation shift Δ_R which describes the phase shift induced during the return of the system to equilibrium following a perturbation. For the single population case this relaxation phase shift was directly computable from the

Ott-Antonsen equations describing the collective dynamics [89]. This computation relied on the relatively simple spiral isochrons of the Kuramoto-Sakagucki coupling scheme [61, 118, 89].

For the circadian model presented here this quantity can no longer be easily computed by direct integration. However, the relaxation phase shift occurs during the transient decay of the system back to the dynamical fixed point (R_v^*, R_d^*, θ^*) of the macroscopic model. The collective frequency of the unpreturbed system is given by $\Omega^* = \Omega(R_v^*, R_d^*, \theta^*)$. Therefore, the phase shift induced as the system relaxes back to the equilibrium state is given as,

$$\Delta_R = \int_0^\infty \Omega(R_v(t), R_d(t), \theta(t)) - \Omega^* dt = \int_0^\infty \Delta\Omega(t) dt \tag{4.27}$$

Thus, we may calculate the relaxation phase shift by integrating the frequency mismatch between the perturbed system and the steady state system along the trajectory of the system as it returns to equilibrium. The relaxation trajectory may be approximated by a perturbation about the fixed point under the assumption the light-pulse does not induce a large deviation from (R_v^*, R_n^*, θ^*). We set,

$$R_v(t) = R_v^* + \sigma R_v^1(t) + \mathcal{O}(\sigma^2) \tag{4.28a}$$

$$R_d(t) = R_d^* + \sigma R_d^1(t) + \mathcal{O}(\sigma^2) \tag{4.28b}$$

$$\theta(t) = \theta^* + \sigma\theta^1(t) + \mathcal{O}(\sigma^2) \qquad \sigma << 1, \tag{4.28c}$$

with initial conditions $R_v(0) = R_v^* + \Delta R_v$, $R_d(0) = R_d^*$, $\theta(0) = \theta^* + \Delta\theta$ using that the dorsal population is initially unaffected by the light stimulus. The initial changes in R_v and θ can be written in terms of the prompt phase and amplitude response curves for the ventral population: $\Delta R_v = R_v(1 - \Lambda_v)$ and $\Delta\theta = (\psi_d - \bar{\psi}_v) - (\psi_d - \psi_v) = \psi_v - \bar{\psi}_v = -\Delta_0^v$.

Therefore, the leading order terms in σ for the relaxation phase shift is given by,

$$\Delta_R \approx A(1-\Lambda_v) - B\Delta_0^v, \tag{4.29}$$

with the (A,B) constants determined by the model parameters. In practice we find the leading order term in σ is sufficient to provide a good approximation to the numerical solutions (see Fig. 4.4) although higher order terms may be taken in the perturbation series (Eq. 4.28) if additional accuracy is required. We note that (A, B) are a measure of the sensitivity of the collective frequency of the system to perturbations in the amplitude (R_v) and phase gap θ respectively, and are weighted by the stiffness of the system to perturbations in those directions.

To gain intuition of how the circadian model parameters will affect the relaxation phase shifts, we solve for the relaxation terms analytically for a simplified system (see Appendix C). If the amplitude of the ventral and dorsal populations are fixed (without loss of generality let $R_{v,d} = 1$) we find that,

$$B = \frac{q - p\alpha}{1+\alpha}, \qquad\qquad \alpha = \frac{K_{vd}}{K_{dv}}. \tag{4.30}$$

From this simplification we can see that $B \in [-p, q]$ when both coupling terms are positive. Moreover the change occurs at $\alpha = \frac{q}{p}$ from a positive to negative value. Note, for symmetric coupling ($\alpha = 1$) between the regions and $q = p = \frac{1}{2}$ we have $B = 0$. In Fig. 4.5 we show the variation of B with α using both the perturbation approach and the simplified formula Eq. 4.30.

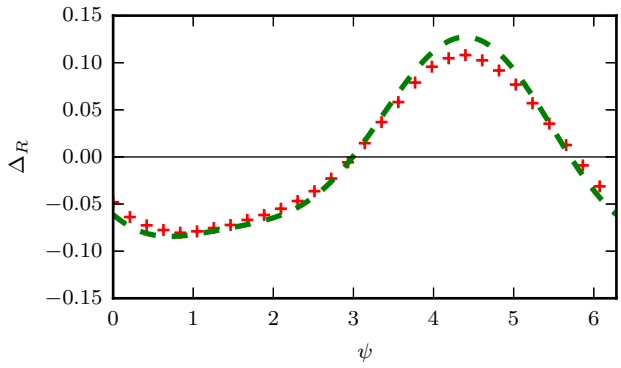

Figure 4.4: Relaxation phase response curve Δ_R using a first order perturbation series to calculate (A, B) in Eq. 4.29 (dotted green) versus numerical simulation(red crosses) for the default parameter values.

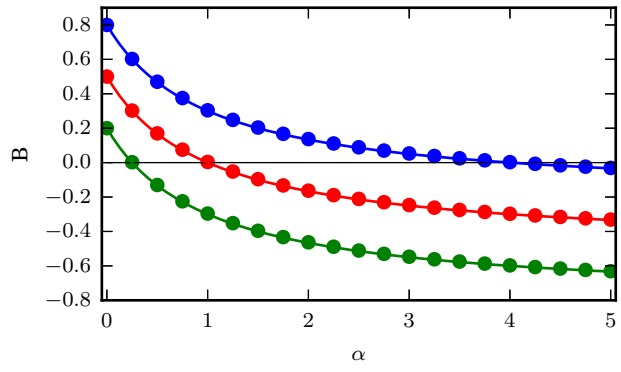

Figure 4.5: Network resistance to phase shifts B versus $\alpha = K_{vd}/K_{dv}$ for the first order perturbation theory (circles) with the default parameter values varying K_{vd} and the approximate formula Eq. 4.30 (solid line) with $q = 0.5$ (red), $q = 0.8$ (blue), $q = 0.2$ (green).

4.3.3 Collective Phase Response Curve

When the prompt phase shift Δ_0 is combined with the relaxation shift Δ_R we find the collective phase response curve Δ_∞,

$$\Delta_\infty = \Delta_0 + \Delta_R = (C - B)\Delta_0^v + (D - A)(1 - \Lambda_v), \tag{4.31}$$

with the constants (A, B, C, D) as defined in the previous sections. In general, we find this approximate formula provides a good approximation to the numerically determined collective phase response (Fig. 4.6). To improve our understanding of the role of light-input to the mammalian circadian system we analyze these results further. Of particular importance is the amplitude of the collective phase response as this determines the entrainment range for weakly forced systems [156].

We first note that the collective PRC for the circadian system carries over many of the trends of the single population model. Namely, we expect that higher harmonics in the microscopic phase response curve will be damped with the first harmonic amplified like $R_v^3 + \frac{1}{R_v}$. This transformation in the shape leads to an overall smoothing effect and is tied to the disorder in the underlying population.

Additionally, we note that the term proportional to the amplitude response curve $(D - A)(1 - \Lambda_v)$ is expected to be of comparatively small magnitude as it is proportional to $\frac{1}{R_v} - R_v^3 \to 0$ as $R_v \to 1$. Moreover the amplitude response curve reaches its maximum values around the zeros of the individual phase response curve. Thus, the amplitude of the collective phase response curve is largely determined by the $(C - B)\Delta_0^v$ term, while a shift in the entrainment points is determined by the $(D - A)(1 - \Lambda_v)$ term.

From Eq. 4.31 we see the amplitude of the collective PRC is influenced by the sign of the B constant as determined by the relaxation dynamics. Positive values of B indicate the relaxation shift acts to decrease the initial phase shift thus providing

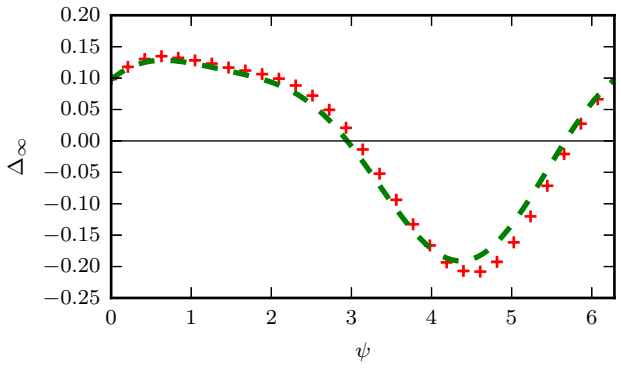

Figure 4.6: Collective phase response curve for the theoretical curve (Eq. 4.31) (dotted green) versus numerical simulation (red crosses) for the default parameter values.

a resistance to the phase shift. Negative values of B indicate the initial shift is reinforced/increased during the transient relaxation, while a value near zero indicates the relaxation shift has a small effect on the collective phase response.

The simplified expression in Eq. 4.30 allows for intuition on the scale and sign of B. In particular we can see the value of B scales with the ratio of the feedforward coupling strength K_{vd} to the feedback strength K_{dv}. For a balanced system $K_{vd} = K_{dv}, q = 0.5$ we observe that $B = 0$, although by varying this ratio of coupling strengths the system can toggle between a resistant/reinforcing behavior to the initial phase shifts.

For a pure feedforward network, where $K_{dv} = 0$, the B term is positive and the effect of having a fractional sensor population on the amplitude of the collective phase response disappears. In this limit the phase shift in the ventral population is imposed on the dorsal population over time. Thus, when $K_{dv} \neq 0$ the non-sensing dorsal population can act as a feedback on the phase shifts and integrate the current phase shift against the past history.

Therefore, we see that the entrainment range of a two-population system is crucially dependent on the ratio of the coupling strengths between the sensing (ventral) and non-sensing (dorsal) populations (Fig. 4.7). By adjusting the ratio of these coupling strengths the size of the light response may be modulated.

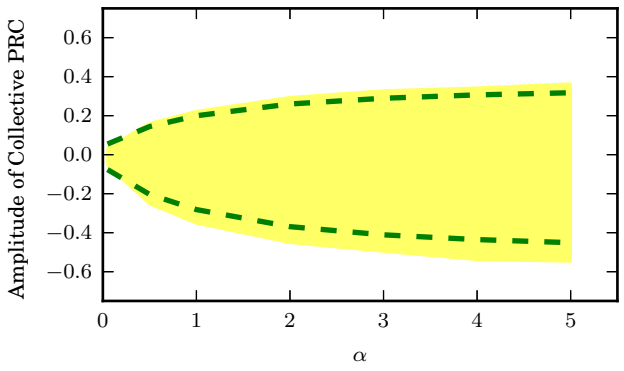

Figure 4.7: The amplitude of the collective phase response curve as a function of $\alpha = K_{vd}/K_{dv}$. The range of the numerical collective phase response is highlighted in yellow and the theoretical prediction of the amplitude (Eq. 4.31) is shown as dotted green lines.

4.4 Seasonal Effects on Light Resetting

Our study of the collective phase response in a two-population model identified the relative strengths of the intra-population coupling forces as an important factor in determining the amplitude of the phase response. Experimental evidence has found that the amplitude of phase shifts induced by a light-stimulus decreases in mammals entrained to long day-lengths [147, 126]. This could be explained in our framework by an increase in the network resistance to the phase shift (B), for animals exposed to long day-lengths.

To evaluate this hypothesis we may check for consistency against two other seasonal light effects on mammalian circadian rhythms: Seasonal encoding and light entrainment after-effects. First, we consider seasonal encoding. Experimental evidence has indicated that the phase difference between the dorsal and ventral phase clusters grows with the day-length [105, 40]. Within our model this corresponds to the variable $|\theta^*|$ growing with the entrained day-length. We make use of the hypothesis that these changes in θ occur through an adjustment of the couping strengths rather than a change in the intrinsic periods in the ventral/dorsal SCN [32, 105, 40]. Thus, we consider the intrinsic periods to be constant while allowing the coupling

strengths to vary, an assumption which has some experimental justification [40].

Let $\chi \in [0,1]$ be the photoperiod, or the fraction of the circadian day in which the organism is exposed to light. Considering Eq. 4.11 we see the steady state phase gap θ^* is given by,

$$\theta^*(\chi) = \arcsin\left(\frac{\Delta\omega}{G(\chi)}\right) \approx \left(\frac{\Delta\omega}{G(\chi)}\right) \tag{4.32a}$$

$$\frac{d|\theta^*|}{d\chi} = \frac{-|\Delta\omega|G'(\chi)}{G(\chi)^2} \tag{4.32b}$$

From this we can see that we must have $G'(\chi) < 0$ to allow the absolute value of the phase gap to increase with the photoperiod length.

Additionally, we observe that θ^* will only show significant variation for a small range $G(\chi) = \mathcal{O}(\Delta\omega)$ and will asymptote to a small value for $G(\chi)$ outside this range. This nonlinear dependence of the phase gap $\theta^*(\chi)$ with asymptotic values for short photoperiods has been observed in experiments using both *Per2* and *Bmal* circadian phase markers [105, 40].

Moreover, the macroscopic model also identifies a fundamental trade-off as the photoperiod is lengthened. As $G(\chi)$ decreases towards $\Delta\omega$ the phase gap increases quickly. However, a further increase in χ will cause the system to undergo a bifurcation where the ventral and dorsal regions decouple from one another. Thus, we predict that organisms which show robust seasonal adjustment necessarily must approach a bifurcation to desynchrony/large phase gaps at long photoperiods. Therefore, organisms which show robust decreases in $G(\chi)$, thereby showing larger changes in the phase gap variable θ^* as the photoperiod lengthens, will also approach a bifurcation to desynchrony more closely and display rhythm abnormalities.

In fact, several species of mammals show desynchrony or large phase gaps when perturbed outside their normal photoperiodic range by unnatural lighting conditions (e.g. constant light) [40, 162, 111]. Moreover, it has been observed that hamsters

which show robust seasonal adjustments to short daylengths have a higher propensity for rhythm abnormalities under constant lighting conditions-illustrating the trade-off identified by our analysis [38].

In order to relate these properties to reduced light phase-resetting responses at long photoperiods we now recall a predominant circadian after-effect to light-entrainment in mammals [105, 123]: Mammals entrained under short day-lengths show a transient increase in period when moved to a dark environment. The long day length after-effect works in an opposite direction by inducing a short period with the magnitude of the period change increasing with the entrained day length. In the context of our model this implies that $\frac{d\Omega}{d\chi} > 0$ in Eq. 4.12. Expanding this condition gives,

$$\frac{d\Omega}{d\chi} = H'(\chi)\sin(\theta^*) + H(\chi)\cos(\theta^*)\frac{d\theta^*}{d\chi} > 0. \tag{4.33}$$

Applying the assumption that θ^* is a small variable we may simplify this condition to give,

$$\Delta\omega\left[\frac{H'(\chi)G(\chi) - H(\chi)G'(\chi)}{[G(\chi)]^2}\right] > 0, \tag{4.34}$$

and we consider the case that $\Delta\omega > 0$ as indicated by experimental evidence [11, 105, 106]. Under the approximation that $R_v \approx R_d$ we have that $2H(\chi) \approx qK_{dv}(\chi) - pK_{vd}(\chi)$ and $G(\chi) \approx K_{dv}(\chi) + K_{vd}(\chi)$. This simplification allows us to express our approximation for the network resistance to phase shifts B (Eq. 4.30), in terms of H and G,

$$\frac{1}{2}B(\chi) \approx \frac{H(\chi)}{G(\chi)}. \tag{4.35}$$

Thus, taking the derivative with respect to the the photoperiod χ,

$$\frac{1}{2}\frac{dB}{d\chi} = \frac{H'(\chi)G(\chi) - H(\chi)G'(\chi)}{[G(\chi)]^2} > 0, \tag{4.36}$$

we see that the network resistance to phase shifts B will increase with the photoperiod directly from the after-effect condition (Eq. 4.34). This gives the surprising result that seasonal entrainment after-effects and the reduced sensitivity to light-pulses at long photoperiods are intimately related to one another. In fact, the presence of one implies the other in our model. Additionally, we see that the seasonal adjustment condition $G'(\chi) < 0$ is consistent with the after-effect and increasing phase shift resistance condition (Eq. 4.36). Therefore, we find the adjustment of couping strengths required to explain three predominant light mediated circadian effects are all mutually consistent within our model.

4.5 Conclusions

In this work we focus on phase resetting to light in mammalian rhythms making use of the m^2 ansatz to derive a simplified model of the central clock. The reduced model holds the advantage that the collective variables (R_v, R_d, θ) all have physiological interpretations and are measurable in experimental treatments. We have focused on the effects of heterogeneity in oscillator frequencies, the shape of the microscopic phase response curve to light, the effects of only a fraction of populations receiving direct light input and variation of the coupling strengths between regions on the phase resetting response.

Similar to previous work on this subject we find heterogeneity of the population changes the shape, amplitude and zeros of the collective phase response curve [61, 89]. Moreover, we note these alterations occur through a re-weighting of the Fourier components of the collective phase response with the first harmonic amplified and higher

harmonics being damped out as the oscillators spread out in phase. We find examination of only the first harmonic terms may give misleading results when considering phase resetting to light in mammals.

The effect of having a fraction of the population receive light-input can lead to a reduction in the overall amplitude of the collective phase response. However, we find this effect is dependent on the coupling between the oscillators in the SCN. In a feedforward network, where the sensing ventral cells project more strongly on the non-sensing dorsal cells than the feedback connection, the initial shift induced on the sensing population is largely imposed on the total population over time. Thus, for pure feedforward network architectures the effect of a fractional sensing population is to induce a time delay on the shift of the population mean phase.

However, when feedback coupling from the dorsal cells to the sensing ventral populations is significant we see the reduction in the initial shift caused by the fractional sensing is retained and even reinforced over time. This leads to the conclusion that the relative coupling strengths between the ventral and dorsal oscillators allows the system to weight phase shifts induced by light differently. The re-weighting of the coupling strengths between the subpopulations with seasonal changes in day length may act like the aperture on a camera by allowing the sensitivity of the clock to light to vary with the total amount of light input received. In short days the feed-forward connection is weighted more strongly to allow for larger responses when light input is more scarce. In contrast, relative weighting of the feedback connection more strongly in long days results in a reduction in light sensitivity when more light is received over the course of the day.

These results may also have applications to the study of aging in the circadian clock. In a similar manner to long-day lengths, older animals tend to show reduced phase coherence and the clock neurons are thought to be more weakly coupled as the animals age [41, 110, 109]. Moreover, these aged animals also show reduced phase-

shifts in response to light stimuli and slower entrainment to shifted light schedules [13, 131, 146, 14]. Our analysis reveals this reduction in phase shifting capacity may be explained in terms of a reduction in the ratio of the feed-forward to feedback coupling between the ventral and dorsal populations.

Our results are consistent with current ideas of how seasonal information is encoded in the mammalian circadian clock [105, 39] and provide an explanation for mammals showing reduced phase shifts to light when entrained to long day lengths [147, 126]. Furthermore, our model reveals an intimate connection between seasonal day-length encoding, seasonal entrainment after-effects and the amplitude of the phase-response to light. Additionally, we find the change in coupling strengths with the day-length required to explain each of these phenomena are mutually consistent within our model.

However, our results remain to be strengthened both from a biological and theoretical standpoint. In order to derive these results we have assumed an all-to-all connectivity between clock cells in the SCN and simple sinusoidal coupling between the oscillators. However, the connectivity in the SCN is known to be much more complex [2]. An important extension of these results would be to consider phase resetting in a general circadian network building on previous results [80, 79].

From a biological standpoint it remains to be tested whether an increasing resistance to phase shifts under long-day lengths underlies the decreased sensitivity to light pulses for organisms entrained to long day-lengths. This prediction seems testable by measuring initial phase shifts to light and comparing these with the asymptotic phase shifts obtained over long-times. This would be particularly interesting if the effect was seen to vary with the entrained day-length and could provide evidence for a variation in the relative coupling strengths between the ventral and dorsal SCN with seasonal day-length. Recent experimental evidence suggests that the coupling strength, as determined globally in the SCN, decreases with increasing day-lengths

which could provide indirect evidence for this hypothesis [18].

CHAPTER V

Macroscopic Models for Human Circadian Rhythms

5.1 Introduction

Disrupted circadian rhythms have been implicated in a vast array of both mental and physical health maladies including cancer, diabetes, addiction, depression and sleep disorders [1, 64, 49, 90]. Moreover, the efficacy of health treatments has been found to vary in a circadian manner meaning knowledge of a patient's circadian phase could allow for more effective treatments with reduced side-effects [88, 66]. Therefore, it is a matter of vital importance to understand and predict human circadian rhythms.

The maintenance of healthy circadian rhythms requires them to be synchronized to environmental cycles by outside forces known as zeitgebers. In mammals, the most powerful zeitgeber is the daily light cycle [123]. Daily light cycles are sensed in the retina and passed directly along the retino-hypothalmic tract to the master circadian clock [98]. The mammalian master circadian clock has been localized to the suprachiasmatic nucleus (SCN) a cluster of twenty thousand neurons in the hypothalamus [103, 139] . Each of these thousands of clock neurons in the SCN contain an intricate genetic feedback loop which cycles with a period close to 24 hours [92]. The emergent rhythm produced collectively by these clock neurons drives peripheral

circadian cycles found throughout the body [33].

The study of human circadian rhythms has been approached using three principal paradigms. First, through the use of model organisms which allow for invasive examinations of the master clock, coupling agents and molecular details of the clock. Secondly, through careful laboratory based human studies which track circadian dynamics through the use of one of several reliable markers for the human circadian rhythm. Finally, in recent years technological advances have allowed for the collection of large datasets of self-reported survey data from individuals outside the laboratory setting [151, 128, 159].

Studies in model organisms have revealed the details of the genetic feedback loop present in each clock neuron as well as the coupling forces between the neurons which help shape the circadian waveform produced by the SCN. The circadian waveform is known to vary under a variety of conditions including age, seasonal day-length and light history of the animal [39]. Laboratory studies of human circadian rhythms have produced an increased understanding of how light-input is integrated into the master-circadian clock as well as careful measurements of key parameters such as the human circadian period. Large datasets of self-reported circadian data have been used to study the variation in circadian dynamics across the human population [151, 128, 159]. In particular, these studies have begun to uncover the prevalence of different chronotypes, defined by the angular relationship between the light and circadian cycles, in the human population.

From a mathematical modeling perspective, the increased knowledge of the details of circadian timekeeping has led to a divergence in the field. Detailed high-dimensional models have been created to explain and predict the molecular data sets generated through study of model organisms [32, 76]. In contrast, models of human circadian data have remained phenomenological and low-dimensional to avoid over-fitting the available data and to reduce the computational burden of simulations. However, these

two modeling approaches have not been integrated to allow for the exchange of knowledge between the molecular and human paradigms. In order to incorporate molecular data, models of human circadian dynamics need to be derived systematically from more detailed high-dimensional models of the master circadian clock.

A mathematical technique capable of supporting such a derivation was introduced by Edward Ott and Thomas Antonsen in 2008 [114]. Their technique can be used to reduce a large system of heterogeneous coupled phase oscillators to a low-dimensional macroscopic model. Recently this technique was applied to the study of circadian rhythms directly for the first time [93]. However, recent evidence has shown the accuracy of the Ott-Antonsen approach can be improved upon for describing mammalian circadian rhythms [62]. In Chapter II we introduced a new ansatz, the m^2 ansatz, which provides a systematic procedure for the extraction of low-dimensional macroscopic models for biological networks of coupled oscillators [62].

In this work we demonstrate the use of the m^2 ansatz [62] in modeling the light-response of human circadian rhythms. Starting from a phase oscillator description of the SCN we derive a low-dimensional model for the human circadian clock and fit the parameters to available data. The flexibility and extensibility of our approach allows for the derivation of both a single population and a two population description of the core clock. We validate the model parameter fits against three additional data sets, and compare the predictions of our models against a predominant phenomenological model for the human circadian clock.

5.2 Results

5.2.1 Previous Models

The most prolific models of human circadian dynamics are based on the van der Pol (VDP) limit cycle oscillator model [84, 155, 46]. The VDP oscillator provides a

low-dimensional and well understood basis to model the overt circadian rhythms as measured by markers such as core body temperature and melatonin levels. As our knowledge of the light-response of the human circadian rhythm has grown, a series of modifications have been introduced to the original models [68, 85, 46]. These progressive modifications have allowed the VDP models to continue to make accurate quantitative and qualitative predictions of the light-response of the human circadian rhythm.

For our purposes we choose to study the simplest VDP model currently used in predicting human circadian rhythms [46],

$$\frac{dx}{dt} = \frac{\pi}{12}(x_c + B(t)) \tag{5.1a}$$

$$\frac{dx}{dt} = \frac{\pi}{12}\left\{\mu\left(x_c - \frac{4x_c^3}{3}\right) - x\left[\left(\frac{24}{0.99669\tau_x}\right)^2 + kB(t)\right]\right\}. \tag{5.1b}$$

The parameters τ_x and μ determine the period of the oscillator and the stiffness of the oscillator, respectively. In Eq. 5.1 the variable $B(t)$ is a transformed version of the light stimulus $L(t)$ according to the *Process L* formalism [85]. The dynamics of *Process L* adds one dynamical dimension to the model and is given by,

$$\frac{dn}{dt} = 60\left[\alpha(L)(1-n) - \beta n\right] \tag{5.2a}$$

$$\hat{B}(t) = G(1-n)\alpha(L) \tag{5.2b}$$

$$\alpha(L) = \left(\frac{L(t)}{I_0}\right)^p \tag{5.2c}$$

$$B(t) = \hat{B}(1 - 0.4x)(1 - 0.4xc). \tag{5.2d}$$

We note that Eq. 5.2d, called the sensitivity modulation, assumes the amplitude of the transformed light input $B(t)$ varies as a function of the phase of the master circadian clock [46]. In order to tie the limit cycle to an experimental circadian marker, the minimum value of the dynamic variable x is taken to coincide with the core body

temperature minimum. The parameter values we use are as specified in Serkh et al [132]. The accuracy and simplicity of this model has led to its application to many open questions in human chronobiology including jet-lag, sleep dynamics and the treatment of circadian disorders [117, 52, 132, 151].

Despite the tremendous success of the VDP formalism in modeling human circadian rhythms, the lingering phenomenological basis remains and can limit the models utility. The variables (x_c, x) and parameter μ do not have interpretations which can be tied to the known physiology of the master circadian clock. Thus, the circadian phase and amplitude measured experimentally can be only loosely interpreted within the VDP formalism. In addition, the lack of a physiological origin for the parameters makes the incorporation of many molecular data sets problematic. For example, the overt circadian rhythm described by the VDP models is known to be produced through the aggregation of the rhythmic contributions of thousands of coupled noisy heterogeneous biochemical oscillators. This large ensemble of coupled oscillators produces an intricate circadian waveform within the SCN which varies with age, seasonal day-length, light history, and a host of other factors [41, 38, 39]. The VDP model formalism has only a limited use in the study these phenomena.

In addition, large data sets have begun to shed more light on the diversity of chronotypes present in the human population [151, 128, 159]. In understanding human chronotypes the phenomenological basis for the VDP model could cripple the ability of researchers to incorporate differences between individual's circadian rhythms beyond variations in the intrinsic circadian period [117]. Variations in the circadian period can only partially explain the variation observed in human chronotypes [35, 34]. In applications, the diagnosis and treatment of circadian disorders will likely require additional knowledge beyond variations in the intrinsic circadian period [34].

5.2.2 Derivation of a Macroscopic Model

Overcoming the limitations of the VDP modeling formalism will require moving beyond a phenomenological paradigm. In this spirit we begin with a high-dimensional model which describes the phase of each clock cell in the SCN. We assume the clock neurons are weakly coupled, that is we make the assumption that deviations off the autonomous limit cycle induced by the coupling forces are sufficiently small to be safely ignored. Additionally, we assume the coupling between the oscillators is all-to-all and is sufficiently weak that the contributions may be averaged into a coupling function with a single harmonic [86]. We allow for heterogeneity in the natural frequency ω_i of each clock cell and include a white noise factor in time progression of each oscillator. These assumptions lead to the following model for each clock neuron $i = 1, 2...N$,

$$\frac{d\phi_i}{dt} = \omega_i + \sqrt{D}\eta_i(t) + \frac{K}{N}\sum_{j=1}^{N}\sin(\phi_j - \phi_i) + B(t)Q(\phi_i) \tag{5.3a}$$

$$Q(\phi_i) = \sigma - A_1\sin(\phi_i + \beta_1) - A_2\sin(2\phi_i + \beta_2) \tag{5.3b}$$

where η_i is a white noise process with $\langle\eta_i\rangle = 0$ and $\langle\eta_i(t)\eta_j(t')\rangle = 2\delta(t-t')\delta_{ij}$, and δ_{ij} is the Kronecker delta. For reasons that will become apparent in the course of the dimension reduction we will assume that the heterogeneity in the natural frequencies of the clock neurons follows a Cauchy (Lorentzian) distribution,

$$g(\omega) = \frac{\gamma}{\pi[(\omega-\omega_0)^2 + \gamma^2)]}, \tag{5.4}$$

where ω_0 is the median frequency and γ sets the spread of the distribution about the median value. The $Q(\phi)$ function describes the phase response curve of the individual clock neuron to a brief light-stimulus and the coefficients A_1, A_2 scale the first and second harmonic components of the phase response curve respectively. Finally, as in

the VDP model the time-dependent input $B(t)$ gives the form of the light stimulus after processing by the visual system. We model the processing of light information along the retino-hypothalamic tract using a slight modification in the $\alpha(L)$ term of the Kronauer-Jewett *Process L* formalism (Eq. 5.2) [85]. That is, we define the transformation from the raw light input $L(t)$ to the processed light input to the circadian clock $B(t)$ as,

$$\frac{dn}{dt} = 60\left[\alpha(L)(1-n) - \delta n\right], \tag{5.5a}$$

$$\alpha(L) = \frac{\alpha_0 L(t)^p}{L(t)^p + I_0}, \tag{5.5b}$$

$$B(t) = G(1-n)\alpha(L). \tag{5.5c}$$

For a large system of coupled phase oscillators it is useful to define the Daido order parameters of the phase distribution [31, 30] as,

$$Z_m(t) = R_m(t)e^{i\psi_m(t)} = \frac{1}{N}\sum_{j=1}^{N} e^{im\phi_j(t)}, \tag{5.6}$$

where ϕ_j are the phases of the oscillators, R_m are the phase coherences and ψ_m are the mean phases. Typically, only the first term is considered $Z_1 = R_1 e^{i\psi_1}$ and is known as the Kuramoto order parameter. Here R_1 measures the amplitude of the collective behavior of the oscillator population with R_1 near zero indicating a near-uniform distribution of phases among the oscillators and $R_1 = 1$ perfect synchrony with all oscillators in the same phase.

While the phase model coarse-grains over the biochemical details of each clock neuron, the large number of neurons in the SCN means it is still very high dimensional $N = \mathcal{O}(10^4)$ model. Given this high-dimensionality it is natural to consider the continuum limit as the number of oscillators grows to infinity $N \to \infty$. In the continuum limit, the oscillator population may be described as a phase density func-

tion $f(\omega, \phi, t)$ which gives the density of oscillators with frequency ω at phase ϕ. The time-evolution of f is given by a continuity equation,

$$\frac{\partial f}{\partial t} + \frac{\partial}{\partial \phi}(fv) + D\frac{\partial^2 f}{\partial \phi^2} = 0, \tag{5.7a}$$

$$v = \omega + \sigma B(t) + \mathrm{Im}\left[Ke^{-i\phi}Z_1 + H_1(t)e^{-i\phi} + H_2(t)e^{-2i\phi}\right] \tag{5.7b}$$

$$H_1(t) = A_1 e^{-i\beta_1} B(t) \qquad H_2(t) = A_2 e^{-i\beta_2} B(t) \tag{5.7c}$$

where Im denotes the imaginary part of the expression. The Fourier series decomposition of f is given by

$$f = \frac{g(\omega)}{2\pi}\left(1 + \left[\sum_{n=1}^{\infty} A_n(\omega, t)e^{in\phi} + \text{c.c.}\right]\right), \tag{5.8}$$

where c.c. stands for the complex conjugate of the expression and $g(\omega)$ is the distribution of natural frequencies of the oscillators. Substitution of the Fourier series for f into the continuity equation yields

$$\begin{aligned} &\frac{\dot{A}_n}{n} + (i\omega + i\sigma B(t) + Dn)A_n + \frac{K}{2}\left(Z_1 A_{n+1} - \bar{Z}_1 A_{n-1}\right) \\ &+ \frac{1}{2}\left(H_1 A_{n+1} - \bar{H}_1 A_{n-1}\right) + \frac{1}{2}\left(H_2 A_{n+2} - \bar{H}_1 A_{n-2}\right) = 0. \end{aligned} \tag{5.9}$$

where barred quantities are the complex conjugate. In the continuum limit the Daido order parameters Z_m are given by

$$Z_m(t) = \int_0^{2\pi}\int_{-\infty}^{\infty} f(\omega, \phi, t)e^{im\phi}d\omega d\phi = \int_{-\infty}^{\infty} \bar{A}_m(\omega, t)g(\omega)d\omega \in \mathbb{C} \tag{5.10a}$$

using that all oscillating terms in the Fourier series for f integrate to zero except for $n = m$. If $g(\omega)$ is given by a Cauchy distribution with median ω_0 and dispersion parameter γ (Eq. 5.4), the integral (Eq. 5.10a) can be evaluated as a residue by

arguing that $A_m(\omega, t)$ may be analytically continued into the lower half of the ω plane [114]. Evaluation of the contour integral gives $Z_m(t) = \bar{A}_m(\omega_0 - i\gamma, t)$. Using this substitution for the Daido order parameters allows us to re-write Eq. 5.9 as follows,

$$\frac{\dot{Z}_n}{n} = (i\omega_0 + \sigma B(t) - \gamma - Dn)Z_n + \frac{K}{2}(Z_1 Z_{n-1} - \bar{Z}_1 Z_{n+1}) + \\ + \frac{1}{2}(H_1 Z_{n-1} - \bar{H}_1 Z_{n+1}) + \frac{1}{2}(H_2 Z_{n-2} - \bar{H}_2 Z_{n+2}). \tag{5.11}$$

Now, we set $n = 1$ to get an equation of motion for the Kuramoto order parameter $Z_1 = R_1 e^{i\psi_1}$,

$$\dot{Z}_1 = (i\omega_0 + i\sigma B(t) - \gamma - D)Z_1 + \frac{K}{2}\left(Z_1 - Z_2\bar{Z}_1\right) + \frac{1}{2}(H_1 - \bar{H}_1 Z_2) + \frac{1}{2}(H_2\bar{Z}_1 - \bar{H}_2 Z_3). \tag{5.12}$$

However, we note that Eq. 5.12 is not a closed system for Z_1, as it depends on higher order Daido order parameters (Z_2, Z_3). Therefore, some simplification is required to achieve a reduction in the dimensionality of the system.

In Chapter II, we found that the higher order Daido order parameters may be expressed in terms of Z_1 for a large class of coupled oscillator networks [62]. We termed the relation the m^2 ansatz and it is given by, $Z_m = |Z_1|^{(m^2-m)} Z_1^m$ or $R_m = R_1^{m^2}, \psi_m = m\psi_1$. Significantly to this work, examination of the phase distribution of clock neurons in whole SCN explants shows the m^2 ansatz describes the phase distribution accurately [2, 62].

Applying this moment-closure and separating the real and imaginary parts for Z_1

gives the following two-dimensional model for the human circadian clock:

$$\dot{R} = \left(\frac{K}{2} - D - \gamma\right) R_1 - \frac{K}{2} R_1^5 + L_R(R, \psi) \tag{5.13a}$$

$$\dot{\psi} = \omega_0 + L_\psi(R, \psi) \tag{5.13b}$$

$$L_R(R, \psi) = \frac{A_1}{2} B(t)(1 - R^4)\cos(\psi + \beta_1) + \frac{A_2}{2} B(t) R(1 - R^8)\cos(2\psi + \beta_2)$$

$$L_\psi(R, \psi) = \sigma B(t) - \frac{A_1}{2} B(t)\left(\frac{1}{R} + R^3\right)\sin(\psi + \beta_1) - \frac{A_2}{2} B(t).(1 + R^8)\sin(2\psi + \beta_2)$$

where we have dropped the subscripts on the Kuramoto terms $Z_1 = Re^{i\psi}$. The two variables of the model have the benefit of having direct physiological interpretations: $R \in [0, 1]$ measures the collective amplitude of the oscillator population and ψ gives the mean phase of the population. The terms L_R and L_ψ give the impact of the light input on the amplitude and mean phase of the circadian clock respectively. Our systematic derivation also allows the parameters of the macroscopic model to be traced back to the properties of the high-dimensional microscopic model for each phase oscillator.

5.2.3 Two Population Model

Another advantage of our modeling approach is that alterations in the microscopic model may be easily incorporated and a new macroscopic model derived. To illustrate this process we note that physiological investigations of the mammalian SCN have revealed it may be functionally clustered into two principal regions: the ventral (core) and the dorsal (shell) clusters [45]. Especially pertinent to the study of light on the mammalian circadian clock, is the discovery that light information channeled to the SCN from the eyes along the retino-hypothalamic tract projects mainly onto the ventral cluster of oscillators [98]. As discussed in Chapter IV this can have significant effects on the phase-resetting properties of the system as only a fraction of the oscillator population phase-shifts in response to a stimulus. This also allows

for more complex processing of the light-information as the phase-shift of the sensing ventral population is integrated against the non-sensing population to produce a composite phase-shift (see Chapter IV).

Within our formalism we may easily generalize the derivation used for a single population model of the SCN to include the division of neurons into the ventral and dorsal clusters (see Chapter IV for a two population derivation). We assume the same structure and coupling terms as depicted in Fig. 4.1. The addition of the dorsal population of oscillators yields a five-dimensional macroscopic model for the circadian clock which describes the collective amplitude of the ventral and dorsal populations (R_v, R_d) and the mean phase of each population (ψ_v, ψ_d), along with the *Process L* light-processing variable $B(t)$. The two population model is given by,

$$\dot{R}_v = -\gamma_v R_v + \frac{K_{vv}}{2} R_v(1 - R_v^4) + \frac{K_{dv}}{2} R_d(1 - R_v^4)\cos(\psi_d - \psi_v) + L_R(R_v, \psi_v) \tag{5.14a}$$

$$\dot{R}_d = -\gamma_d R_d + \frac{K_{dd}}{2} R_d(1 - R_d^4) + \frac{K_{vd}}{2} R_v(1 - R_d^4) \tag{5.14b}$$

$$\dot{\psi}_v = \omega_v + \frac{K_{dv}}{2} R_d(\frac{1}{R_v} + R_v^3)\sin(\psi_d - \psi_v) + L_\psi(R_v, \psi_v) \tag{5.14c}$$

$$\dot{\psi}_d = \omega_d - \frac{K_{vd}}{2} R_v(\frac{1}{R_d} + R_d^3)\sin(\psi_d - \psi_v) \tag{5.14d}$$

$$L_R = \frac{A_1}{2} B(t)(1 - R_v^4)\cos(\psi_v + \beta_1) + \frac{A_2}{2} B(t) R_v(1 - R_v^8)\cos(2\psi_v + \beta_2) \tag{5.14e}$$

$$L_\psi = \sigma B(t) - \frac{A_1}{2} B(t)\left(\frac{1}{R_v} + R_v^3\right)\sin(\psi_v + \beta_1) - \frac{A_2}{2} B(t)(1 + R_v^8)\sin(2\psi_v + \beta_2), \tag{5.14f}$$

with the *Process L* light-processing variable $B(t)$ defined as for the single population model. A distinct advantage of the two-population model is that it allows for finer adjustments of the coupling forces within the SCN. Thus, the coupling strengths may be adjusted to allow for seasonal variations in the circadian waveform found in model organisms. For example, studies in rodents have found that in longer day-lengths

the ventral and dorsal populations tend to separate in phase [105]. Within the two-population model this may be included by allowing the inter-region coupling strengths K_{vd}, K_{dv} to decrease in increasing day-lengths. As shown in the last chapter this manipulation of the coupling strengths can lead to the reduction in the phase-shifting response observed experimentally when organisms are entrained to long day-lengths as seen experimentally [126, 147].

5.2.4 Parameter Fitting

In order to allow for prediction of human circadian rhythms we fit our model to available data on the human circadian light response. We make use of three experimental measurements of the human phase response curve to light to calibrate our model [75, 138, 26]. These three phase response curve studies use a similar protocol for the assessment of circadian phase shifts while varying the light stimulus applied considerably. Hilaire et al [138] use a single bright white stimulus one-hour in length, while Khalsa et al [75] employ a 6.7 hour bright light pulse. Finally, Czeisler et al [26] use a three pulse stimulus delivered over a period of 72 hours. The single light pulse curves show weak or Type 1 phase resetting, meaning the phase response curve is continuous and the phase transition curve (initial phase plotted against final phase) shows an average slope of one [156]. Conversely, the three pulse phase response curve shows Type 0 resetting where the phase transition curve has an average slope of zero [26, 156]. Type 0 resetting is associated with the stimulus driving the system to a phase singularity and produces large phase shifts in the circadian phase [156].

In addition to the phase resetting data-sets, we also make use of experimental measurements of the human light intensity dose response curve [163]. These results study the effects of the differing light intensities on the magnitude of phase delays induced by a light stimulus applied during the early subjective night. The intensity response curve was found to be nonlinear and sigmoidal, with the inflection point

near the light intensities typical of indoor lighting [163].

In order to compare a model with experimental data we define the collective phase $\psi = \pi$ in the single population model and $\psi_v = \pi$ in the two population model, to correspond with the minimum of the core body temperature in humans. In addition, for the two-population model we make the assumption that the core body temperature marker is driven by the ventral SCN. We find this assumption is required for the model to provide good fits to the Type 0 resetting data.

Optimal parameters sets were found using a genetic algorithm based global optimization over the parameter space, with a least-squares cost function. Similar to the process used to fit the VDP model [46], we fit the parameters to a biharmonic function for the Type I phase resetting curves and a smoothed curve for the Type 0 data (Fig. 5.1). In addition, we constructed Markov Chain Monte Carlo (MCMC) ensembles about these optimal parameter sets in order to see the effects of parameter variations on model performance (see Methods). Optimal parameters sets for both models and MCMC quantiles may be found in Appendix D.

A comparison between the VDP model [46] and our models shows each of them are capable of describing the phase response curve data well (Fig. 5.1). However, the alteration of the light processing we introduce allows for an improved fit to the light intensity dosage response curve in our models (Fig. 5.1). In addition, we note that in order to achieve fits to the data for the VDP model the authors introduced an ad-hoc sensitivity modulation function (Eq. 5.2d), which requires the assumption of a significant variation in the light processing as a function of the circadian phase [46]. In fitting our models we find this sensitivity function is not required to describe the phase shifting data.

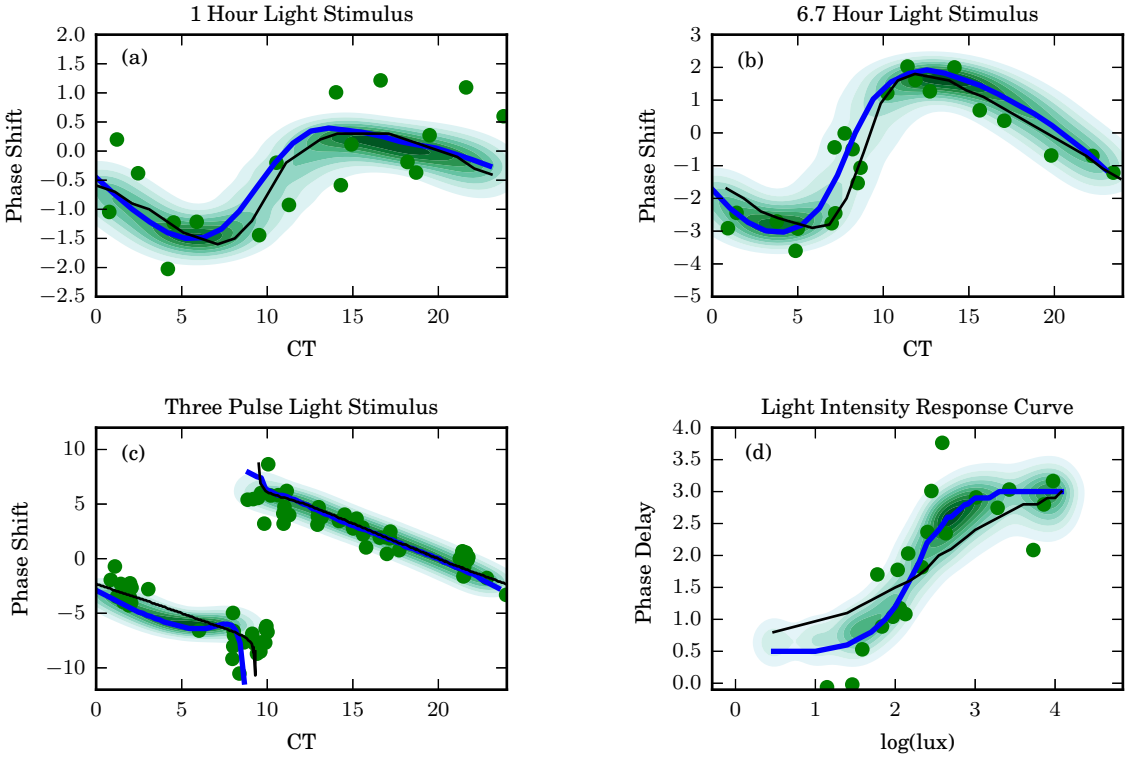

Figure 5.1: (a-c) Single population model parameter fits plotted for three experimental measurements of the human phase response curve to light. (d) Shows the light intensity dosage response curve fits. Thick blue curves show the single optimal parameter fits and the green shading shows the density across the MCMC parameter ensemble. Green dots show experimental data points [75, 138, 26, 163]. Thin black lines show fits using the VDP model [46] for parameter values as given in [132].

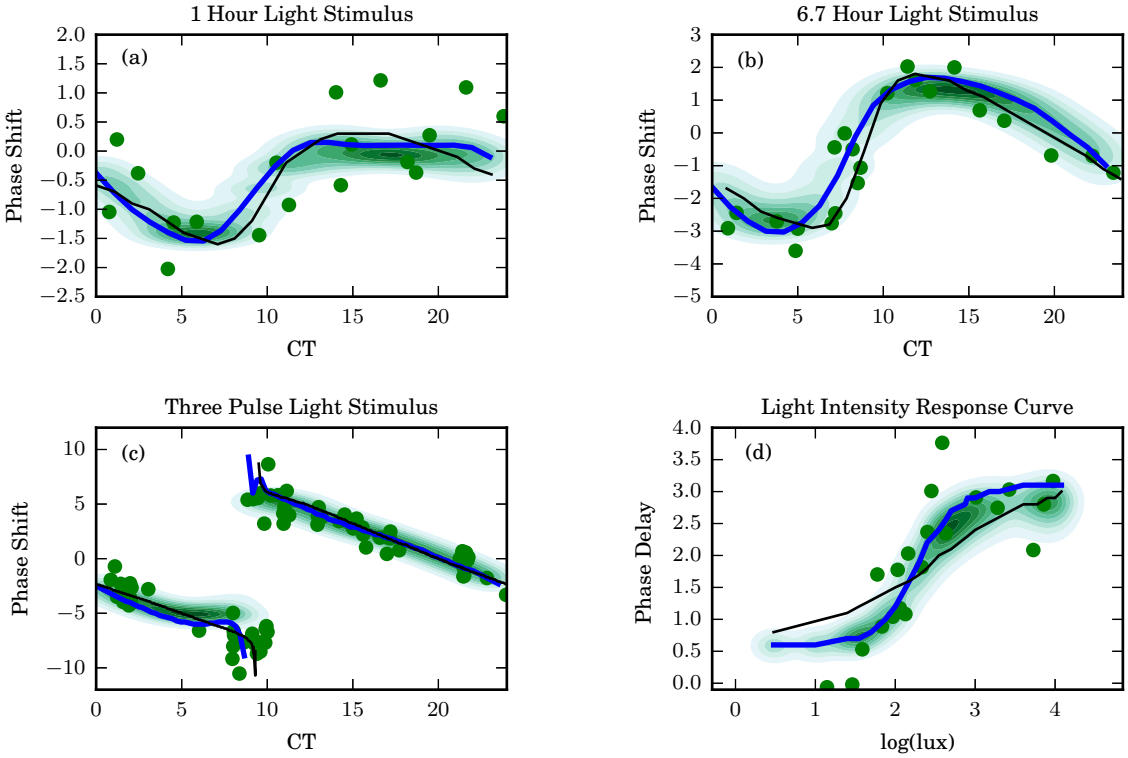

Figure 5.2: (a-c) Two population model parameter fits plotted for three experimental measurements of the human phase response curve to light. (d) Shows the light intensity dosage response curve fits. Thick blue curves show the single optimal parameter fits and the green shading shows the density across the MCMC parameter ensemble. Green dots show experimental data points [75, 138, 26, 163]. Thin black lines show fits using the VDP model [46] for parameter values as given in [132].

5.2.5 Model Validation

In addition to the data sets used in the parameter fitting procedure, we also simulated the model response for three additional experimental protocols in order to validate our parameter fits. The first two of these data sets consider phase-resetting in subjects exposed to intermittent light exposures in the phase delay [57] and phase advance regions [127] of the phase response. In the Rimmer et al experiments subjects were exposed to intermittent bright light exposures of 5.3 and 46 minute lengths alternating with episodes of darkness over a total of 5 hours [127]. The phase shifting efficacy of these intermittent exposures were compared with a base line constant bright light exposure of 5 hours. These intermittent light exposures were found to produce nearly the same magnitude of phase advances as the full light exposure, with the 90 minute intermittent light schedule yielding approximately 90% of the baseline phase shift and the 25 minute schedule producing 70% of the value of the baseline phase shift measured in terms of the median phase shifts of each group. For this validation data set we find the two-population model out performs both the single population and the VDP model (Fig. 5.3(a)). Although each of the models have the property that intermittent light exposures retain a large percentage of the phase shifting capacity of the base line constant light exposures.

The second validation data set measured the effects of intermittent light exposures in the phase delay region of the phase response [57]. Subjects were exposed to a intermittent light schedule consisting of six 15 minute bright light pulses separated by sixty minutes in very dim light. The phase delaying effects of this intermittent light schedule were compared against a baseline light exposure of 6.5 hours of constant bright light. For this data set we find each of the models capture the experimental data closely (Fig. 5.3(b)).

The third validation data set we considered is a duration response curve, measuring the phase delays induced by bright light exposures of different lengths (0.2,1.0,2.5

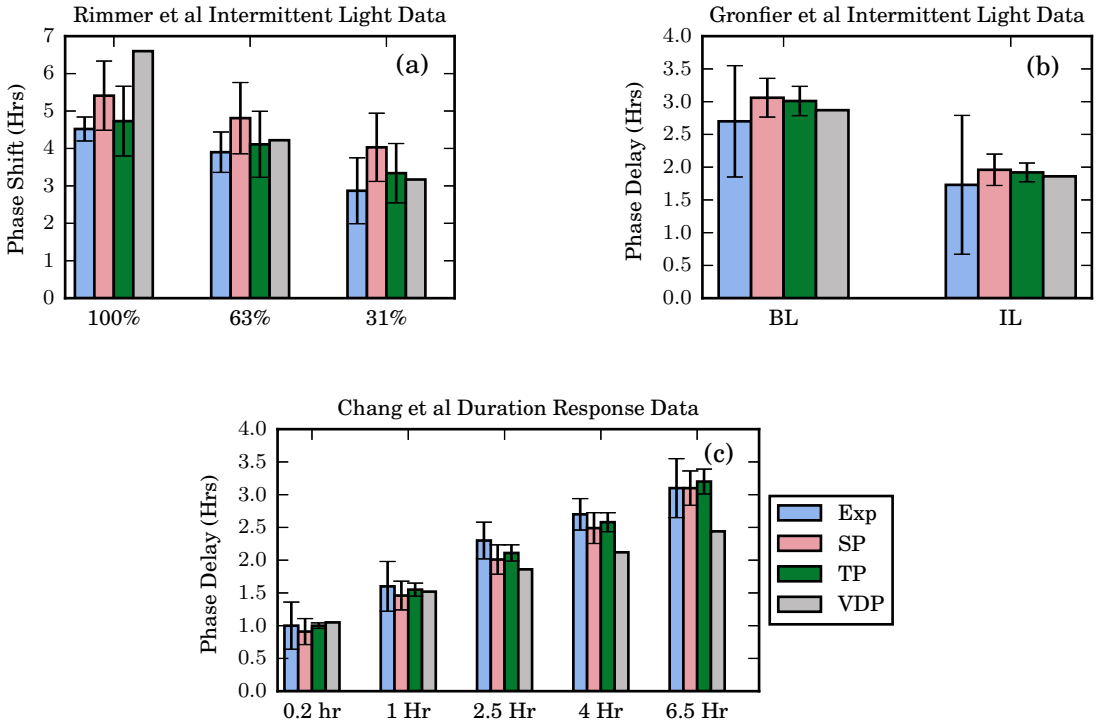

Figure 5.3: Results for the three validation data sets (Exp) using the single population model (SP), two population model (TP) and the VDP model (VDP). Error bars for the single and two population models are taken from the probability density estimated by the MCMC parameter ensemble.

and 4.0 hours) [21]. Similar to the intermittent light experiments, we find each model reproduces the qualitative results. Both the single and two population model were found to reproduce the mean phase shifts accurately (Fig. 5.3). While the VDP model matches the experimental results for shorter light pulses with degrading accuracy for the longer light pulses (Fig. 5.3(c)).

5.2.6 Differences in Model Predictions

A major difference between the VDP model and the models we propose here lies in the assumed sensitivity modulation function (Eq. 5.2d) of the VDP based models. The sensitivity modulation function introduces a strong circadian phase dependence into the amplitude of the processed light input $B(t)$ presented to the circadian oscillator.

The sensitivity function allows the VDP model to match the Type 0 (three-pulse) phase resetting experimental data. Functionally, the sensitivity modulation function amplifies the phase shifts in the critical region for stimuli occurring near the core body temperature minimum. This enables the VDP model to demonstrate Type 0 resetting for relatively high stiffness values μ, which in the absence of the sensitivity function would prevent the oscillator from showing Type 0 resetting. Our formalism does not require the introduction of an ad-hoc sensitivity function to match the Type 0 phase resetting behavior. To compensate for the loss of the sensitivity function, the amplitude recovery dynamics of our models differ significantly from the VDP model.

We find the amplitude recovery rates of the models differ significantly in the absence of time cues. In both the single and two population models, circadian amplitude recovery from small amplitudes takes significantly longer than is predicted by the VDP model (Fig. 5.4(a)). However, when the light entrainment cues are provided the amplitude recovery rate speeds up considerably, such that it is comparable with the rate predicted by the VDP model (Fig. 5.4(b)). This slower amplitude recovery has been observed in laboratory treatments when participants are exposed to circadian amplitude suppressing bright light pulses [70, 69]. The one participant who was kept in darkness following an amplitude suppression showed little evidence of amplitude recovery after four circadian cycles [69]. However, in participants who received an additional light pulse following amplitude suppression, the circadian amplitude was observed to recover to typical levels within three circadian cycles [69]. This overestimate of the amplitude recovery rate from small amplitudes by the VDP model has been noted previously in the literature [67]. However, attempts to remedy this deficiency for VDP based models introduced higher order terms into the dynamics of the amplitude recovery [67]. By comparison, our models do not require higher order terms in the amplitude recovery function, but rather make the hypothesis of weaker coupling forces in the SCN. For small amplitude reductions both the VDP model

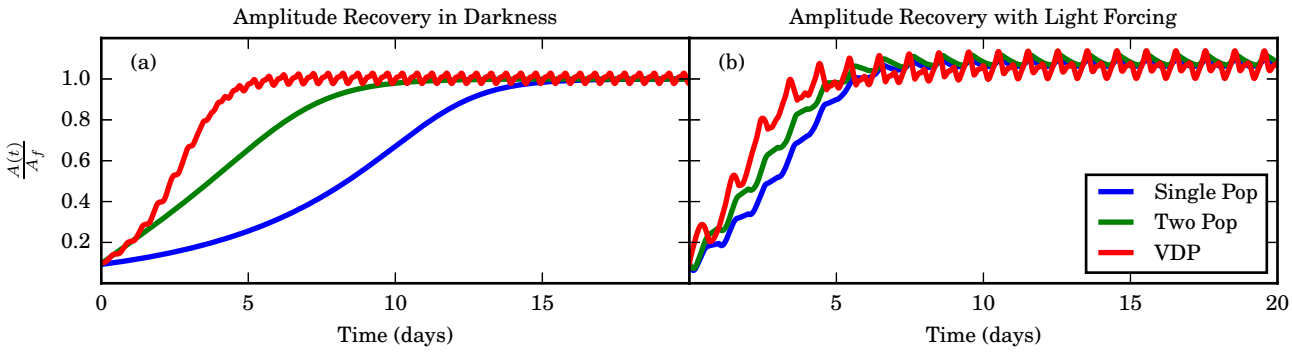

Figure 5.4: Amplitude recovery from small initial amplitudes in the models (a) Shows the recovery of amplitude for the VDP, Single and Two Population models in darkness. (b) Shows amplitude recovery when subjected to a regular 16:8 LD light schedule of 100 lux light following the amplitude reduction.

and our models predict the amplitude recovery will occur quickly, in accordance with experimental results [69].

The difference in the amplitude recovery dynamics also manifests itself in the entrainment of the models to regular light schedules. To study the entrainment of the models we compute the days required to entrain to shifted light schedules in each of the models. To assess entrainment times we compute the number of days required to entrain to within 0.1 radians or $\approx$ 22 minutes of the final stable entrainment angle beginning from all amplitude states and initial phases. The single and two population models make similar predictions for the number days required to entrain to the shifted schedules, however the VDP model predicts significantly longer entrainment times for larger phase shifts (Fig. 5.5). Observing the entrainment dynamics via stroboscopic plots we see our models entrain more quickly due to increased circadian amplitude suppression in response to large shifts in the light schedule (Fig. 5.5). Finally, we note that similar to the VDP model our models demonstrate an asymmetry between the entrainment times for east and west shifts in the light schedule. Of note we find this asymmetry in our models for experimentally measured values of the circadian clock period $\approx$ 24.2 hours [27, 20]. This contrasts with the mechanism suggested

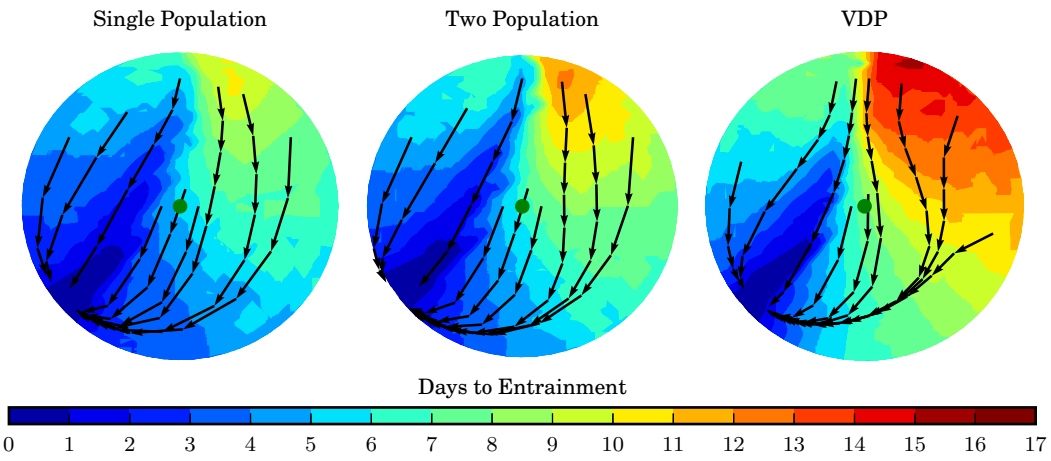

Figure 5.5: Entrainment times to sudden time zone shifts in the single population, two population and VDP models. Colors indicate the days required to entrain to a regular light schedule starting from the amplitude and phase indicated in the circular plot. The amplitudes are normalized between the models to allow comparison, and the orientation of the VDP model plot is reversed for the same reason. Arrows show stroboscopic snapshots of the phase and amplitude at 24 hour intervals during the entrainment process.

by a recent macroscopic model, using the Ott-Antonsen ansatz, which requires an assumption that the human circadian period exceed 24.5 hours [93].

The differences between the model's predictions for entrainment time following a sudden shift in the light schedule should alter model predictions of light therapy prescriptions used in the treatment of circadian maladies [132]. In particular, the increased amplitude malleability of our models will likely have significant effects on predictions of optimal light schedules for re-entrainment, which typically seek to push the system towards the phase singularity to allow for a faster entrainment [132].

In addition to the amplitude recovery and entrainment time differences, we find the entrainment angle is more sensitive to the strength of the entraining stimulus in our models than is predicted by the VDP model. For example, for an individual living on a regular 16:8 light dark schedule with room light levels (100 lux) the core body temperature (CBT) minimum lights occurs 2.9 hours before lights on in both the single and two population models. Under the same 100 lux lighting conditions

the VDP model makes a similar prediction that the CBT minimum will occur 2.4 hours before lights on. However, when the light intensity is raised to $10,000$ lux (typical of outdoor sunlight) our models predict that lights on will occur at an earlier biological time [2.6 hours (single population) and 2.3 hours (two population) after the CBT minimum]. The VDP model predicts a shift in the opposite direction with the difference between lights on and the CBT minimum increasing to 2.8 hours under bright light entrainment. Therefore, our models predict individuals who receive higher light intensities during day-light hours will wake at an earlier biological time. A similar trend was found when subject's circadian markers were compared between natural/outdoor light:dark cycles and an artificial light dominated environment [160].

5.3 Discussion

The m^2 ansatz is consistent with experimental measurements of the phase distribution of circadian neurons and allows for the systematic reduction of high-dimensional stochastic phase oscillator models to low-dimensional macroscopic models. In this work we have shown how the m^2 ansatz may be applied to derive two new models for human circadian dynamics. The m^2 ansatz and the associated dimension reduction procedure are extremely extensible, enabling our models and assumptions to be updated to incorporate new experimental results.

Since our models are derived from high-dimensional phase models describing the phase of each circadian neuron in the SCN, the variables and parameters have inherent physiological interpretations which can be traced back to the high-dimensional single cell model. This allows for the easier incorporation of new experimental results and greater falsifiability than can be achieved with phenomenological models currently in use [46]. Moreover, as our knowledge of population variability increases the physiological interpretations of parameters in our models could allow for personalized models to be constructed based on the peculiar properties of each individual's

circadian dynamics.

To provide predictive models, we fit our macroscopic models to measurements of the human circadian light response. The parameter fits were validated against three additional data sets to evaluate the accuracy of the model predictions. Moreover, we highlight some key differences between our model predictions and a previous phenomenological model based on the van der Pol oscillator. In particular, we find the elimination of the sensitivity modulation function used in the VDP model significantly alters the model predictions on the amplitude recovery dynamics. Our models predict a slower amplitude recovery at smaller amplitudes in the absence of time cues, with a much faster recovery of amplitude predicted when rhythmic light input is provided. This is consistent with available experimental data on circadian amplitude recovery [70, 69].

In addition, we find our models differ significantly from the VDP model in predictions of entrainment times. Weaker coupling in our models leads to predictions of shorter entrainment times to large shifts in the light schedule than predicted by the VDP model. This difference in predictions could significantly change predictions of optimal light based chronotherapies for circadian misalignment [132]. Finally, we observe that our models and the VDP model make opposite predictions on the influence of zeitgeber strength on the entrainment angle. Our models predict entrainment to bright light conditions, typical of the outdoors, will shift circadian rhythms earlier in the solar day while the VDP model shows a weak effect in the opposite direction. Our models predictions align with an experimental study of the influence of outdoor living on circadian rhythms [160].

5.4 Methods

Model simulations were run using a custom C++ library, employing a variable step-size fourth order Runga-Kutta explicit solver for the ODE integrations. Light

schedules for the fitting and validation were reproduced *in silco* from the various experimental protocols [75, 138, 26, 163]. The model was entrained to a regular light schedule for 50 days prior to initialization of the experimental protocols. To mimic the experimental circadian phase determination, the core body temperature (CBT) crossing times [defined to be $\psi = \pi$, $\psi_v = \pi$ for our models] were used to determine the phase shifts induced by the light stimulus.

To quantify the model's adherence to the fitting data sets, we defined a least-squares cost function. Model outputs were evaluated against functions fit to the experimental data, rather than the raw data points. For the Type 1 resetting data we fit a biharmonic function to the data sets [75, 138]. For the Type 0 data each branch of the discontinuous PRC was fit to a function of the form $a+bx+cx^2+d/(\theta-x)^2$ [26]. Given the ambiguity present in the data on the exact placement of the discontinuity, θ was allowed to vary in the range $\theta \in [8.8, 10.05]$ and the minimum distance was assumed in each comparison with the model simulations. For light intensity response curve data we used the four parameter logistic function as specified by the authors in the original work [163].

Optimal parameters were identified using a genetic algorithm for global optimization using a population size of 200 and running for 100 generations. The optimal parameter sets were then selected from the final population produced by the genetic algorithm.

We also implemented a MCMC algorithm in order to explore the cost basin around our optimal parameter sets. Statistical inferences based on the parameter ensemble require knowledge of the variance of the measurements in our fitting data sets. Given the small sample sizes of human studies, estimates of the variance of measurements are lacking. Thus, we assume fixed variances for each measurement in the four experimental protocols used in fitting [$\sigma_C = 0.85$ (Type 0), $\sigma_K = 0.50$ (6.7 hour), $\sigma_H = 0.50$ (1 hour), $\sigma_Z = 0.30$ (Intensity response)]. The MCMC algorithm was implemented

as a custom Metropolis-Hasting's walk across the cost basin. Simulations were run for $N = 1000$ steps in the parameter space and thinned by a factor of five to remove any autocorrelation from the random walk.

CHAPTER VI

Conclusions

A crucial choice in the art of mathematical modeling is the choice of what to leave out of the model. In many cases this choice can be aided by focusing on a scale for the model commensurate with the experimental data the model seeks to explain. For example, in building a model of the circadian rhythms at the cellular scale, the inclusion of a large number of biological components may be appropriate [47, 76, 100, 32]. This level of detail will allow the model to be compared against detailed measurements of the components, and enable the model to make testable predictions of the phenotypes of mutant cells with components removed [47, 76, 100]. However, at the scale of whole organism circadian rhythms a low-dimensional phenomenological model may be more appropriate and offer greater insights into the phenomena [46, 156].

However, biological systems and circadian rhythms in particular are inherently multiscale phenomena and models which are limited to one spatial or temporal scale will suffer from inherent predictive limitations [161]. In circadian rhythms, daily oscillations in behavior and physiology are produced by cellular processes which operate on very short time and spatial scales. These molecular clocks are then integrated into a complex spatial network of interacting clock neurons. This spatial network produces the collective oscillations which drive behavioral oscillations emergently from

the rhythmic contributions of thousands of clock neurons.

Therefore, multiscale mathematical models must be developed which can synthesize hierarchical data and make predictions across divergent time and spatial scales. One answer to the multiscale challenge is the development of numerical methods which allow for the efficient simulation of multiscale models [32]. Alternatively, the multiscale challenge may be addressed through the development of mathematical techniques which allow for freedom of movement between temporal and spatial scales. In this work we have focused on the development of mathematical tools which enable the study of multiscale dynamics in coupled oscillator networks.

The Ott-Antonsen approach is a powerful example of a multiscale mathematical technique which may be applied to coupled oscillator systems to move from a high-dimensional microscopic model to a low-dimensional macroscopic model [114]. We apply the Ott-Antonsen technique to study the response of collective oscillations to perturbations in Chapter III. The application of the Ott-Antonsen technique allowed for the derivation of analytical results detailing how the phase sensitivity of an oscillator population differs from its component oscillators.

In addition, we provide the first investigation of the applicability of the Ott-Antonsen technique to the study of coupled biological oscillators (Chapter II). To assess the applicability of the Ott-Antonsen technique to biological systems we extracted phase distribution estimates from measurements of cellular timecourses in the mammalian circadian clock [2]. We also generated several phase distribution *in silco* data sets for coupled biological oscillators (Repressilators [36, 50], Morris-Lecar neurons [104], and Noisy Modified Goodwin Oscillators [76, 140]). Analysis of these data sets showed that a key assumption of the Ott-Antonsen technique is invalid for these systems. However, we do find evidence of low-dimensional macroscopic dynamics and discover a modification of the Ott-Antonsen technique, the m^2 ansatz, which does describe these systems well. The emergence of the m^2 ansatz is justified through a

simple argument relying on the general phase-locking of oscillators. Moreover, we demonstrate the validity of the m^2 ansatz for a wider class of models then can be studied with the Ott-Antonsen approach (Chapter II). Finally, we demonstrate how the m^2 ansatz may be used to extract a macroscopic model for the stochastic heterogeneous Kuramoto equation.

We apply the m^2 ansatz in Chapter IV to characterize the impact of light on mammalian circadian rhythms. Our analysis clarifies the conditions for a rule of thumb in the circadian literature that oscillators show increasing phase sensitivity as the oscillator amplitude is decreased [125, 3, 156]. In particular, we find this rule depends on the harmonic content of the oscillator's phase response to the stimuli and provide analytic scaling results for the dependence of phase shifting on the collective amplitude. Surprisingly, our analysis reveals an intimate connection between three light-induced effects of mammalian circadian rhythms: seasonal encoding, seasonal after-effects to light entrainment and reduced light sensitivity in long-day lengths. We find each of these phenomena can be parsimoniously explained within our model by an adjustment of coupling forces within the master circadian clock as a function of entrained day-length.

Finally, in Chapter V we apply the m^2 ansatz to derive two simple models for human circadian rhythms. We fit the parameters of our models using the phase response curve measurements in human subjects for three different light stimuli [138, 75, 26]. In addition, we use an experimental human intensity response curve to calibrate and fit our model [163]. We validate our parameter fits through comparison with three additional data sets, and compare our model's predictions with a popular phenomenological model for human circadian rhythms based on the van der Pol (VDP) oscillator [46]. We find our models predict slower amplitude growth than the VDP oscillator model in the absence of light input. This also induces differences between our model's and the VDP based model's predictions of entrainment times to abrupt

shifts in the light schedule. This has particular significance in applications for light based treatments of circadian misalignment disorders such as jetlag or shift work. Finally, we find our models make different predictions on the effect of bright light on the entrainment angle of the circadian clock. Our models predict that extended exposure to bright light typical of the outdoors will lead to circadian alignment such that lights on occurs at an earlier biological time, while the VDP model makes a prediction of a slight shift in the opposite direction.

APPENDICES

APPENDIX A

Supplementary Information for the m^2 ansatz

Data and Mathematical Model Details

Circadian Data

The circadian data shown in Figure. 2.1(a) of the main text is described in detail in Abel et al 2016 [2] and was generously provided publicly by those authors and may be downloaded from https://github.com/JohnAbel/scn-resynchronization-data-2016. In total the public data set has measurements from five different whole SCN explants. In the main text we show the estimated equilibrium phase distribution for SCN 1 in the Abel et al data set. In Fig. A.1 we show the plots for SCN 1-3 (A-C) and SCN 5(D). We excluded SCN 4 from our analysis due to difficulties in estimating the phases of the oscillators from the raw bioluminescence data.

m^2 Ansatz Phase Distribution Function

For the plots in Figure. 2.1 of the main text we show the experimental (numerical) data phase distribution against a theoretical m^2 phase distribution. In this section we show how the theoretical distribution was calculated. We consider the phase

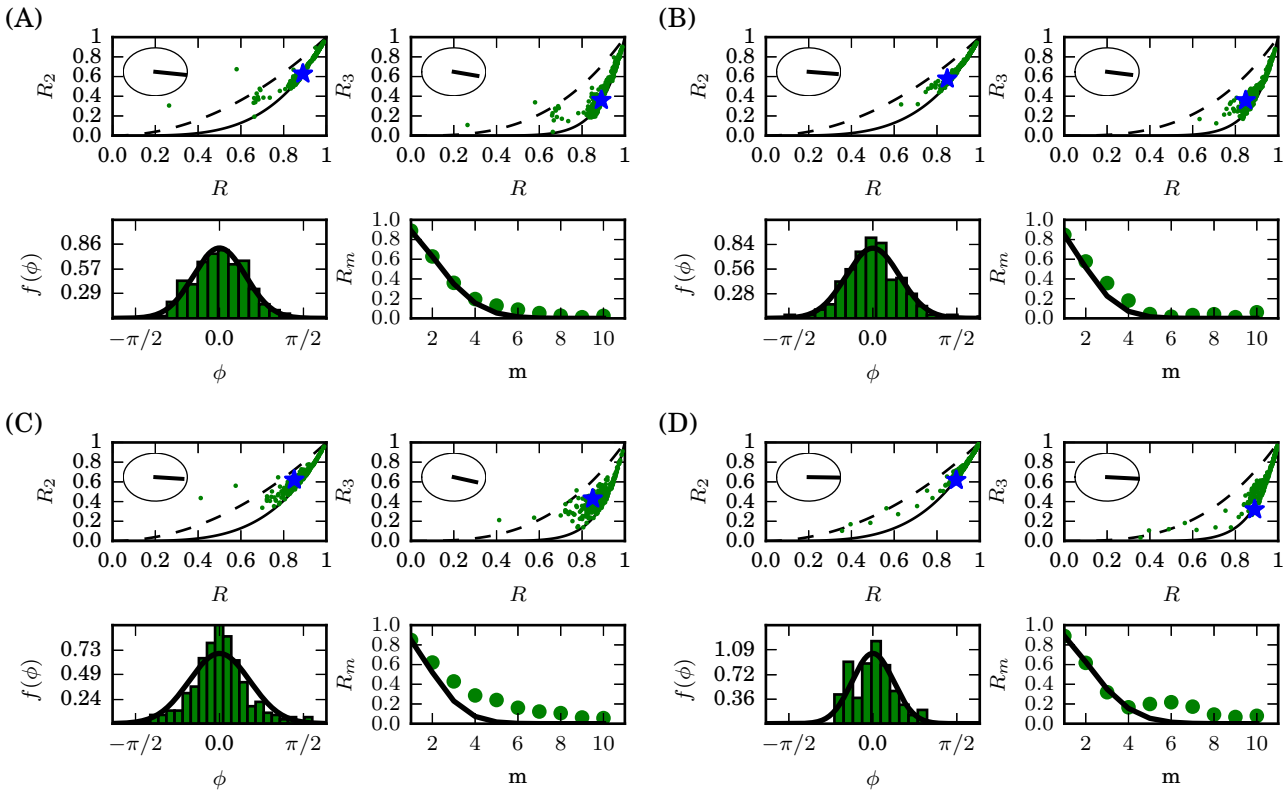

Figure A.1: The low-dimensional structure in the phase distribution of coupled oscillator systems from the Abel et al 2016 [2] circadian data set. (A-D) Show the results from whole suprachaismatic nucleus (SCN) recordings for four different SCN samples (top row) Each green point shows a time measurement of the phase distribution of circadian oscillators. The solid black line shows the relation $R_m = R_1^{m^2}$ and the dashed line the COA relation $R_m = R_1^m$. Inset plots show the circular mean vector of $\psi_m - m\psi_1$ across all observations. (bottom left) shows a histogram of the experimental phase distribution indicated by the blue star in in top row, against the m^2 ansatz phase distribution black line. (bottom right) We plot the first ten Daido order parameters for the experimental phase distribution (green circles) against the m^2 ansatz prediction (black line).

distribution function $f(\omega, \phi, t)$ in the limit as $N \to \infty$ so that it may be considered continuous. Now, consider the Fourier series decomposition of the phase distribution,

$$f(\omega, \phi, t) = \frac{g(\omega)}{2\pi}\left(1 + \sum_{m=1}^{\infty} A_m(\omega, t)e^{im\phi} + \bar{A}_m(\omega, t)e^{im\phi}\right), \tag{A.1}$$

where the bar indicates the complex conjugate and $g(\omega)$ is the distribution of natural frequencies. Integrating both sides with respect to ω yields and expression in terms of the Daido order parameters,

$$f(\phi, t) = \frac{1}{2\pi} + \frac{1}{2\pi}\sum_{m=1}^{\infty} \bar{Z}_m(t)e^{im\phi} + Z_m e^{-im\phi}, \tag{A.2}$$

using the property that

$$Z_m(t) = \int_{-\infty}^{\infty} \bar{A}_m(\omega, t)g(\omega)d\omega. \tag{A.3}$$

Finally, applying the m^2 anstaz $Z_m = R_1^{m^2}e^{im\psi}$ and simplifying gives,

$$f_{MS}(\phi, t) = \frac{1}{2\pi} + \frac{1}{\pi}\sum_{m=1}^{\infty} R^{m^2}\cos(m(\phi - \psi)), \tag{A.4}$$

where f_{MS} is the m^2 ansatz phase distribution. To compare with experimental and numerical data we set $\psi = 0$ and choose R to match the experimental (numerical) data.

Coupled Repressilator Model

We used the coupled repressilator model largely as specified in Garcia-Ojalvo et al 2004 [50]. The repressilator is a network of three transcriptional repressors which each mutually inhibit one another [36]. For our purposes we consider a large collection ($N = 10^4$) of cells which each contain a repressilator genetic oscillator. As in Garcia-

Ojalvo 2004, we assume the cells are coupled through a mean-field quorum-sensing mechanism. The model for each cell i is given by,

$$\frac{da_i}{dt} = -a_i + \frac{\alpha}{1 + C_i^n} \tag{A.5a}$$

$$\frac{db_i}{dt} = -b_i + \frac{\alpha}{1 + A_i^n} \tag{A.5b}$$

$$\frac{dc_i}{dt} = -c_i + \frac{\alpha}{1 + B_i^n} + \frac{\kappa S_i}{1 + S_i} \tag{A.5c}$$

$$\frac{dA_i}{dt} = \beta_i(a_i - A_i) \tag{A.5d}$$

$$\frac{dB_i}{dt} = \beta_i(b_i - B_i) \tag{A.5e}$$

$$\frac{dA_i}{dt} = \beta_i(c_i - C_i) \tag{A.5f}$$

$$\frac{dS_i}{dt} = -k_{s0}S_i + k_{s1}A_i - \eta(S_i - Q\bar{S}), \qquad \bar{S} = \frac{1}{N}\sum_{i=1}^{N} S_i, \tag{A.5g}$$

where lower case variables refer to mRNA and upper case values the protein form of a gene. The parameter values were as specified in Garcia-Ojalvo 2004, for Figure 1(B). We vary the parameter Q to change the coupling strengths between the oscillators. Additionally, heterogeneity was added to the population by drawing β_i from a normal distribution ($\mu = 1$, $\sigma^2 = 0.05$) which produces period heterogeneity in the repressilator population [50].

Morris-Lecar Neural Model

The Morris-Lecar neuronal model [104] for $N = 10^3$ neurons with all-to-all electrical coupling was simulated with parameter values as given in Table. E.1 for the

type II membrane regime. The Morris-Lecar model for each neuron is given by,

$$C\frac{dV_i}{dt} = -\bar{g}_{ca}m_\infty(V_i)(V_i - V_{ca}) - \bar{g}_K w_i(V_i - V_K) - \bar{g}_L(V_i - V_L) \tag{A.6a}$$

$$+ \frac{1}{N}\sum_{j=1}^{N} g_{syn}(V_j - V_i) + I^i_{app} \tag{A.6b}$$

$$\frac{dw_i}{dt} = \phi\frac{w_\infty(V_i) - w_i}{\tau_w(V_i)} \tag{A.6c}$$

$$m_\infty(V_i) = \frac{1}{2}\left[1 + \tanh\left(\frac{V_i - \bar{V}_1}{\bar{V}_2}\right)\right] \tag{A.6d}$$

$$w_\infty(V_i) = \frac{1}{2}\left[1 + \tanh\left(\frac{V_i - \bar{V}_3}{\bar{V}_4}\right)\right] \tag{A.6e}$$

$$\tau_w(V_i) = \frac{1}{\cosh\left(\frac{V_i - \bar{V}_3}{2\bar{V}_4}\right)} \tag{A.6f}$$

Heterogeneity was added such that the firing frequencies of the neurons were normally distributed. Coupling strengths between the neurons were adjusted through the g_{syn} parameter.

Stochastic Modified Goodwin Model

The modified Goodwin model is a simple model of the genetic oscillator in mammalian circadian neurons [76]. Each cell in the population of $N = 10^3$ oscillators is modeled using the modified Goodwin oscillator,

$$\frac{dM_i}{dt} = \alpha_1 f(P_i, A_i, K_d) - \beta_1 M_i + \kappa(\bar{M} - M_i) + \sqrt{D}\eta_1(t) \tag{A.7a}$$

$$\frac{dPc_i}{dt} = \alpha_2 M_i - \beta_2 Pc_i + \sqrt{D}\eta_2(t) \tag{A.7b}$$

$$\frac{dP_i}{dt} = \alpha_3 Pc_i - \beta_3 P_i + \sqrt{D}\eta_3(t) \tag{A.7c}$$

$$f(P, A, K_d) = \frac{A - P - K_d + \sqrt{(A - P - K_d)^2 + 4AK_d}}{2A} \tag{A.7d}$$

$$\bar{M} = \frac{1}{N}\sum_{i=1}^{N} M_i \tag{A.7e}$$

The coupled modified Goodwin oscillator uses the model and parameters as described in Kim et al [76]. The coupling term is taken to be a mean-field average $\bar{M}$ of the mRNA in the population. The oscillators were taken to be identical using the parameters as specified in Kim et al [76] with a weak white-noise term with strength $D = 10^{-6}$ added to each of the species. This system was integrated using a Euler-Maruyama scheme with step-size $h = 0.001$ to generate the *in silco* data. Coupling strengths were manipulated through the κ parameter.

Emergence of the m^2 Ansatz for Complex Networks

Here we give the details of the derivation for the m^2 ansatz for general noisy heterogeneous networks in the main text (Eq. 2.13). Let us begin with the linearized phase oscillator equation from the main text (Eq. 2.11),

$$\dot{\phi}_i = \tilde{\omega}_i - KH'(0)\sum_{j=1}^{N} L_{ij}\phi_j + \sqrt{D}\eta_i(t), \tag{A.8}$$

If we assume each $\phi_j \approx 0$ in equilibrium state $\boldsymbol{\phi}^*$ the Daido order parameters Z_m may be written as,

$$Z_m = \frac{1}{N}\sum_{j=0}^{\infty}\frac{(im)^j||\boldsymbol{\phi}||_j^j}{j!} \tag{A.9a}$$

$$\approx 1 + \frac{im}{N}\sum_{k=1}^{N}\phi_k - \frac{m^2}{2N}\sum_{k=1}^{N}\phi_k^2 + ... \tag{A.9b}$$

Introducing a suitable rotation and using our symmetry assumption on the phase distribution allows us to set $\psi_m = m\psi_1 = 0$. Considering the expected value in time gives,

$$\mathbb{E}[R_m]_t \approx 1 - \frac{m^2}{2N}\mathbb{E}\left[||\boldsymbol{\phi}||_2^2\right]_t \approx \mathbb{E}[R_1^{m^2}]_t, \tag{A.10}$$

for $\mathbb{E}\left[||\boldsymbol{\phi}||_2^2\right]_t$ small. We now consider Eq. A.8 about the deterministic steady state $\boldsymbol{\phi^*} = L^\dagger \tilde{\boldsymbol{\omega}}/(KH'(0))$ where $L^\dagger = \sum_{j=2}^{N} \frac{\boldsymbol{v}_j \boldsymbol{v}_j^T}{\lambda_j}$ is Moore-Penrose pseudoinverse of the normalized Laplacian matrix L. Our assumptions on the network mean that L has real eigenvalues that may be ordered $\lambda_1 = 0 \leq \lambda_2 \leq ...\lambda_N$ with associated eigenvectors $\{\boldsymbol{v}_1, ..., \boldsymbol{v}_N\}$. A change of basis to the eigenvector basis such that $c_i = \boldsymbol{v_i} \cdot \boldsymbol{\phi}$ gives a system of decoupled stochastic differential equations,

$$\delta \dot{c}_i = -K\lambda_i H'(0)\delta c_i + \sqrt{D}\tilde{\eta}_i(t), \tag{A.11}$$

where $\delta c_i = c_i - c^*$ gives the deviation off the deterministic steady state $c_i^* = \boldsymbol{v}_i \cdot \boldsymbol{\phi}^*$. This gives a classic Ornstein-Uhlenbeck process for each δc_i and we find,

$$\mathbb{E}[(\delta c_i)^2]_t = \frac{D}{K\lambda_i H'(0)} \tag{A.12}$$

$$\mathbb{E}[c_i^2]_t = (c_i^*)^2 + \frac{D}{K\lambda_i H'(0)} \tag{A.13}$$

Taking the long-time limit and considering fluctuations about the equilibrium gives,

$$\mathbb{E}[||\boldsymbol{\phi}^*||_2^2]_t = \sum_{j=1}^{N} (c_j^*)^2 + \sum_{j=2}^{N} \frac{D}{K\lambda_j H'(0)}, \tag{A.14a}$$

$$= \sum_{j=2}^{N} \left(\frac{|\boldsymbol{v}_j \cdot \tilde{\boldsymbol{\omega}}|}{K\lambda_j H'(0)} \right)^2 + \frac{D}{K\lambda_j H'(0)}. \tag{A.14b}$$

Therefore, we have derived the condition for the accuracy of the m^2 ansatz as given in the main text (Eq. 2.13).

Network Simulation Details

For the simulations of the heterogeneous noisy Kuramoto equation over complex networks shown in the main text (Fig. 2.3) we considered networks with $N = 10^3$ nodes with noise strength $D = 1$ and Gaussian heterogenity with $\sigma = 1$. These

networks were run for a long-time in order to find the equilibrium phase distribution using a Euler–Maruyama scheme.

The networks were generated using the networkx python package. Barabasi-Albert networks we created using the preferential attachment algorithm with parameter $k = 5$ [12]. Watts-Strogatz networks were generated by local connections to the nearest five neighbors and randomly rewiring the edges with probability $p = 0.2$ [153].

APPENDIX B

Method of Characteristics for Phase Resetting

In this appendix we will consider the partial differential equation version for small perturbations of a coupled oscillator system. At the moment of the perturbation the continuity equation will look like:

$$f_t + \frac{\partial}{\partial \phi}(\epsilon Q(\phi) f(\omega, \phi, t)\delta(t)) = 0 \tag{B.1a}$$

$$f_t + \epsilon\delta(t)Q'(\phi)f + \epsilon\delta(t)Q(\phi)f_\phi = 0 \tag{B.1b}$$

$$f_t + \epsilon\delta(t)Q(\phi)f_\phi = -\epsilon\delta(t)Q'(\phi)f \tag{B.1c}$$

This may be solved using the method of characteristics. This yields three ordinary differential equations:

$$\frac{dt}{ds} = 1 \implies t = s + t_0 \implies t = s \tag{B.2a}$$

$$\frac{d\phi}{ds} = \epsilon\delta(t)Q(\phi) \tag{B.2b}$$

$$\frac{dh}{ds} = -\epsilon\delta(t)Q'(\phi)h \tag{B.2c}$$

To leading order in ϵ we get that $\phi(t) = \phi_0 + \epsilon Q(\phi_0)$ and $h(t) = h_0 e^{-\epsilon Q'(\phi_0)}$. Thus,

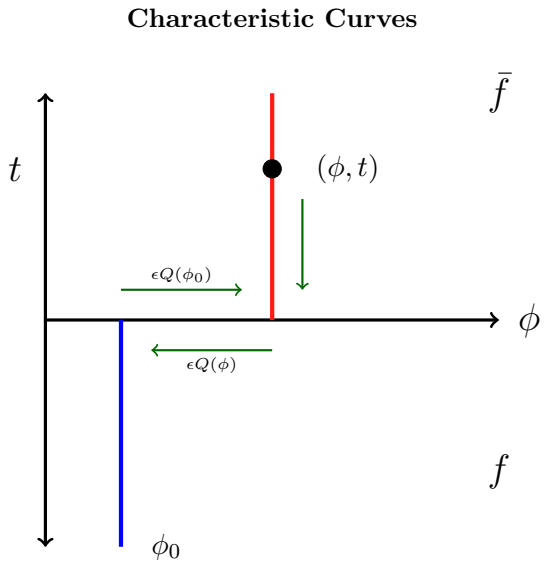

Figure B.1: Depiction of the characteristic curves for the system Eq. B.1c

the distribution after the perturbation $\bar{f}(\omega, \phi)$ may be expressed as,

$$\bar{f}(\omega, \phi) = f(\omega, \phi - \epsilon Q(\phi)) e^{-\epsilon Q'(\phi - \epsilon Q(\phi))} \tag{B.3}$$

to leading order in ϵ. Defining $\rho(\phi)$ as the phase density function,

$$\rho(\phi) = \int_{-\infty}^{\infty} f(\omega, \phi) d\omega, \tag{B.4}$$

and integrating Eq. B.3 with respect to ω gives,

$$\bar{\rho}(\phi) = \rho(\phi - \epsilon Q(\phi)) e^{-\epsilon Q'(\phi - \epsilon Q(\phi))}. \tag{B.5}$$

Let us expand equation B.5 under the assumption of small epsilon,

$$\bar{\rho}(\phi) \approx \rho(\phi) - \epsilon \rho(\phi) Q'(\phi) - \epsilon \rho_\phi(\phi) Q(\phi) + O(\epsilon^2), \tag{B.6}$$

and recall that

$$Z_0 = \int_{-\pi}^{\pi} \rho(\phi) e^{i\phi} d\phi \qquad\qquad \bar{Z} = \int_{-\pi}^{\pi} \bar{\rho}(\phi) e^{i\phi} d\phi. \tag{B.7}$$

Therefore, multiplying B.6 by $e^{i\phi}$ and integrating gives

$$\bar{Z} = Z_0 - \epsilon \int_{-\pi}^{\pi} \rho(\phi) Q'(\phi) e^{i\phi} d\phi - \epsilon \int_{-\pi}^{\pi} \rho_\phi Q(\phi) e^{i\phi} d\phi \tag{B.8}$$

Integrating the second term by parts, in order to move the ϕ derivative yields,

$$\bar{Z} = Z_0 - \epsilon \int_{-\pi}^{\pi} \rho(\phi) Q'(\phi) e^{i\phi} d\phi - \epsilon \left([\rho Q(\phi) e^{i\phi}]|_{-\pi}^{\pi} - \int_{-\pi}^{\pi} \rho(\phi) \frac{d}{d\phi} [Q(\phi) e^{i\phi}] d\phi \right)$$

Simplifying this results gives,

$$\bar{Z} = Z_0 + i\epsilon \int_{-\pi}^{\pi} \rho(\phi) Q(\phi) e^{i\phi} d\phi \tag{B.9}$$

APPENDIX C

Two Population Relaxation Phase Shift

Simple Coupling

Here we derive a analytical approximation for the B factor in Eq. 4.29 which describes effect of the relaxation (return to equilibrium) on the collective phase response. Considering Eqs. 4.11, 4.12 we make the approximation that R_v, R_d are constant and without loss of generality we set $R_v, R_d = 1$ as any deviation from unity may be absorbed into the coupling strengths K_{vd}, K_{dv}. With this approximation the expressions simplify to give,

$$\dot{\theta} = \Delta\omega - (K_{vd} + K_{dv})\sin(\theta) \tag{C.1a}$$

$$\Omega = \bar{\omega} + (qK_{dv} - pK_{vd})\sin(\theta). \tag{C.1b}$$

Now we assume the coupling strengths are sufficiently strong for a steady state θ^* to exist with collective frequency Ω^*. We linearize $\theta(t) \approx \theta^* + \Delta\theta(t)$ to give,

$$\Delta\dot{\theta} = -(K_{vd} + K_{dv})\Delta\theta(t) \tag{C.2}$$

$$\Delta\theta(0) = -\epsilon\Delta_0(\psi). \tag{C.3}$$

The induced phase shift as the system returns to its equilibrium value is thus given by,

$$\Delta_R = \int_0^\infty \Omega(\theta(t)) - \Omega^* dt \tag{C.4}$$

$$\approx \int_0^\infty (qK_{dv} - pK_{vd})\Delta\theta(t)dt. \tag{C.5}$$

Therefore, we find that the relaxation shift may be approximated by:

$$\Delta_R \approx \epsilon\Delta_0 \frac{qK_{dv} - pK_{vd}}{K_{dv} + K_{vd}}. \tag{C.6}$$

Therefore, the B factor may be written as,

$$B = \frac{q - p\alpha}{1 + \alpha} \qquad\qquad \alpha = \frac{K_{vd}}{K_{dv}}, \tag{C.7}$$

as given in the main text (Eq. 4.30).

General Coupling

Here we show the details of the first order calculation of the relaxation phase shift for two coupled phase oscillators with a general coupling function. Specifically we consider,

$$\frac{d\phi_v}{dt} = \omega_v + K_b\Gamma(\phi_d - \phi_v) + \epsilon Q(\phi_v)\delta(t - t') \tag{C.8}$$

$$\frac{d\phi_d}{dt} = \omega_d + K_f\Gamma(\phi_v - \phi_d) \tag{C.9}$$

where Γ is a general coupling function between the two phase oscillators. Make the change of variables to $\theta = \phi_d - \phi_v$ and $\Omega = \frac{d}{dt}\frac{\phi_v+\phi_d}{2}$ yields,

$$\dot{\theta} = \Delta\omega - \Gamma_o(\theta) \tag{C.10a}$$

$$\Omega = \bar{\omega} + \Gamma_e(\theta) \tag{C.10b}$$

$$\Gamma_o(\theta) = K_f\Gamma(\theta) - K_b\Gamma(-\theta) \tag{C.10c}$$

$$\Gamma_e(\theta) = \frac{1}{2}\left[K_f\Gamma(\theta) + K_b\Gamma(-\theta)\right], \tag{C.10d}$$

with $\Delta\omega = \omega_d - \omega_v$ and $\bar{\omega} = \frac{1}{2}(\omega_d + \omega_v)$. We assume the coupling is sufficiently strong for an equilibrium phase locked state $\theta^* = \Gamma_0^{-1}(\Delta\omega)$ to exist. A perturbation according to the phase response curve $Q(\phi_v)$ at time t' gives $\Delta\theta(0) = -\epsilon Q(\phi_v)$. Linearization about the fixed point θ^* gives,

$$\Delta\theta(t) \approx \Delta\theta(0)e^{-\Gamma_o(\theta^*)t} = -\epsilon Q(\phi_v)e^{-\Gamma_o(\theta^*)t}. \tag{C.11}$$

The linear term for the frequency difference $\Delta\Omega = \Omega(t) - \Omega^*$ is given by,

$$\Delta\Omega(t) = \Gamma'_e(\theta^*)\Delta\theta(t) \tag{C.12}$$

Therefore, the phase shift as the system returns to equilibrium can be approximated by,

$$\Delta_R = \int_0^\infty \Delta\Omega(t)dt = \frac{-\epsilon Q(\phi_v)\Gamma'_e(\theta^*)}{\Gamma'_o(\theta^*)}, \tag{C.13}$$

for a general coupling function between the two populations.

APPENDIX D

Human Model Supplementary Information

Parameter Values

Optimal parameter fits for the single population (Table. D.1) and two population (Table. D.2) are given below. In addition, we show the parameters of each model which were allowed to vary in the Markov Chain Monte Carlo (MCMC) algorithm (those parameters which were fixed during the MCMC run have N/A as quantiles). Given that the variability of the data-points is largely unknown for the fitting data sets, a strict statistical interpretation should not be assumed for the quantiles provided. However, the magnitude of the quantiles does give a measure of the how well the parameter values are constrained by the fitting data. In particular, we note that the parameters β_1 and β_2 are not well-constrained by the data. The β_1 parameter plays an important role in determining the entrainment angle of the model. This can be observed by plotting the entrainment angle (as measured by the phase at lights-on for a regular light schedule) against β_1 and β_2 (Figures. D.1 and D.2). The correlation between the β parameters and the entrainment angle means the entrainment angle is also poorly constrained by the data.

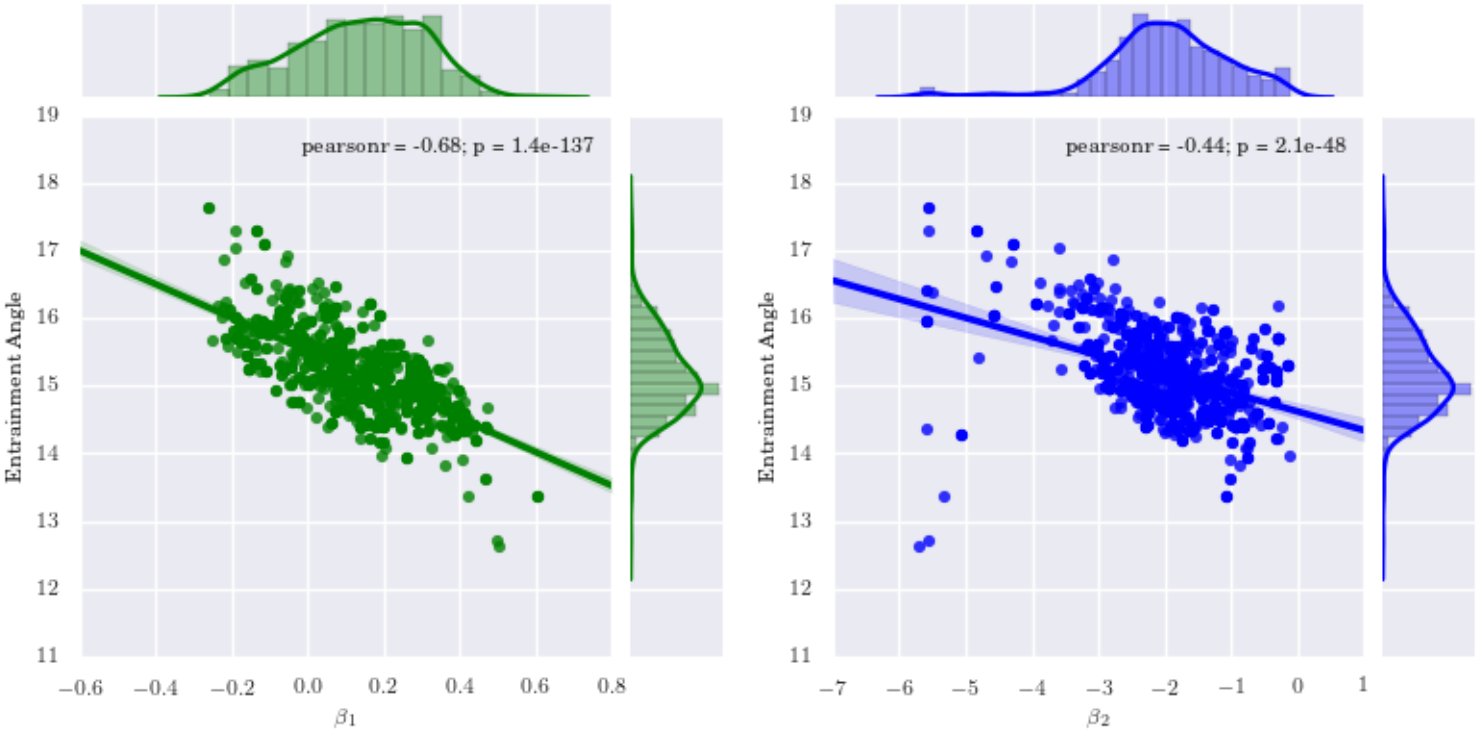

Figure D.1: For the single population human model the MCMC parameter ensemble reveals the β_1 parameters is poorly constrained by the data and correlates strongly with the entrainment angle. The β_2 parameter is seen to be better constrained by the data and shows a weaker correlation with the entrainment angle.

In applications, this variation is significant because the entrainment angle to regular light schedules may be used to define an individual's chronotype [128]. Chronotypes has been found to vary over a large range in human populations, similar to the large range observed for the MCMC ensemble [128, 151]. From the small sample sizes used in fitting the model it is unclear whether the principal source of the variation in the entrainment angle is due to differing chronotypes between study participants or if this variation may be soley attributed to noise in the data.

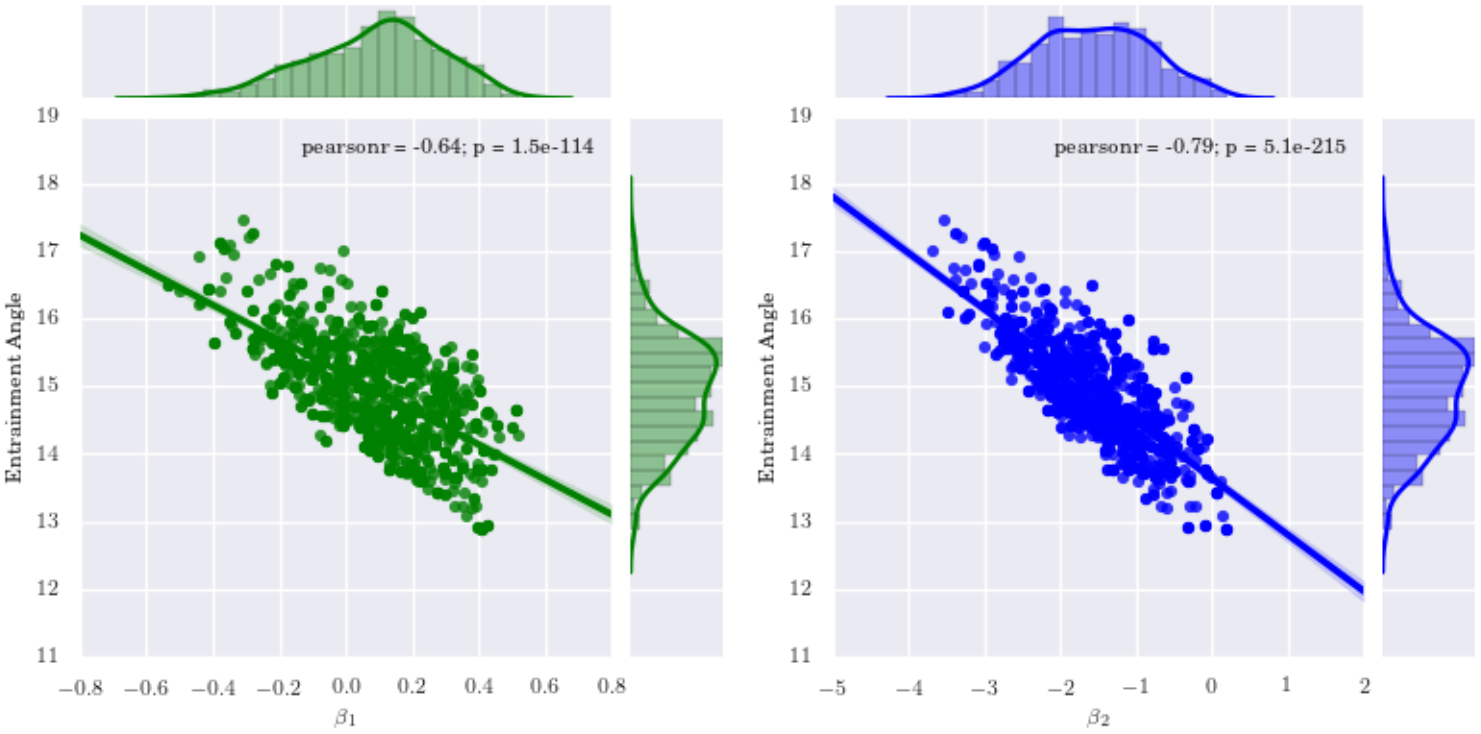

Figure D.2: For the two population human model the MCMC parameter ensemble reveals the $\beta_{1,2}$ parameters are poorly constrained by the data and each correlates with the entrainment angle.

Parameter	**Optimal Value**	**MCMC 95% Quantile**
τ	24.18	[24.09,24.33]
K	0.065	N/A
γ	0.024	N/A
σ	0.05	N/A
A_1	0.40	[0.377,0.40]
A_2	0.20	[0.18,0.22]
β_1	0.20	[-0.18,0.41]
β_2	-1.80	[-4.57,-0.31]
G	33.75	N/A
α_0	0.05	N/A
δ	0.0075	N/A
p	1.5	N/A
I_0	9325.0	N/A

Table D.1: Single Population Model Parameter Values

Parameter	**Optimal Value**	**MCMC 95% Quantile**
τ_v	24.25	N/A
τ_d	24.00	N/A
K_{vv}	0.05	N/A
K_{dd}	0.04	N/A
K_{vd}	0.05	N/A
K_{dv}	0.01	N/A
γ	0.024	N/A
σ	0.07	N/A
A_1	0.43	[0.35,0.43]
A_2	0.28	[0.26,0.40]
β_1	0.09	[-0.33,0.41]
β_2	-1.49	[-2.99,-0.11]
G	33.75	N/A
α_0	0.05	N/A
δ	0.0075	N/A
p	1.5	N/A
I_0	9985.0	N/A

Table D.2: Two Population Model Parameter Values

APPENDIX E

Phase Model Approximation of the Morris-Lecar Model

In this appendix we give the details for the Morris-Lecar neural model as used in Chapter. III to assess the applicability of the Ott-Antonsen based collective phase resetting results to biological systems. In addition, I give some additional details on how the comparison was made between the phase resetting by the full neural system and the analytical theory based on the Ott-Antonsen reduction of the Kuramoto-Sakaguchi equation.

Morris-Lecar Model

The Morris-Lecar model is a two dimensional conductance based model for neuronal firing originally derived to study Barnacle muscle fiber, but may also be used as a relatively simple model for neuronal firing [104]. The Morris-Lecar model is commonly used when studying the properties of Type I and Type II neurons, because by varying the model parameters we can see both Type I and Type II phase resetting. The Morris-Lecar dynamical system used in Chapter. III is shown in (Eq. E.1) with the parameter values shown in Table. E.1.

Parameter	Type I	Type II
C	20 uF/cm^2	20 uF/cm^2
g_{Ca}	4.0 mS/cm^2	4.4 mS/cm^2
g_K	8.0 mS/cm^2	8.0 mS/cm^2
g_L	2.0 mS/cm^2	mS/cm^2
V_{Ca}	120 mV	120 mV
V_K	-84.0 mV	-84.0 mV
V_L	-60 mV	-60 mV
$\bar{V}_1$	-1.2 mV	-1.2 mV
$\bar{V}_2$	18.0 mV	18.0 mV
$\bar{V}_3$	12.0 mV	2.0 mV
$\bar{V}_4$	17.4 mV	30.0 mV
ϕ	1/15	0.04

Table E.1: Parameter values used for the Morris-Lecar model for the Type I and Type II regimes.

$$C\frac{dV_i}{dt} = -\bar{g}_{ca}m_\infty(V_i)(V_i - V_{Ca})$$
$$- \bar{g}_K w_i(V_i - V_K) - \bar{g}_L(V_i - V_L) + \frac{g_{syn}}{N}\sum_{j=1}^{N}(V_j - V_i) + I^i_{app} \tag{E.1a}$$
$$\frac{dw_i}{dt} = \phi\frac{w_\infty(V_i) - w_i}{\tau_w(V_i)} \tag{E.1b}$$
$$m_\infty(V_i) = \frac{1}{2}\left[1 + \tanh\left(\frac{V_i - \bar{V}_1}{\bar{V}_2}\right)\right] \tag{E.1c}$$
$$w_\infty(V_i) = \frac{1}{2}\left[1 + \tanh\left(\frac{V_i - \bar{V}_3}{\bar{V}_4}\right)\right] \tag{E.1d}$$
$$\tau_w(V_i) = \frac{1}{\cosh\left(\frac{V_i - \bar{V}_3}{2\bar{V}_4}\right)} \tag{E.1e}$$

Numerical Phase Reduction

To begin the numerical phase model reduction we computed the infinitesimal phase response curve to voltage pulses for the Morris-Lecar model for both the Type I and Type II parameter regimes for a variety of applied current values (I_{app}) (Figure. E.1).

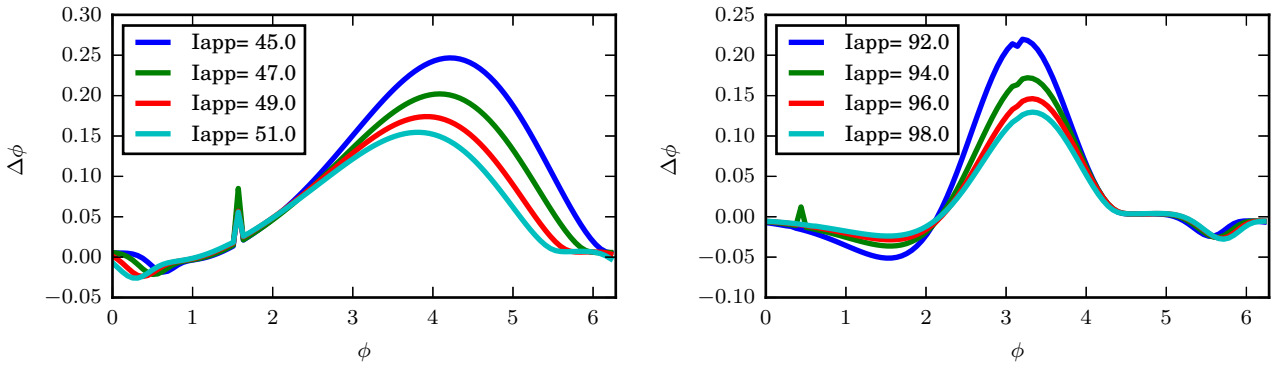

(a) Type I

(b) Type II

Figure E.1: Infinitesimal phase response curve for the Morris-Lecar type I/II system for different values of applied current. For higher values of applied current and thus higher frequency oscillations the phase response curves becomes attenuated.

In order to compute the infinitesimal phase response curves we implemented a direct solver using the fundamental matrices about the limit cycle solution [108].

The attenuation of the phase response curves at increased applied voltages has been noted in previous work [44]. This property is only of importance for this work because we must ensure that we pick I_{app} values near the respective bifurcation points in order to guarantee the individual phase response curves really are Type I and Type II shaped. We choose $I_{app} = 50.0$ for the Type I parameter regime and $I_{app} = 95.0$ for the Type II parameters.

The infinitesimal phase response curves $Q(\phi)$ can be used to find the averaged coupling functions for the Morris-Lecar system, as seen theoretically in Section 1.1.4. We estimate the coupling functions from the integral [86],

$$\Gamma(\psi) = \frac{1}{T}\int_0^T Q(\psi + t)\left[V(\psi + t) - V(t)\right] dt, \tag{E.2}$$

where T is the period of the oscillator and $[V(\psi + t) - V(t)]$ is the interaction function between the neurons. For the simple electrical coupling assumed in our model the interaction function is just the voltage difference for values taken along the limit cycle.

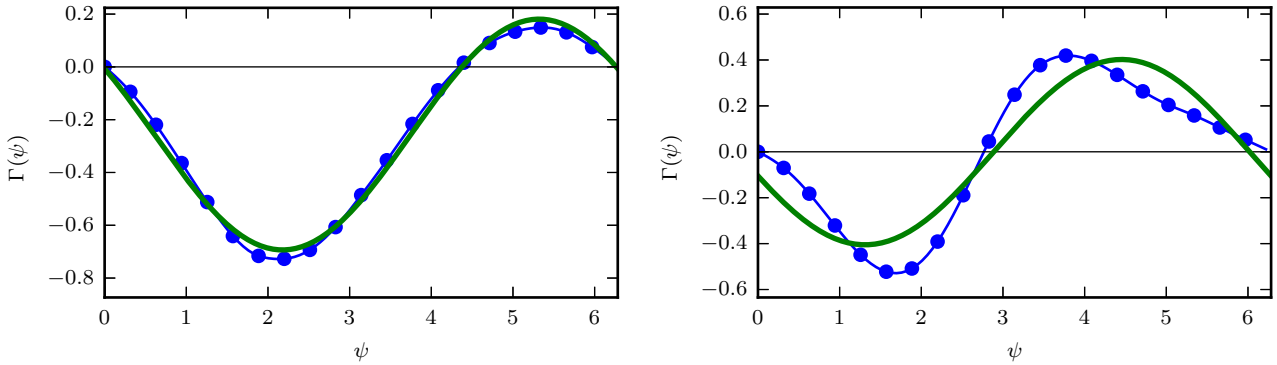

(a) Type I, $\beta = -0.65$

(b) Type II, $\beta = 0.25$

Figure E.2: Coupling function for the Morris-Lecar gap junction coupled system with Type I/II parameters. Blue dotted curves show the full numerical coupling functions, while the solid green curve shows the first harmonic approximation for the coupling functions.

Finally, in order to apply the analytical techniques utilizing the Ott-Antonsen dimension reduction technique we must truncate the Fourier terms of coupling function to include only the first order terms [95]. Figure. E.2 shows the numerical coupling functions for the Morris-Lecar system with excitatory coupling via gap junctions and the first harmonic truncation to approximate the coupling function. The first harmonic truncation of the coupling functions may then be used to build a Kuramoto-Sakaguchi model to approximate the full Morris-Lecar model (Eq. E.1).

BIBLIOGRAPHY

BIBLIOGRAPHY

[1] Carolina Abarca, Urs Albrecht, and Rainer Spanagel. "Cocaine sensitization and reward are under the influence of circadian genes and rhythm." In: *Proc. Natl. Acad. Sci. U. S. A.* 99.13 (June 2002), pp. 9026–9030.

[2] John H Abel et al. "Functional network inference of the suprachiasmatic nucleus". In: *Proc. Natl. Acad. Sci.* 113.16 (2016), pp. 4512–4517.

[3] Ute Abraham et al. "Coupling governs entrainment range of circadian clocks." In: *Mol. Syst. Biol.* 6.438 (Nov. 2010), p. 438.

[4] JA Acebrón et al. "The Kuramoto model: A simple paradigm for synchronization phenomena". In: *Rev. Mod. Phys.* 77.January (2005).

[5] Sungwon An et al. "A neuropeptide speeds circadian entrainment by reducing intercellular synchrony." In: *Proc. Natl. Acad. Sci. U. S. A.* 110.46 (Nov. 2013), E4355–61.

[6] Sungwon An et al. "Spatiotemporal distribution of vasoactive intestinal polypeptide receptor 2 in mouse suprachiasmatic nucleus". In: *J. Comp. Neurol.* 520 (2012), pp. 2730–2741.

[7] Alex Arenas et al. "Synchronization in complex networks". In: *Phys. Rep.* 469.3 (2008), pp. 93–153.

[8] Jurgen Aschoff. "Exogenous and endogenous components in circadian rhythms." In: *Cold Spring Harb. Symp. Quant. Biol.* 25 (1960), pp. 11–28.

[9] Jurgen Aschoff and Hermann Pohl. "Phase relations between a circadian rhythm and its zeitgeber within the range of entrainment". In: *Naturwissenschaften* 65.2 (1978), pp. 80–84.

[10] Sara J Aton et al. "GABA and Gi/o differentially control circadian rhythms and synchrony in clock neurons." In: *Proc. Natl. Acad. Sci. U. S. A.* 103.50 (2006), pp. 19188–19193.

[11] Abdelhalim Azzi et al. "Network Dynamics Mediate Circadian Clock Plasticity". In: *Neuron* 93.2 (2017), pp. 441–450.

[12] Barabasi and Albert. "Emergence of scaling in random networks". In: *Science* 286.5439 (Oct. 1999), pp. 509–12.

[13] Susan Benloucif, Monica I. Masana, and Margarita L. Dubocovich. "Light-induced phase shifts of circadian activity rhythms and immediate early gene expression in the suprachiasmatic nucleus are attenuated in old C3H/HeN mice". In: *Brain Res.* 747.1 (1997), pp. 34–42.

[14] Stephany M. Biello. “Circadian clock resetting in the mouse changes with age”. In: *Age (Omaha).* 31.4 (2009), pp. 293–303.

[15] Michael Breakspear, Stewart Heitmann, and Andreas Daffertshofer. “Generative models of cortical oscillations: neurobiological implications of the kuramoto model.” In: *Front. Hum. Neurosci.* 4.November (Jan. 2010), p. 190.

[16] Steven A. Brown et al. “The period length of fibroblast circadian gene expression varies widely among human individuals”. In: *PLoS Biol.* 3.10 (2005).

[17] T.M. Brown and H.D. Piggins. “Spatiotemporal Heterogeneity in the Electrical Activity of Suprachiasmatic Nuclei Neurons and their Response to Photoperiod”. In: *J. Biol. Rhythms* 24.1 (Feb. 2009), pp. 44–54.

[18] M. Renate Buijink et al. “Evidence for Weakened Intercellular Coupling in the Mammalian Circadian Clock under Long Photoperiod”. In: *PLoS One* 11.12 (2016), e0168954.

[19] Ruifeng Cao et al. “Translational control of entrainment and synchrony of the suprachiasmatic circadian clock by mTOR/4E-BP1 signaling”. In: *Neuron* 79.4 (2013), pp. 712–724. arXiv: `NIHMS150003`.

[20] Mary A. Carskadon et al. “Intrinsic circadian period of adolescent humans measured in conditions of forced desynchrony”. In: *Neurosci. Lett.* 260.2 (1999), pp. 129–132.

[21] Anne-Marie Chang et al. “Human responses to bright light of different durations”. In: *J. Physiol.* 590.13 (2012), pp. 3103–3112.

[22] Hayato Chiba and Isao Nishikawa. “Center manifold reduction for large populations of globally coupled phase oscillators”. In: *Chaos* 21.4 (Dec. 2011), p. 043103. arXiv: `arXiv:1103.0363v1`.

[23] Claudia P. Coomans, Ashna Ramkisoensing, and Johanna H. Meijer. “The suprachiasmatic nuclei as a seasonal clock”. In: *Front. Neuroendocrinol.* 37 (2015), pp. 29–42.

[24] JD Crawford. “Scaling and singularities in the entrainment of globally coupled oscillators”. In: *Phys. Rev. Lett.* 74.21 (1995), pp. 4341–4344.

[25] JD Crawford and KTR Davies. “Synchronization of globally coupled phase oscillators: singularities and scaling for general couplings”. In: *Phys. D Nonlinear Phenom.* 125 (1999), pp. 1–46.

[26] C A Czeisler et al. “Bright light induction of strong (type 0) resetting of the human circadian pacemaker.” In: *Science* 244.4910 (1989), pp. 1328–1333. arXiv: `NIHMS150003`.

[27] Charles A Czeisler et al. “Stability, precision, and near-24-hour period of the human circadian pacemaker”. In: *Science (80-.).* 284.5423 (1999), pp. 2177–2181.

[28] S. Daan and J. Aschoff. “The entrainment of circadian systems”. In: *Circadian Clocks* 12 (2001), pp. 7–43.

[29] Serge Daan. "Tonic and Phasic Effects of Light in the Entrainment of Circadian Rhythms". In: *Annu. New York Acad. Sci.* 290 (1977), pp. 51–59.

[30] H Daido. "Critical conditions of macroscopic mutual entrainment in uniformly coupled limit-cycle oscillators". In: *Prog. Theor. Phys.* 89.4 (1993), pp. 929–934.

[31] Hiroaki Daido. "Onset of cooperative entrainment in limit-cycle oscillators with uniform all-to-all interactions: bifurcation of the order function". In: *Phys. D* 91 (1996), pp. 24–66.

[32] Daniel DeWoskin et al. "Distinct roles for GABA across multiple timescales in mammalian circadian timekeeping". In: *Proc. Natl. Acad. Sci. U. S. A.* 112.29 (2015), E3911–E3919.

[33] Charna Dibner, Ueli Schibler, and Urs Albrecht. "The mammalian circadian timing system: organization and coordination of central and peripheral clocks." In: *Annu. Rev. Physiol.* 72 (2010), pp. 517–49.

[34] Jeanne F. Duffy and Charles A. Czeisler. "Age-related change in the relationship between circadian period, circadian phase, and diurnal preference in humans". In: *Neurosci. Lett.* 318.3 (2002), pp. 117–120.

[35] Jeanne F. Duffy, David W. Rimmer, and Charles A. Czeisler. "Association of intrinsic circadian period with morningness–eveningness, usual wake time, and circadian phase". In: *Behav. Neurosci.* 115.4 (2001), pp. 895–899.

[36] Michael B Elowitz and Stanislas Leibler. "A synthetic oscillatory network of transcriptional regulators." In: *Nature* 403.6767 (2000), pp. 335–338.

[37] Bard Ermentrout. "Type I Membranes, Phase Resetting Curves, and Synchrony". en. In: *Neural Comput.* 8.5 (July 1996), pp. 979–1001.

[38] J. A. Evans, J. A. Elliott, and M. R. Gorman. "Individual Differences in Circadian Waveform of Siberian Hamsters under Multiple Lighting Conditions". In: *J. Biol. Rhythms* 27.5 (2012), pp. 410–419.

[39] J.A. Evans and M.R. Gorman. "In synch but not in step: Circadian clock circuits regulating plasticity in daily rhythms". In: *Neuroscience* 320 (2016), pp. 259–280.

[40] Jennifer A. Evans et al. "Dynamic Interactions Mediated by Nonredundant Signaling Mechanisms Couple Circadian Clock Neurons". In: *Neuron* 80 (2013), pp. 973–983.

[41] Sahar Farajnia et al. "Evidence for neuronal desynchrony in the aged suprachiasmatic nucleus clock." In: *J. Neurosci.* 32.17 (2012), pp. 5891–9.

[42] Sahar Farajnia et al. "Seasonal induction of GABAergic excitation in the central mammalian clock." In: *Proc. Natl. Acad. Sci. U. S. A.* 111.26 (2014), pp. 9627–9632.

[43] G. Filatrella, A. H. Nielsen, and N. F. Pedersen. "Analysis of a power grid using a Kuramoto-like model". In: *Eur. Phys. J. B* 61.4 (2008), pp. 485–491.

[44] Christian G Fink, Victoria Booth, and Michal Zochowski. "Cellularly-driven differences in network synchronization propensity are differentially modulated by firing frequency." In: *PLoS Comput. Biol.* 7.5 (May 2011), e1002062.

[45] Nicholas C. Foley et al. "Characterization of orderly spatiotemporal patterns of clock gene activation in mammalian suprachiasmatic nucleus." In: *Eur. J. Neurosci.* 33.10 (May 2011), pp. 1851–65.

[46] Daniel B. Forger, Megan E. Jewett, and Richard E. Kronauer. "A Simpler Model of the Human Circadian Pacemaker". In: *J. Biol. Rhythms* 14.6 (Dec. 1999), pp. 533–538.

[47] Daniel B Forger and Charles S Peskin. "A detailed predictive model of the mammalian circadian clock." In: *Proc. Natl. Acad. Sci. U. S. A.* 100.25 (Dec. 2003), pp. 14806–14811.

[48] G. Mark Freeman et al. "GABA networks destabilize genetic oscillations in the circadian pacemaker". In: *Neuron* 78.5 (2013), pp. 799–806.

[49] John E Gale et al. "Disruption of circadian rhythms accelerates development of diabetes through pancreatic beta-cell loss and dysfunction." In: *J. Biol. Rhythms* 26.5 (2011), pp. 423–33.

[50] Jordi Garcia-Ojalvo, Michael B Elowitz, and Steven H Strogatz. "Modeling a synthetic multicellular clock: repressilators coupled by quorum sensing." In: *Proc. Natl. Acad. Sci.* 101.30 (2004), pp. 10955–60.

[51] Leon Glass. "Synchronization and rhythmic processes in physiology". In: *Nature* 410.March (2001), pp. 277–284.

[52] Rebecca D Gleit, Cecilia G Diniz Behn, and Victoria Booth. "Modeling interindividual differences in spontaneous internal desynchrony patterns." In: *J. Biol. Rhythms* 28.5 (Oct. 2013), pp. 339–55.

[53] Diego a Golombek and Ruth E Rosenstein. "Physiology of Circadian Entrainment". In: *Physiol. Rev* 90.3 (2010), pp. 1063–1102.

[54] Georg a. Gottwald. "Model reduction for networks of coupled oscillators". In: *Chaos* 25.5 (2015), p. 053111.

[55] CM Gray. "Synchronous oscillations in neuronal systems: mechanisms and functions". In: *J. Comput. Neurosci.* 38 (1994), pp. 11–38.

[56] Daniel J. Green and Rhanor Gillette. "Circadian rhythm of firing rate recorded from single cells in the rat suprachiasmatic brain slice". In: *Brain Res.* 245.1 (1982), pp. 198–200.

[57] Claude Gronfier et al. "Efficacy of a single sequence of intermittent bright light pulses for delaying circadian phase in humans." In: *Am. J. Physiol. Endocrinol. Metab.* 287.1 (2004), E174–E181.

[58] Gerard Groos and Jan Hendriks. "Circadian rhythms in electrical discharge of rat suprachiasmatic neurones recorded in vitro". In: *Neurosci. Lett.* 34.3 (1982), pp. 283–288.

[59] J. Guckenheimer. "Isochrons and phaseless sets". In: *J. Math. Biol.* 1.3 (Sept. 1975), pp. 259–273.

[60] John Guckenheimer and Philip J Holmes. *Nonlinear oscillations, dynamical systems, and bifurcations of vector fields*. Springer Science & Business Media, 2013.

[61] Kevin M. Hannay, Victoria Booth, and Daniel B. Forger. "Collective phase response curves for heterogeneous coupled oscillators". In: *Phys. Rev. E* 92.2 (Aug. 2015), p. 022923.

[62] Kevin M. Hannay, Daniel B. Forger, and Victoria Booth. "Macroscopic Models for Networks of Coupled Biological Oscillators". In: *arXiv Prepr. arXiv1701.04404* (Jan. 2017), pp. 1–9. arXiv: `arXiv:1701.04404v1`.

[63] D Hansel, G Mato, and C Meunier. "Phase dynamics for weakly coupled Hodgkin-Huxley neurons". In: *EPL (Europhysics Lett.* 367 (1993).

[64] Erhard Haus and Michael Smolensky. "Biological clocks and shift work: Circadian dysregulation and potential long-term effects". In: *Cancer Causes Control* 17.4 (2006), pp. 489–500.

[65] Hyunsuk Hong and Steven H. Strogatz. "Mean-field behavior in coupled oscillators with attractive and repulsive interactions". In: *Phys. Rev. E* 85 (2012), p. 056210.

[66] W J Hrushesky. "Circadian timing of cancer chemotherapy." In: *Science* 228.4695 (Apr. 1985), pp. 73–5.

[67] Premananda Indic et al. "Comparison of amplitude recovery dynamics of two limit cycle oscillator models of the human circadian pacemaker." In: *Chronobiol. Int.* 22.4 (Jan. 2005), pp. 613–29.

[68] M E Jewett and R E Kronauer. "Refinement of a limit cycle oscillator model of the effects of light on the human circadian pacemaker." In: *J. Theor. Biol.* 192.4 (1998), pp. 455–465.

[69] M E Jewett, R E Kronauer, and C a Czeisler. "Phase-amplitude resetting of the human circadian pacemaker via bright light: a further analysis." In: *J. Biol. Rhythms* 9 (1994), pp. 295–314.

[70] Megan E. Jewett, Richard E. Kronauer, and Charles A. Czeisler. "Light- induced suppression of endogenous circadian amplitude in humans". In: *Nature* 350 (1991), pp. 59–62.

[71] ME Jewett et al. "Human circadian pacemaker is sensitive to light throughout subjective day without evidence of transients". In: *Am. J. Physiol.* 273.5 Pt 2 (1997), R1800–R1809.

[72] CH Johnson. "Forty years of PRCs-What have we learned?" In: *Chronobiol. Int.* 16.6 (1999), pp. 711–743.

[73] Yoji Kawamura et al. "Collective Phase Sensitivity". In: *Phys. Rev. Lett.* 101.2 (July 2008), p. 024101.

[74] Yoji Kawamura et al. “Phase synchronization between collective rhythms of globally coupled oscillator groups: noisy identical case.” In: *Chaos* 20.4 (Dec. 2010), p. 043109.

[75] Sat Bir S. Khalsa et al. “A Phase Response Curve to Single Bright Light Pulses in Human Subjects”. In: *J. Physiol.* 549.3 (2003), pp. 945–952.

[76] Jae Kyoung Kim and Daniel B Forger. “A mechanism for robust circadian timekeeping via stoichiometric balance.” In: *Mol. Syst. Biol.* 8.1 (2012), p. 630.

[77] Tae-Wook Ko and G. Ermentrout. “Phase-response curves of coupled oscillators”. In: *Phys. Rev. E* 79.1 (Jan. 2009), p. 016211.

[78] R J Konopka and S Benzer. “Clock mutants of Drosophila melanogaster.” In: *Proc. Natl. Acad. Sci. U. S. A.* 68.9 (1971), pp. 2112–6. arXiv: `9809069v1 [arXiv:gr-qc]`.

[79] Hiroshi Kori and Alexander S. Mikhailov. “Entrainment of Randomly Coupled Oscillator Networks by a Pacemaker”. In: *Phys. Rev. Lett.* 93.25 (2004), p. 254101.

[80] Hiroshi Kori and Alexander S. Mikhailov. “Strong effects of network architecture in the entrainment of coupled oscillator systems”. In: *Phys. Rev. E* 74.6 (2006), p. 066115.

[81] Hiroshi Kori et al. “Collective-phase description of coupled oscillators with general network structure”. In: *Phys. Rev. E* 80.3 (Sept. 2009), p. 036207.

[82] Björn Kralemann et al. “Phase dynamics of coupled oscillators reconstructed from data”. In: *Phys. Rev. E* 77.6 (June 2008), p. 066205.

[83] Björn Kralemann et al. “Uncovering interaction of coupled oscillators from data”. In: *Phys. Rev. E - Stat. Nonlinear, Soft Matter Phys.* 76.5 (2007), pp. 1–4.

[84] R. E. Kronauer et al. “Mathematical model of the human circadian system with two interacting oscillators”. In: *Am. J. Physiol. - Regul. Integr. Comp. Physiol.* 242.1 (1982).

[85] Richard E Kronauer, Daniel B Forger, and Megan E Jewett. “Quantifying human circadian pacemaker response to brief, extended, and repeated light stimuli over the phototopic range.” In: *J. Biol. Rhythms* 14.6 (Dec. 1999), pp. 500–15.

[86] Yoshiki Kuramoto. *Chemical Oscillations, Waves, and Turbulence*. Vol. 19. Mineola, New York: Dover, 1984.

[87] Ji Eun Lee et al. “Quantitative peptidomics for discovery of circadian-related peptides from the rat suprachiasmatic nucleus”. In: *J. Proteome Res.* 12.2 (2013), pp. 585–593.

[88] Francis Lévi. “Chronotherapeutics: The relevance of timing in cancer therapy”. In: *Cancer Causes Control* 17.4 (2006), pp. 611–621.

[89] Zoran Levnajić and Arkady Pikovsky. "Phase resetting of collective rhythm in ensembles of oscillators". In: *Phys. Rev. E* 82.5 (Nov. 2010), p. 056202.

[90] Alfred J Lewy et al. "The circadian basis of winter depression." In: *Proc. Natl. Acad. Sci. U. S. A.* 103.19 (2006), pp. 7414–7419.

[91] C Liu and S M Reppert. "GABA synchronizes clock cells within the suprachiasmatic circadian clock." In: *Neuron* 25 (2000), pp. 123–128.

[92] Chen Liu et al. "Cellular Construction of a Circadian Clock: Period Determination in the Suprachiasmatic Nuclei". In: *Cell* 91.6 (Dec. 1997), pp. 855–860.

[93] Zhixin Lu et al. "Resynchronization of circadian oscillators and the east-west asymmetry of jet-lag". In: *Chaos* 26.9 (Sept. 2016), p. 094811.

[94] Tanushree B. Luke, Ernest Barreto, and Paul So. "Complete Classification of the Macroscopic Behavior of a Heterogeneous Network of Theta Neurons". In: *Neural Comput.* 25.12 (Dec. 2013), pp. 3207–3234. arXiv: `1309.2848v1`.

[95] SA Marvel, RE Mirollo, and SH Strogatz. "Identical phase oscillators with global sinusoidal coupling evolve by Möbius group action". In: *Chaos* 19.4 (2009), p. 043104.

[96] Elizabeth S. Maywood et al. "Synchronization and maintenance of timekeeping in suprachiasmatic circadian clock cells by neuropeptidergic signaling". In: *Curr. Biol.* 16.6 (2006), pp. 599–605.

[97] Johanna H. Meijer, Stephan Michel, and Mariska J. Vansteensel. "Processing of daily and seasonal light information in the mammalian circadian clock". In: *Gen. Comp. Endocrinol.* 152 (2007), pp. 159–164.

[98] Johanna H Meijer and William J Schwartz. "In Search of the Pathways for Light-Induced Pacemaker Resetting in the Suprachiasmatic Nucleus". In: *J. Biol. Rhythms* 18.3 (2003), pp. 235–249.

[99] E. M. Mintz et al. "GABA interacts with photic signaling in the suprachiasmatic nucleus to regulate circadian phase shifts". In: *Neuroscience* 109.4 (2002), pp. 773–778.

[100] Henry P Mirsky et al. "A model of the cell-autonomous mammalian circadian clock." In: *Proc. Natl. Acad. Sci. U. S. A.* 106.27 (July 2009), pp. 11107–11112.

[101] Ernest Montbrió and Diego Pazó. "Shear diversity prevents collective synchronization". In: *Phys. Rev. Lett.* 106.25 (2011), pp. 1–4. arXiv: `1107.0903`.

[102] Ernest Montbrió, Diego Pazó, and Alex Roxin. "Macroscopic Description for Networks of Spiking Neurons". In: *Phys. Rev. X* 5.2 (2015), p. 021028.

[103] Robert Y. Moore and Victor B. Eichler. "Loss of a circadian adrenal corticosterone rhythm following suprachiasmatic lesions in the rat". In: *Brain Res.* 42 (1972), pp. 201–206.

[104] C Morris and H Lecar. "Voltage oscillations in the barnacle giant muscle fiber." In: *Biophys. J.* 35.1 (July 1981), pp. 193–213.

[105] Jihwan Myung et al. “GABA-mediated repulsive coupling between circadian clock neurons in the SCN encodes seasonal time”. In: *Proc. Natl. Acad. Sci. U. S. A.* 112.29 (2015), E3920–E3929.

[106] Jihwan Myung et al. “Period coding of Bmal1 oscillators in the suprachiasmatic nucleus.” In: *J. Neurosci.* 32.26 (June 2012), pp. 8900–8918.

[107] Mamoru Nagano et al. “An abrupt shift in the day/night cycle causes desynchrony in the mammalian circadian center.” In: *J. Neurosci.* 23.14 (2003), pp. 6141–6151. arXiv: 68.

[108] Viktor Novičenko and Kestutis Pyragas. “Computation of phase response curves via a direct method adapted to infinitesimal perturbations”. In: *Nonlinear Dyn.* 67.1 (Mar. 2011), pp. 517–526.

[109] Mikael Nygård and Maria Palomba. “The GABAergic network in the suprachiasmatic nucleus as a key regulator of the biological clock: does it change during senescence?” In: *Chronobiol. Int.* 23.1-2 (2006), pp. 427–35.

[110] Mikael Nygård et al. “Age-related changes in electrophysiological properties of the mouse suprachiasmatic nucleus in vitro”. In: *Brain Res. Bull.* 65.2 (2005), pp. 149–154.

[111] Hidenobu Ohta, Shin Yamazaki, and Douglas G McMahon. “Constant light desynchronizes mammalian clock neurons”. In: *Nat. Neurosci.* 8.3 (2005), pp. 267–269.

[112] Oleh E. Omel’Chenko and Matthias Wolfrum. “Nonuniversal transitions to synchrony in the Sakaguchi-Kuramoto model”. In: *Phys. Rev. Lett.* 109.16 (2012), pp. 1–4.

[113] Edward Ott and Thomas M Antonsen. “Long time evolution of phase oscillator systems.” In: *Chaos* 19.2 (June 2009), p. 023117.

[114] Edward Ott and Thomas M Antonsen. “Low dimensional behavior of large systems of globally coupled oscillators.” In: *Chaos* 18.3 (Sept. 2008), p. 037113.

[115] Diego Pazó and Ernest Montbrió. “Low-Dimensional Dynamics of Populations of Pulse-Coupled Oscillators”. In: *Phys. Rev. X* 4.1 (Jan. 2014), p. 011009.

[116] Charles S Peskin. *Mathematical aspects of heart physiology*. Courant Institute of Mathematical Sciences, New York University, 1975.

[117] a J K Phillips, P Y Chen, and P a Robinson. “Probing the mechanisms of chronotype using quantitative modeling.” In: *J. Biol. Rhythms* 25.3 (2010), pp. 217–27.

[118] A. Pikovsky, M. Rosenblum, and J. Kurths. *Synchronization : A Universal Concept in Nonlinear Sciences*. Cambridge, England: Cambridge University Press, 2004.

[119] Arkady Pikovsky and Michael Rosenblum. “Dynamics of globally coupled oscillators: Progress and perspectives”. In: *Chaos* 25.9 (2015).

[120] Arkady Pikovsky and Michael Rosenblum. “Dynamics of heterogeneous oscillator ensembles in terms of collective variables”. In: *Phys. D Nonlinear Phenom.* 240.9-10 (Apr. 2011), pp. 872–881.

[121] C S Pittendrigh. “The photoperiodic phenomena: seasonal modulation of the ”day within”.” In: *J. Biol. Rhythms* 3.2 (1988), pp. 173–188.

[122] C S Pittendrigh and S Daan. “A functional analysis of circadian pacemakers in noctural rodents: I. The stability and lability of circadian frequency”. In: *J. Comp. Physiol. A* 106 (1976), pp. 223–252.

[123] Colin S Pittendrigh and Serge Daan. “A Functional Analysis of Circadian Pacemakers in Nocturnal Rodents I. The Stability and Lability of Spontaneous Frequency”. In: *J. Comp. Physiol.* 106 (1976), pp. 223–252.

[124] Colin S. Pittendrigh and Serge Daan. “A Functional Analysis of Circadian Pacemakers in Nocturnal Rodents IV. Entrainment: Pacemaker as Clock”. In: *J. Comp. Physiol.* 331.3 (Oct. 1976), pp. 291–331.

[125] Colin S. Pittendrigh, Walter T Kyner, and T. Takamura. “The Amplitude of Circadian Oscillations: Temperature Dependence, Latitudinal Clines, and the Photoperiodic Time Measurement”. In: *J. Biol. Rhythms* 6.4 (1991), pp. 299–313.

[126] Ashna Ramkisoensing et al. “Enhanced phase resetting in the synchronized suprachiasmatic nucleus network.” In: *J. Biol. Rhythms* 29.1 (2014), pp. 4–15.

[127] D W Rimmer et al. “Dynamic resetting of the human circadian pacemaker by intermittent bright light.” In: *Am. J. Physiol. Regul. Integr. Comp. Physiol.* 279.5 (2000), R1574–9.

[128] Till Roenneberg et al. “Epidemiology of the human circadian clock”. In: *Sleep Med. Rev.* 11.6 (2007), pp. 429–438.

[129] Hidetsugu Sakaguchi and Yoshiki Kuramoto. “A Soluble Active Rotater Model Showing Phase Transitions via Mutual Entertainment”. In: *Prog. Theor. Phys.* 76.3 (1986), pp. 576–581.

[130] NW Schultheiss, AA Prinz, and RJ Butera. *Phase response curves in neuroscience: theory, experiment, and analysis*. New York, NY: Springer Science+Business Media, LLC., 2011.

[131] M. T. Sellix et al. “Aging Differentially Affects the Re-entrainment Response of Central and Peripheral Circadian Oscillators”. In: *J. Neurosci.* 32.46 (2012), pp. 16193–16202.

[132] Kirill Serkh and Daniel B. Forger. “Optimal Schedules of Light Exposure for Rapidly Correcting Circadian Misalignment”. In: *PLoS Comput. Biol.* 10.4 (2014).

[133] Per Sebastian Skardal, Dane Taylor, and Jie Sun. “Optimal synchronization of directed complex networks”. In: *Phys. Rev. Lett.* 113.14 (2014), pp. 1–11.

[134] Michael Small. *Applied Nonlinear Time Series Analysis*. Ed. by Leon O. Chua. World Scientific Publishing Co., 2005.

[135] Roy M Smeal, G Bard Ermentrout, and John A White. "Phase-response curves and synchronized neural networks." In: *Philos. Trans. R. Soc. Lond. B. Biol. Sci.* 365.1551 (Aug. 2010), pp. 2407–22.

[136] Bernard Sonnenschein and Lutz Schimansky-Geier. "Approximate solution to the stochastic Kuramoto model". In: *Phys. Rev. E* 88.5 (2013), pp. 1–5.

[137] Melissa a. St Hilaire et al. "Human phase response curve to a 1 h pulse of bright white light". In: *J. Physiol.* 590.13 (2012), pp. 3035–3045.

[138] Melissa a St Hilaire et al. "Human phase response curve to a 1 h pulse of bright white light". In: *J. Physiol.* 590.13 (July 2012), pp. 3035–3045.

[139] F K Stephan and I Zucker. "Circadian rhythms in drinking behavior and locomotor activity of rats are eliminated by hypothalamic lesions." In: *Proc. Natl. Acad. Sci. U. S. A.* 69.6 (1972), pp. 1583–1586.

[140] Adam R. Stinchcombe and Daniel B. Forger. "An Efficient Method for Simulation of Noisy Coupled Multi-Dimensional Oscillators". In: *J. Comput. Phys.* 321.May (2016), pp. 932–946.

[141] Steven Strogatz. *Sync*. New York: Hyperion, 2003.

[142] Steven H. Strogatz. "From Kuramoto to Crawford: exploring the onset of synchronization in populations of coupled oscillators". In: *Phys. D Nonlinear Phenom.* 143.1-4 (Sept. 2000), pp. 1–20.

[143] Alena Sumová et al. "Seasonal Molecular Timekeeping Within the Rat Circadian Clock". In: *Physiol. Res.* 53 (2004), S167–S176.

[144] A. Sumova et al. "The rat suprachiasmatic nucleus is a clock for all seasons". In: *Proc Natl Acad Sci U S A* 92.17 (1995), pp. 7754–8.

[145] K. Tominaga, S. I T Inouye, and H. Okamura. "Organotypic slice culture of the rat suprachiasmatic nucleus: Sustenance of cellular architecture and circadian rhythm". In: *Neuroscience* 59.4 (1994), pp. 1025–1042.

[146] V S Valentinuzzi et al. "Effects of aging on the circadian rhythm of wheel-running activity in C57BL/6 mice". In: *Am. J. Physiol.* 273.6 Pt 2 (1997), R1957–64.

[147] Henk Tjebbe VanderLeest et al. "Phase shifting capacity of the circadian pacemaker determined by the SCN neuronal network organization." In: *PLoS One* 4.3 (Jan. 2009), e4976.

[148] M H Vitaterna et al. "Mutagenesis and mapping of a mouse gene, Clock, essential for circadian behavior." In: *Science (80-.).* 264.5159 (1994), pp. 719–25.

[149] Vladimir Vlasov, Maxim Komarov, and Arkady Pikovsky. "Synchronization transitions in ensembles of noisy oscillators with bi-harmonic coupling". In: *J. Phys. A Math. Theor.* 48.10 (2015), p. 105101. arXiv: `1411.3204`.

[150] Vladimir Vlasov, Elbert E N Macau, and Arkady Pikovsky. "Synchronization of oscillators in a Kuramoto-type model with generic coupling". In: *Chaos* 24.2 (2014), pp. 1–8. arXiv: `arXiv:1405.5464v1`.

[151] Olivia J. Walch, Amy Cochran, and Daniel B. Forger. "A global quantification of "normal" sleep schedules using smartphone data". In: *Sci. Adv.* 2.5 (2016), e1501705–e1501705.

[152] Shinya Watanabe and Steven H. Strogatz. "Constants of motion for superconducting Josephson arrays". In: *Phys. D Nonlinear Phenom.* 74.3-4 (July 1994), pp. 197–253.

[153] D J Watts and S H Strogatz. "Collective dynamics of'small-world' networks". In: *Nature* 393.6684 (1998), pp. 440–442.

[154] David K. Welsh et al. "Individual neurons dissociated from rat suprachiasmatic nucleus express independently phased circadian firing rhythms". In: *Neuron* 14.4 (1995), pp. 697–706.

[155] R. Wever. "Virtual synchronization towards the limits of the range of entrainment". In: *J. Theor. Biol.* 36.1 (1972), pp. 119–132.

[156] A. T. Winfree. *The Geometry of Biological Time*. New York: Springer, 2001.

[157] Arthur T Winfree. "On emerging coherence". In: *Science* 298.5602 (Dec. 2002), pp. 2336–7.

[158] AT Winfree. "Biological rhythms and the behavior of populations of coupled oscillators". In: *J. Theor. Biol.* 16 (1967), pp. 15–42.

[159] Anna Wirz-Justice, Till Roenneberg, and Martha Merrow. "Life between Clocks: Daily Temporal Patterns of Human Chronotypes". In: *J Biol Rhythm.* 18.1 (2003), pp. 80–90.

[160] Kenneth P. Wright et al. "Entrainment of the human circadian clock to the natural light-dark cycle". In: *Curr. Biol.* 23.16 (2013), pp. 1554–1558.

[161] Yr Yamada and Db Forger. "Multiscale complexity in the mammalian circadian clock." In: *Curr. Opin. Genet. Dev.* 20.6 (Dec. 2010), pp. 626–33.

[162] L. Yan et al. "Two Antiphase Oscillations Occur in Each Suprachiasmatic Nucleus of Behaviorally Split Hamsters". In: *J. Neurosci.* 25.39 (2005), pp. 9017–9026.

[163] J M Zeitzer et al. "Sensitivity of the human circadian pacemaker to nocturnal light: melatonin phase resetting and suppression". In: *J. Physiol.* 526 Pt 3 (2000), pp. 695–702.